Doctoral Dissertation

Development of TiO_2/graphene nanocomposites as visible-light active photocatalysts for water treatment

Ton Nu Thanh Nhan

Supervisor: Assoc. Prof. Toshiaki Taniike

Graduate School of Advanced Science and Technology

Japan Advanced Institute of Science and Technology

Material Science

September 2020

Development of TiO_2/graphene nanocomposites as visible-light active photocatalysts for water treatment

Ton Nu Thanh Nhan
1720422

Heterogeneous photocatalysis using titanium dioxide is a well-known advanced oxidation process for water treatment. However, the large band gap, a short lifetime of photo-excited electron-hole pairs, and the ability as an absorbent limit its applications. Hybridization of TiO_2 with graphene emerges as a promising approach to diminish these drawbacks. Many efforts have been reported on the preparation of TiO_2/graphene composites, but most of them utilized graphene oxide (GO) as a starting material. Subsequent reduction of GO into so-called reduced graphene oxide (rGO) leads to the formation of defect-rich graphene with disadvantageous electronic properties. Furthermore, the aggregation of TiO_2 is usually observed because the sensitivity of titanium alkoxide to water (GO usually contains) significantly impedes the uniform and controlled growth of TiO_2 on graphene. Hence, the aim of this thesis is to explore a novel and effective approach for the preparation of the TiO_2/graphene nanocomposites to obtain excellent visible-light photocatalysts for water treatment application.

In Chapter 2, a novel GO-free route for the fabrication of TiO_2/graphene nanocomposites was explored. This route involved the ultrasonication-assisted exfoliation of graphite in a titanium tetra-*n*-butoxide and subsequent sol-gel reaction to form TiO_2 using the graphene dispersion. Featured with various advantageous characteristics (Figure 1), the obtained the TiO_2/graphene nanocomposites exhibited an excellent performance for the visible-light photocatalytic decomposition of methylene blue in an aqueous medium.

Chapter 3 concentrated on the exploration of new solvents for liquid-phase exfoliation of graphite via ultrasonication. Various new exfoliating solvents were found through screening of different solvents and their mixtures. Most importantly, the preparation of a graphene dispersion in the presence of different metal alkoxides was demonstrated, which could be useful as a direct precursor of various oxide@graphene nanocomposites without mediating GO.

In Chapter 4, further improvement in the visible-light photocatalytic performance of the TiO_2/graphene nanocomposites was achieved by chlorine doping. The chlorine-doped TiO_2/graphene nanocomposites were synthesized based on the synthetic method established in Chapter 2. With the aid of chlorine radicals in accelerating the photodecomposition of target organic compounds and a significant reduction of the amount of graphene defects, the chlorine-doped TiO_2/graphene nanocomposites exhibited a significant improvement in the photocatalytic performance compared to that of the undoped TiO_2/graphene nanocomposite (Figure 1).

To the end, I have successfully established a novel and effective route for the synthesis of the TiO_2/graphene nanocomposites and demonstrated its usefulness in the field of water treatment based on excellent visible-light photocatalysis. The results are expected to be useful not only in the field of photocatalysis, but also in the development of various oxide/graphene functional composite materials.

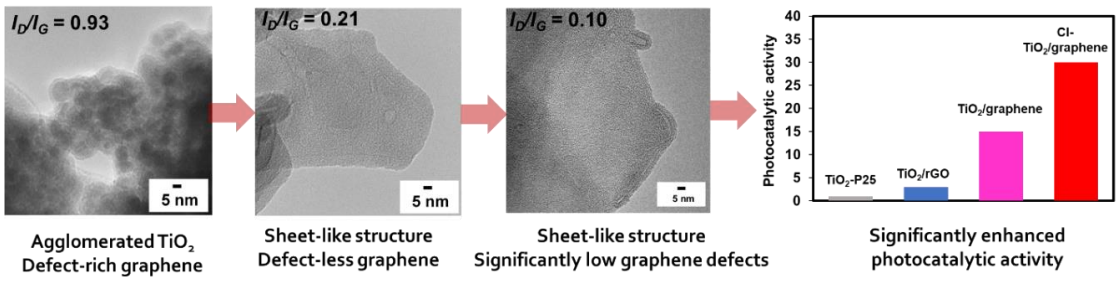

Figure 1. Development of TiO_2/graphene nanocomposites for the enhancement of visible-light photocatalytic activity.

Keywords: TiO_2/graphene, Chemical exfoliation, Sol-gel, Photocatalysis, Water treatment

Referee-in-chief:	Associate Professor	Toshiaki Taniike
	Japan Advanced Institute of Science and Technology	
Referees:	Professor	Shinya Maenosono
	Japan Advanced Institute of Science and Technology	
	Professor	Noriyoshi Matsumi
	Japan Advanced Institute of Science and Technology	
	Associate Professor	Eijiro Miyako
	Japan Advanced Institute of Science and Technology	
	Professor	Hisayuki Nakatani
	Nagasaki University	

Preface

The present thesis is submitted for the Degree of Doctor of Philosophy at Japan Advanced Institute of Science and Technology, Japan. The thesis is a unification of results of the research works that were performed on the topic “Development of TiO_2/graphene nanocomposites as visible-light active photocatalysts for water treatment” from October 2017 to September 2020 under the supervision of Assoc. Prof. Toshiaki Taniike at Graduate School of Advanced Science and Technology, Japan Advanced Institute of Science and Technology from October 2017 to September 2020..

Chapter 1 describes a general introduction of the research field and the objective of this thesis. **Chapter 2** introduces a novel synthetic route for TiO_2/graphene nanocomposites with an excellent visible-light photocatalytic activity. **Chapter 3** presents a solvent screening for the exploration of solvents for the liquid-phase exfoliation of graphite. **Chapter 4** reports the synthesis of the chlorine-doped TiO_2/graphene nanocomposites for a further improvement of the visible-light photocatalytic activity. **Chapter 5 gives a conclusion** for this thesis. All of these works are original and no part of this thesis has been plagiarized.

Ton Nu Thanh Nhan

Graduate School of Advanced Science and Technology

Japan Advanced Institute of Science and Technology

Acknowledgments

My first words are to express my acknowledgements to all of people who contributed to the works in my dissertation. The foremost place of my sincere gratitude is of Assoc. Prof. Toshiaki Taniike for his supervision, guidance, and encouragements to me from the very first day when I started to accustom science in Japan Advanced Institute of Science and Technology. His endless motivation, creativity, and enthusiasm for science have encouraged me in doing research in various ways. Once again, I would like to express my most sincere gratitude to my supervisor.

I also would like to give my special thanks to Prof. Minoru Terano, Prof. Noriyoshi Matsumi, Prof. Hideyuki Murata, Senior Lecturer Patchanee Chammingkwan, and Assist. Prof. Rajashekar Badam for their kind advice and helps to me in doing research.

I especially thank all the members in Taniike laboratory for their cooperation, suggestion and support not only for my work but also for my daily life. Special thanks would be given to Dr. Toru Wada and Dr. Ashutosh Thakur for their support and valuable discussion on my research.

I would like to specially thank my reviewers, Prof. Shinya Maenosono, Prof. Noriyoshi Matsumi, Assoc. Prof. Eijiro Miyako, and Prof. Hisayuki Nakatani to spend their time to read my thesis and give me valuable comments to improve the quality of my thesis

I would like to express my heartfelt thanks to my parents and my whole big family, who always been staying by my side, encouraging and supporting me. This is the largest motivation for me to complete my dissertation. I also deeply thank Assis. Prof. Dao Thi Ngoc Anh in Tohoku University, my senior and also my close friend, for her support and

guidance in my scientific work as well as in my daily life since I newly came to Taniike laboratory.

I also would like to give my thanks to Mr. Le Cong Duy in Murata laboratory and Mr. Le Dinh Son in Nishimura laboratory for their valuable discussions about scientific areas which I am not familiar with. My Vietnamese friends, especially Ms. Mai Thi Minh Anh and my foreign friends at JAIST have shared memorable time with me at JAIST.

Table of Contents

Abstract

Acknowledgements

CHAPTER 1: General introduction 10

1.1 Water treatment 10

1.2 TiO_2 photocatalysis 12

1.2.1. Fundamental and mechanism for TiO_2-based photocatalytic degradation of organic compounds 12

1.2.2. Design strategies of TiO_2-based photocatalysts 16

1.3 TiO_2/graphene in photocatalysis 25

1.3.1. Fundamental of TiO_2/graphene photocatalysts 25

1.3.2. Synthesis of TiO_2/graphene photocatalysts 27

1.4 Research objective 31

1.5 References 33

CHAPTER 2: Synthesis of TiO_2/graphene nanocomposites based on chemical exfoliation method. 53

Abstract 53

2.1. Introduction 54

2.2. Materials and methods 56

2.2.1. Materials 56

2.2.2. Synthesis of TiO_2/graphene nanocomposites 56

2.2.3. Characterizations 58

2.2.4. Photocatalytic test 60

2.2.5. Investigation of active species 61

2.3. Results and discussion 62

2.3.1. Synthesis of the TiO_2/graphene nanocomposites 62

2.3.2. Photocatalytic test 76
2.3.3. Identification of active species 80
2.4. Conclusion 82
2.5. References 83
CHAPTER 3: Solvents screening for efficient chemical exfoliation of graphite 96
Abstract 96
3.1. Introduction 97
3.2. Materials and methods 99
3.2.1. Materials 99
3.2.2. Chemical exfoliation of graphite 99
3.3. Results and discussion 100
3.3.1. Screening of single solvents 100
3.3.2. Screening of solvent mixtures 103
3.4. Conclusion 106
3.5. References 107
CHAPTER 4: Chlorine-doped TiO_2/graphene nanocomposites for improving visible-light photocatalytic activity 113
Abstract 113
4.1. Introduction 114
4.2. Materials and methods 116
4.2.1. Materials 116
4.2.2. Synthesis of graphene dispersion in $Ti(OnBu)_4$ 117
4.2.3. Synthesis of chlorine-doped graphene dispersion in $Ti(OnBu)_4$ 117
4.2.4. Fabrication of chlorine-doped TiO_2/graphene nanocomposites using sol-gel method 118
4.2.5. Preparation of TiO_2/rGO 119
4.2.6. Characterizations 120

4.2.7. Photocatalytic test 121
4.3. Results and discussion 123
4.3.1. Preparation of chlorine-doped TiO_2/graphene nanocomposites 123
4.3.2. Photocatalytic test 128
4.4. Conclusion 138
4.5. References 139
CHAPTER 5. General Conclusion and Future Plan 146
5.1. General conclusion 146
5.2. Future plan 148
Achievements 150

CHAPTER 1: General introduction

1.1 Water treatment

In recent years, clean water shortage is becoming a severe problem due to the expeditious growth of industry and the environmental pollution [1,2]. As a consequence of the industrial revolution, the rapid development of manufacturing technology has significantly enhanced the living standard of our human beings; however, it is also a factor threatening the environment and human health. Along with the diversification of high-tech industry, pollutants are now quantitatively and qualitatively changing, in which around 38,000 kinds of chemicals and more than 300 new materials are synthesized every year [3,4]. Thus, industrial wastewater is becoming severely and complicatedly contaminated to be managed. In addition, consideration of effective treatment methods for litter leachate and livestock manure is not sufficient. Residual organic compounds and toxic pesticides from industry are polluting rivers, groundwater and becoming more and more severe worldwide, which cannot be solved by a natural cleaning system [5–7]. Moreover, it is found that nearly 4 billion people worldwide are facing with a lack of clean and sanitized water supply, and millions of people died because of waterborne disease annually [8]. Thus, the development of advanced technologies of high efficiency as well as of low cost for water treatment is significantly important.

Several water treatment methods have been investigated or even commercialized. These methods include filtration, biodegradation [9,10], adsorption [11], coagulation/precipitation [12,13], Fenton oxidation [14,15], or biological treatment using microbial metabolism [16–18]. Though these conventional water treatment strategies are

economical and safe, each strategy has their own problems for removal of pollutants. In the coagulation and precipitation method, pollutants are precipitated as separable flocs by adding polymer coagulators or inorganic coagulants under proper pH control [19–22]. Although this method has high processing efficiency, the pipe blockages and water deterioration due to the usage of chemicals and the residual biological sludge constitute main drawbacks. In the Fenton oxidation technology, organic pollutants are decomposed by a strong oxidation power of Fenton's reagents. The process involves a coagulation process, neutralization, and oxidative reaction. However, this easy process might produce large amount of sludge and to be high cost for the operation [23–26]. Biological treatment can also be considered as an environmentally friendly method for water treatment; nevertheless, unstable processing with the production of a large amount of sludge limits the usage of this method [16–18]. Advanced oxidation processes (AOPs) have appeared as groundbreaking technologies for water treatment, which realize the elimination of organic compounds resistant to the conventional treatment methods. Based on physicochemical processes, AOPs produce powerful oxidative species such as H_2O_2, $O_2^{\bullet-}/HO_2^{\bullet}$, and $HO^{\bullet}$, which are the most oxidative agents, contributing to the redox process to destruct the target pollutants and transform them to less or non-toxic compounds [27–29]. Based on the generation mechanism of hydroxyl radicals, the AOPs can be classified into ozone-based, Fenton-based, electrochemical-based, and photocatalysis-based processes. Among these AOPs methods, heterogeneous photocatalysis has received a great interest due to its low cost with the usage of solar energy and its efficiency to decompose a wide range of ambiguous refractory organics into non-toxic compounds, or even mineralized them into carbon dioxide and water [30,31].

1.2 TiO_2 photocatalysis

1.2.1. Fundamental and mechanism for TiO_2-based photocatalytic degradation of organic compounds

Basically, photocatalytic research is related to the improvement of the solar energy utilization efficiency including solar batteries [32,33], solar thermal systems [34], and photocatalysis [35], in which solar energy is converted into chemical energy. After the finding of Fujishima and Honda about the hydrogen production by photocatalytic water splitting under solar light using a semiconductor as a catalyst [36], semiconductor photocatalysis, especially TiO_2 photocatalysis, has received a tremendous attention in both academy and industry with a wide range of applications such as hydrogen evolution [37–40], air cleaning [41–43], anti-corrosion of metals [44,45], self-purification [46–48], and antibacterial [49,50]. In particular, TiO_2 photocatalysis has been considered suitable to requirements of heterogeneous photocatalysis in water treatment, which includes i) ambient operating conditions, ii) complete mineralization of the pollutants and their intermediate compounds without production of any secondary pollution, and iii) low cost. In fact, the formation of highly reactive oxygen species on TiO_2 by the photo-induced charge separation realizes complete mineralization of organic pollutants without generating secondary pollutants [51,52].

The fundamental of the heterogeneous photocatalysis in general and for TiO_2 in particular has been reported in many literatures [36,53]. As shown in Figure 1.1, under the illumination with the photo energy (hν) of greater than or equal to the band gap of TiO_2 (3.2 eV for anatase or 3.0 eV for rutile), an electron in the valence band (VB) of TiO_2 is photo-excited to the empty conduction band (CB) of TiO_2 in the time scale of femtoseconds, and this leaves a hole in VB, thus creating a photo-excited electron-hole pair, which undergoes a series of reactions summarized as follows:

Photoexcitation: $TiO_2 + h\nu \rightarrow e^- + h^+$ (1.1)

Charge carrier trapping of e^-: $e^-_{CB} \rightarrow e^-_{TR}$ (1.2)

Charge carrier trapping of h^+: $h^+_{VB} \rightarrow h^+_{TR}$ (1.3)

Electron-hole recombination: $e^-_{TR} + h^+_{VB}(h^+_{TR}) \rightarrow e^-_{CB}$ + heat (1.4)

Photoexcited electron scavenging: $(O_2)_{ads} + e^- \rightarrow O_2^{\bullet-}$ (1.5)

Oxidation of hydroxyls: $HO^- + h^+ \rightarrow HO^\bullet$ (1.6)

Photodegradation by $HO^\bullet$: $R–H + HO^\bullet \rightarrow R^\bullet + H_2O$ (1.7)

Direct oxidation by photo-induced holes: $R^\bullet + h^+ \rightarrow R^{\bullet+} \rightarrow$ intermediate(s)/final degradation products (1.8)

Protonation of superoxide: $O_2^{\bullet-} + H^+ \rightarrow HOO^\bullet$ (1.9)

Co-scavenging of e^-: $HOO^\bullet + e^- \rightarrow HOO^-$ (1.10)

Formation of H_2O_2: $HOO^- + H^+ \rightarrow H_2O_2$ (1.11)

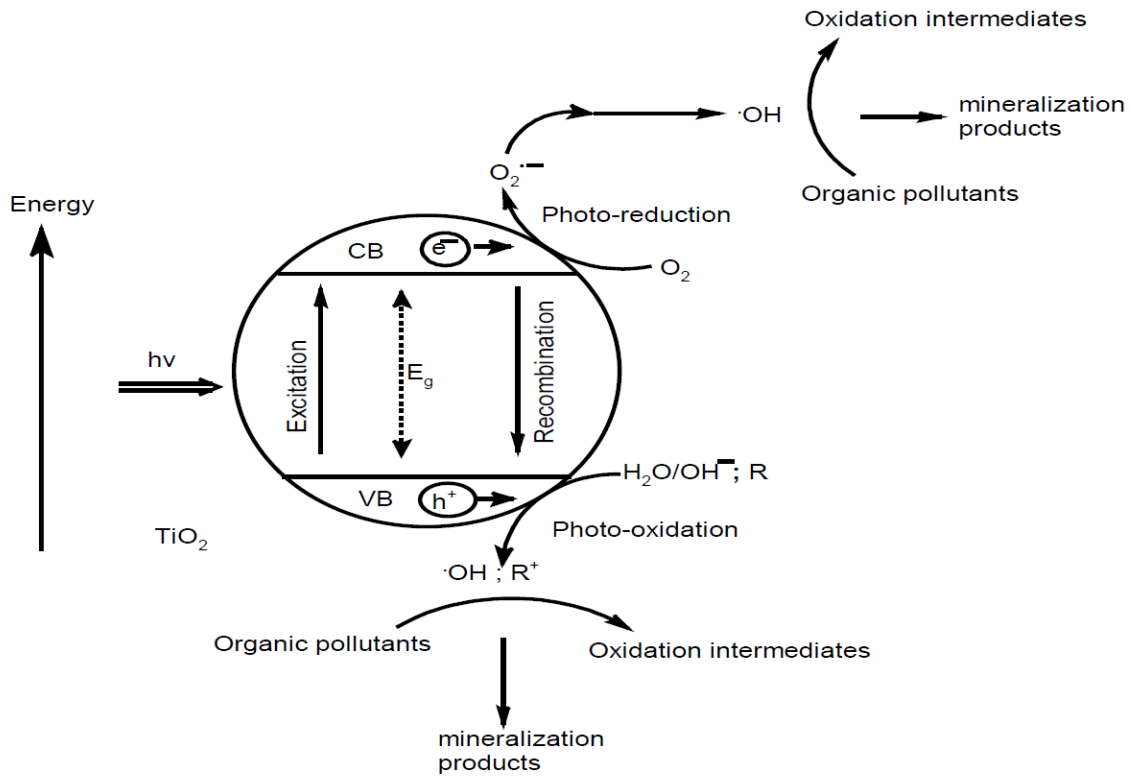

Figure 1.1. Photocatalytic process over TiO_2. Reproduced from Ref. [54].

In the absence of electron scavengers, the photo-excited electrons recombine with the holes in nanoseconds with the release of heat (Equation 1.4). Therefore, the existence of electron scavengers is critical for the successful functioning of photocatalysis. As seen in Equation 1.5, the presence of O_2, which works as an electron scavenger, prevents the electron-hole recombination through the formation of superoxide radicals. In most applications, photocatalytic decomposition reactions are conducted in the co-presence of air, water (moisture), the target compound, and the photocatalyst, in which water plays a crucial role in the reaction. This is because water molecules lead to, the production of highly reactive hydroxyl radicals for the photodegradation of organic compounds in liquid phase. Moreover, holes have a significant potential to oxidize organic species directly or indirectly by the combination with hydroxyl radicals in an aqueous solution to form intermediate(s) or

final products (Equations 1.6–1.9) [55,56]. Superoxide radicals are protonated to form hydroperoxide radicals and superoxide (Equation 1.9–1.11). The co-existence of these radicals can further prolong the lifetime of the electron-hole pairs in the photocatalytic reaction. Furthermore, these highly reactive intermediated radicals concomitantly act with holes and hydroxyl radicals to oxidize organic pollutants including bioaerosols or volatile organic compounds [57,58].

Recently, many mechanistic studies are reported on the photodegradation of different organic compounds over the TiO_2 surface. By highly reactive hydroxyl radicals, aromatic compounds can be hydroxylated, leading to successive oxidation/addition or even ring opening [59]. Then the resulting intermediates (aldehydes and/or carboxylic acids) are further oxidized to produce carbon dioxide and water if the irradiation time is adequate (Equation 1.13)

$$\text{Organic compounds} \xrightarrow{TiO_2, h\nu} \text{Intermediate(s)} \rightarrow CO_2 + H_2O \qquad (1.13)$$

In detail, the photocatalytic reaction in Equation 1.13 can be divided into 5 steps (Figure 1.2) [60,61]:

Step 1. Mass transfer of organic compound(s) (e.g. A) in the liquid phase to the TiO_2 photocatalyst surface;

Step 2. Adsorption of the organic compounds onto the photo-activated surface of TiO_2;

Step 3. Photocatalysis on the TiO_2 surface for the adsorbed organic compounds (e.g. A→B);

Step 4. Desorption of the intermediates (e.g. B) from the TiO_2 surface;

Step 5. Mass transfer of the intermediates (e.g. B) to the bulk fluid from the interface region.

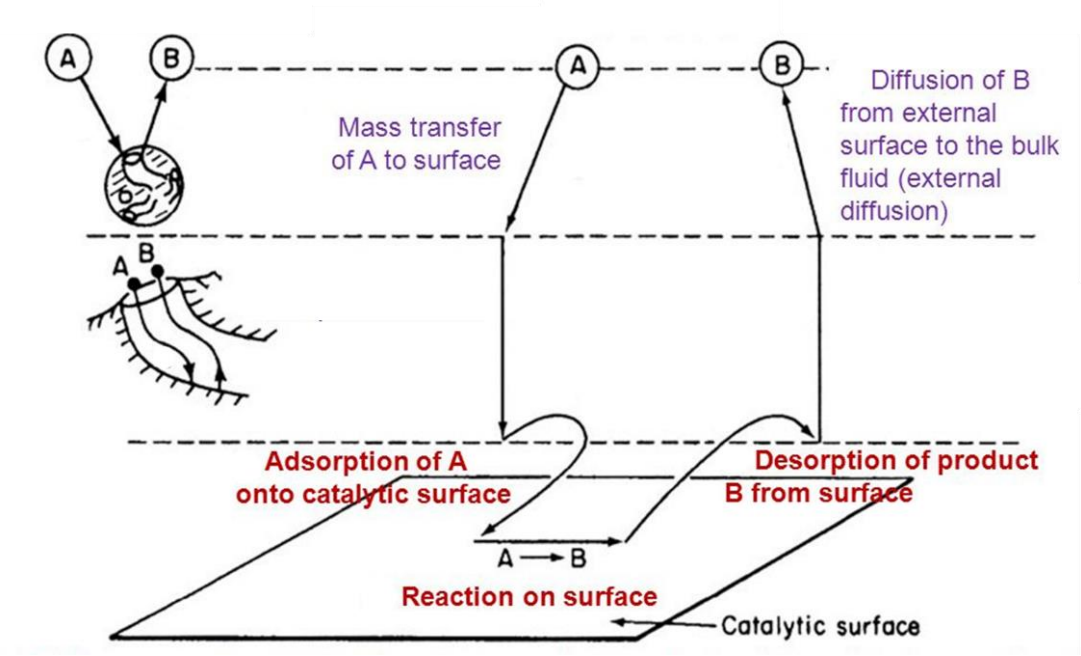

Figure 1.2. Steps involved in heterogeneous photocatalysis. Reproduced from Ref. [61].

In the consideration of rate determination step, it is clear that Steps 1 and 5 for the mass transfer are very fast compared to Steps 2, 3, and 4. According to the finding of Vinodgopal et al. in 1992 about the dependence of the photodegradation rate on the surface coverage of the photocatalyst [62], reactant adsorption and desorption (i.e. Steps 3 and 4) are believed to be impactful on the overall rate of the photocatalytic reaction.

1.2.2. Design strategies of TiO_2-based photocatalysts

So far, water treatment using TiO_2 photocatalysis has been restricted to the scale of laboratory experiments due to many technical challenges. First, the band gap of TiO_2 (3.2 eV for anatase) corresponds to the energy of ultraviolet (UV) irradiation [63–65]. In solar light, UV light accounts only 5 % of the total energy, a small fraction compared to 45 % for the visible light. Hence, improving visible-light response of TiO_2 is the primary focus of research towards its practical applications. Second, as mentioned above, the photocatalytic

reaction mainly arises on TiO_2 surfaces. Nevertheless, the adsorption of organic pollutants on the surface of TiO_2 is relatively poor (especially hydrophobic organic pollutants), which significantly reduces the photocatalytic degradation rate. Third, during the reaction, an aggregation of TiO_2 nanoparticles (NPs) may occur because of the instability of nanosized particles feature with a large surface-to-volume ratio and surface energy. This can obstruct the light absorption on the active center and decrease the photocatalytic activity of TiO_2 [66,67]. Finally, the short lifetime of electron-hole pairs (ranging from nanosecond to microsecond) of TiO_2 significantly limits its photocatalytic activity [68]. Thus, modification of TiO_2 as well as optimization of the catalyst synthesis to obtain the catalyst with a defined crystal structure, a high ability to adsorb various organic pollutants, an enhancement of electron-hole separation, and most importantly an improvement of a visible-light photocatalytic activity are the main focuses of the recent TiO_2-based photocatalysis research. A large number of efforts on TiO_2 modification have been devoted to improve its photocatalytic activity. They include doping with metal or non-metal elements, introducing heterojunctions, and surface modification with organic ligands. Past efforts presented along these three strategies are reviewed as follows.

Doping with metal and non-metal

It is known that the properties and efficiency of nanomaterials are highly influenced by the surface composition and the lattice structure. Many reports pointed out the significant improvement in the optical absorption and the charge carrier lifetime of the nanomaterials by introducing electronically active secondary species. Roy et al. reported hydrothermal preparation of Cu-doped TiO_2 and found the reduction of the band gap of the TiO_2 into 2.06 eV [69]. Sood et al. prepared Fe-doped TiO_2 using an ultrasonication-assisted hydrothermal method. The obtained material presented improved visible-light photocatalytic response due to the extension of the optical absorption edge to visible region through band gap reduction

to 2.9 eV [70]. In addition, the modification of TiO_2 by doping of metal ions like La^{3+}, Ce^{3+}, Er^{3+}, Pr^{3+}, Nd^{3+}, or Sm^{3+} exhibited an improvement in the ability to adsorb organic pollutant, resulting in the enhancement in the photocatalytic activity [71,72].

Improvement of the visible-light photocatalytic activity of TiO_2 doped with non-metals was also reported. In 2008, Yang et al. introduced N and C dopants in the TiO_2 lattice and found that the mixing of N 2p and O 2p states narrows the band gap to improve the visible-light response [73]. Bakar et al. prepared S-doped TiO_2 by a template-free peroxide route and followed by a hydrothermal treatment [74]. It was reported that the replacement of oxygen atoms by sulfur atoms in the crystal lattice of TiO_2 led to a band gap narrowing of TiO_2 [75,76]. In addition, the incorporation of sulfur atoms generated surface oxygen vacancies, which work as trapping centers for the photo-induced electrons, resulting in the reduction of the charge carrier recombination. These factors led to the improvement of its visible-light photocatalytic performance. The improvement of the visible-light photocatalytic activity was also identified in C-doped TiO_2 [77]. The incorporation of carbon atoms on the TiO_2 crystal lattice could generate oxygen vacancies. These led to the introduction of some defect levels between the VB and CB of TiO_2, resulting in the optical absorption extension to visible region [78–80].

In summary, doping with metals and non-metals can increase the visible-light photocatalytic activity of TiO_2 primarily based on the band gap narrowing or gap state introduction, and secondly due to the creation of trapping centers for photo-induced electrons. Several challenges were also reported. In the case of metal-doped TiO_2, the photocatalytic activity of these photocatalysts can be affected by the concentration of dopants [81,82]: Below an optimum dosage level, dopant ions can act as electron-hole separation centers improving the photocatalytic activity. Nevertheless, if the dosage level of dopant ions exceeds an optimum value, they can become recombination centers. Moreover,

deteriorated thermal stability and high cost due to the requirement of expensive ion-implantation facilities also limit the usage of metal-doped TiO_2 photocatalysts [83]. In the case of non-metal doping, several negative aspects were also reported including the energy intensive aspect of non-metal doping at high temperature and the usage of toxic, expensive, and unstable precursors as well as the formation of undesirable gaseous byproducts [84].

Heterojunction

In order to overcome the limitations of TiO_2 in photocatalysis, constructing heterojunctions with noble metal or other semiconductor oxides are considered to be effective to enhance the stability, optical absorption, and the electron-hole separation of TiO_2 photocatalysts. Choosing a proper substrate to couple is significantly important to increase the photocatalytic efficiency and the stability of TiO_2. The substrate with a large surface area can offer more active sites, essential for photocatalytic reaction. A proper band gap with an appropriate band edge alignment is also significant since the energy level at the interface junction dictates the transportation and separation direction of charge carriers. According to these, heterojunction can be classified into heterojunction with noble metals and heterojunction with semiconductors.

Heterojunction with noble metals

It has been found that the coupling of noble metal nanoparticles with TiO_2 could greatly enhance the visible-light photocatalytic performance of TiO_2 through surface plasmon resonance (SPR) that originates from the collective oscillation of electrons in these nanoparticles. When irradiated, hot electrons transfer into the CB of the coupled semiconductor across the Schottky barrier. It is well known that compared to semiconductors, metals have lower Fermi levels. If a semiconductor and a metal contact physically, electrons flow from the semiconductor to the metal until the Fermi level

equilibration, and this leads to the formation of a Schottky barrier, which serves as an electron trap [85]. In addition, noble metal NPs present an absorption in the visible-light region because of SPR [86,87]. There have been three mechanisms proposed to explain SPR-semiconductor photocatalysis [88]. The first one is a direct electron transfer from an excited plasmon state of the metal to the CB of the coupled semiconductor. The second mechanism is based on an increase in the optical path length of photons in the semiconductor matrix by light scattering on the metal NPs. The third one relies on the electromagnetic near-field enhancement in the vicinity of the excited plasmonic NPs.

Heterojunction with semiconductors

In the case of heterojunction between TiO_2 and another semiconductor, both of the components can generate electrons and holes by the photoexcitation. On the other hand, the direction of charge transfer relies on the relative position of VB and CB of the two components, facilitating the charge carrier separation. When TiO_2, a n-type semiconductor couples with p-type semiconductor, a p-n heterojunction can be generated. Figure 1.3 presents the formation of a space charge region at the interface by the diffusion of electrons and holes in the p-n heterojunction [89]. It is found that a strong electric field created by the difference in the electric potential can accelerate the charge carrier separation, in which the electrons are transferred from the CB of the p-type semiconductor to CB of the n-type semiconductor while holes are transferred to the VB of the p-type semiconductor. Copper oxides have received a great attention to be coupled with TiO_2 to form a p-n heterojunction for the photocatalytic reduction of CO_2 [90–93]. Xu et al. [90] prepared Cu_2O/TiO_2 with a porous and heterojunction structure by a two-step strategy. With a high surface area (4 times higher than that of TiO_2-P25), the Cu_2O/TiO_2 presented significant improvement in the adsorption ability, resulting in the improvement in the photocatalytic performance in the visible-light photoreduction of CO_2. In et al. reported hollow CuO nanotubes loaded on

titanium oxynitride, denoted as CuO-$TiO_{2-x}N_x$, which exhibited 3 times higher photocatalytic activity compared to that of TiO_2-P25 [94].

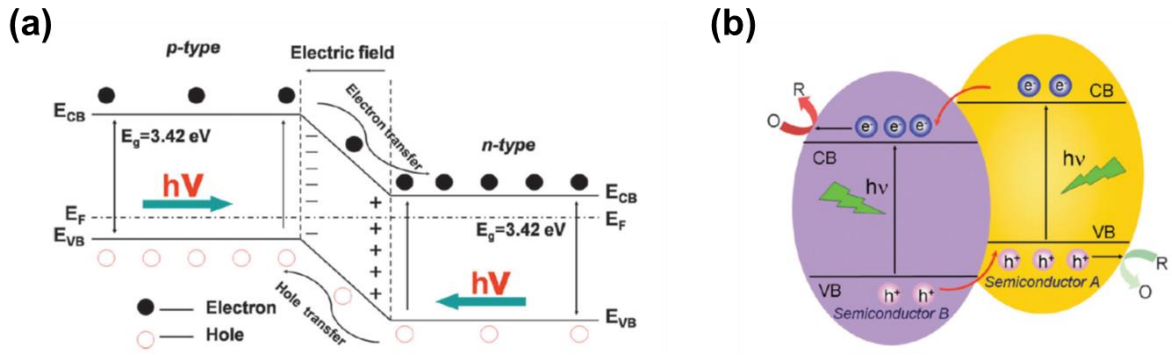

Figure 1.3. Schematic illustration of the band structure and charge carrier transfer in the a) p-n heterojunction and b) non p-n heterojunction. Adapted from Ref. [89].

In addition to the p-n heterojunction, non p-n heterojunction also exists, where a staggered band gap combination is usually employed in photocatalytic applications (Figure 1.3b). The heterostructure in this type is constructed when the two semiconductors with matching band properties tightly bond together. When the CB level of the semiconductor B is lower than that of the semiconductor A, electrons can transfer from the CB of the semiconductor A to that of B. Similarly, when the VB level of the semiconductor B is lower than the VB level of the semiconductor A, holes can transfer from the VB of the semiconductor B to that of A. These processes promote the migration and separation of photo-induced charge carrier by the internal field, preventing the recombination of electrons and holes. As a result, the photocatalytic activity of the catalyst is improved due to the effectiveness of a large number of electrons and holes in the surface of the semiconductor B and A to directly or indirectly decompose organic pollutants. Various combinations of non p-n heterojunction have been examined including CdS/TiO_2 [95–99], Bi_2S_3/TiO_2 [100–104], PbS/TiO_2 [105–108], or CeO_2/TiO_2 [109–112]. It was found that the formation of

heterojunction with TiO_2 can moderate the photocorrosion of sulfide semiconductor and also enhance the photocatalytic performance of TiO_2. Beigi et al. reported the synthesis of CdS/TiO_2 nanocomposites by the hydrothermal process and found that with an optimal ratio of CdS and TiO_2, the CdS/TiO_2 nanocomposite exhibited around 14 times higher in photocatalytic activity compared to that of TiO_2 and CdS [97]. Li et al. reported Bi_2S_3 or CdS loaded into TiO_2 by a precipitation method for the photoreduction of CO_2 to methanol [98]. Bi_2S_3/TiO_2 and CdS/TiO_2 exhibited around 2 times greater photocatalytic performance compared to that of TiO_2-P25 and TiO_2 nanotubes. Wang et al. reported the loading of PbS quantum dots on TiO_2 for the photoreduction of CO_2 and identified significant improvement of the photocatalytic performance [108]. Jiao et al. loaded CeO_2 onto 3D ordered microporous (3DOM) TiO_2 [112]. The 3DOM CeO_2/TiO_2 showed 2 times higher photocatalytic performance compared to that of TiO_2-P25. The improvement was explained due to the benefits of the heterojunction including the extension of the optical absorption to visible region based on the introduction of CeO_2 photosensitization and the improvement of electron-hole separation based on the inner electric field. Furthermore, the addition of CeO_2 was thought to be advantageous in generating surface oxygen radicals.

Surface modification with organic ligands

The visible-light photocatalytic performance of TiO_2 can also be improved by an organic modification on the surface of TiO_2, in which the modified TiO_2 shows the extension of the optical absorption into the visible region. This surface organic modification of TiO_2 includes the dye-sensitization and organic coating.

Dye-sensitization

Dye-sensitized TiO_2 photocatalysts are given by adsorption of dye molecules such as erythrosin B [113], thionine [114], substituted and unsubstituted bipyridine [115,116], or

phthalocyanine [117] on TiO_2. By sensitizing with a proper dye molecule, the light absorption could be extended to the visible-light range [115]. The dye-sensitized TiO_2 has been widely applied to the photodegradation of pollutants in an aqueous media [118,119]. As presented in Figure 1.4, the reaction process is started by HOMO-LUMO photoexcitation in dye molecules adsorbed on the surface of TiO_2 upon the visible-light irradiation, and subsequently by the electron transfer from the excited dye to the CB of TiO_2. Consequently, dyes get oxidized in the existence of proper electron donors e.g. EDTA, water, alcohol, etc., the oxidized dye is formed. The injected electrons at the TiO_2 CB react with O_2 adsorbed on the catalyst surface to form $O_2^{\bullet-}$, which further produce $HO_2^{\bullet}$, H_2O_2 and subsequently $HO^{\bullet}$, leading to the oxidation of the target organic pollutants.

In the photocatalytic mechanism, beginning with the light absorption by dye molecules and followed by the electron transfer to the TiO_2 CB, the quantity and also the stability of adsorbed dye molecules on the surface of TiO_2 are essential [120]. Insufficient stability is an intrinsic problem of the dye sensitization approach. There is no steady chemical bond formed between TiO_2 and dye molecules, and thus the desorption of dye molecules tends to occur, which necessarily reduces the photocatalytic efficiency during the photodegradation reaction. Furthermore, the competitive adsorption with coexisting pollutants at a high concentration can also strongly depress the activity of the catalyst.

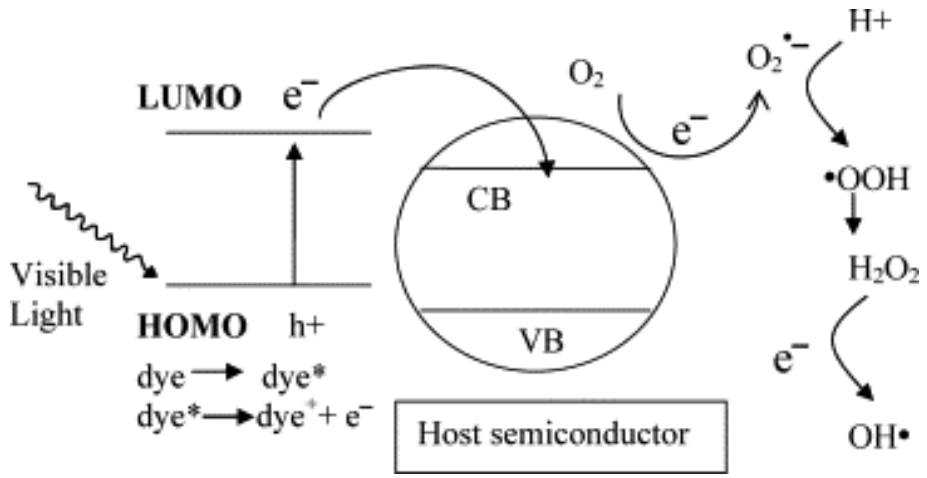

Figure 1.4. Schematic illustration of the band structure of dye-sensitized TiO_2. Adapted from Ref. [121].

Organic coating

Surface modification of TiO_2 NPs with organic chelating ligands has also received a great attention due to its ability to change the electrical and optical properties of the NPs. In 2007, Jiang et al. reported modification of the TiO_2 nanocrystal surface by a traditional reaction between the NCO groups of toluene diisocyanate (TDI) and the hydroxyl groups on the TiO_2 surface to form a steady chemical bond [122]. The presence of the surface complex leads to the extension of the absorption edge into the visible-light region, improving the photocatalytic activity compared to the unmodified TiO_2. The mechanism of the visible-light photocatalysis for TDI-modified TiO_2 is similar to that for dye-sensitized TiO_2. Upon the absorption of visible light, electrons are transferred from the organic ligand to the CB of TiO_2, then react with the adsorbed O_2 to produce $O_2^{\bullet-}$ radicals, and so on. However, the organic ligand is not cleaved differently from dye molecules. By capturing an electron from the environment, it can be recovered and then involved in another reaction cycle by the absorption of another photon [123].

1.3 TiO_2/graphene in photocatalysis

Among different materials that can be paired with TiO_2, carbon materials are regarded as promising owing to their unique advantages such as chemical inertness and high stability in both acidic and basic environments as well as tunable chemical and textual properties. Recently, carbon nanomaterials including carbon nanotubes, fullerenes, and graphene nanosheets have been widely investigated to be paired with TiO_2, opening a new generation for this material in photocatalysis [124–126]. Among carbon nanomaterials, graphene appeared as the newest material to be paired with TiO_2. Graphene is a versatile material, featured with advantageous characteristics like high electron mobility (15000 $cm^2\ V^{-1}\ s^{-1}$), extremely high specific surface area (2630 $m^2\ g^{-1}$), excellent thermal conductivity (~4000 $W\ m^{-1}\ K^{-1}$), and outstanding mechanical strength (tensile strength of 130 GPa) [127–130]. In paring with TiO_2, the zero band gap of graphene satisfies a prerequisite to be an excellent sensitizer. In addition, high electron mobility of graphene resulting from a delocalized conjugated π electrons is advantageous to the effective charge carrier separation, resulting in the enhancement of photocatalytic activity of the material [131–133]. In addition, an extremely large specific surface area of graphene as a support provides a favorable scaffold to anchor TiO_2 NPs and also improves the adsorption capacity of the TiO_2 catalyst with pollutants [134,135].

1.3.1. Fundamental of TiO_2/graphene photocatalysts

In the preparation of the TiO_2/graphene photocatalyst, most of the conventional methods have used graphene oxide (GO) as a starting material and then reduced into graphene; thus, the term reduced graphene oxide (rGO) was always appeared in the sample name. The first report in the preparation of TiO_2/graphene (denoted as TiO_2/rGO)

composites was released in 2008 by Williams et al. [136], in which UV-assisted photocatalytic reduction was employed. In brief, in the presence of ethanol and under UV irradiation, photogenerated holes in TiO_2 VB were scavenged to form ethoxy radicals, leaving electrons accumulating within TiO_2 NPs. When GO was added, the accumulated electrons interacted with GO and reduced certain surface groups to form rGO (Equations 1.14 and 1.15, and Figure 1.5).

$$TiO_2 + h\nu \rightarrow TiO_2(h^+ + e^-) \xrightarrow{C_2H_5OH} TiO_2(e^-) + H^+ + C_2H_4OH^{\bullet} \quad (1.14)$$

$$TiO_2(e^-) + GO \rightarrow TiO_2 + rGO \quad (1.15)$$

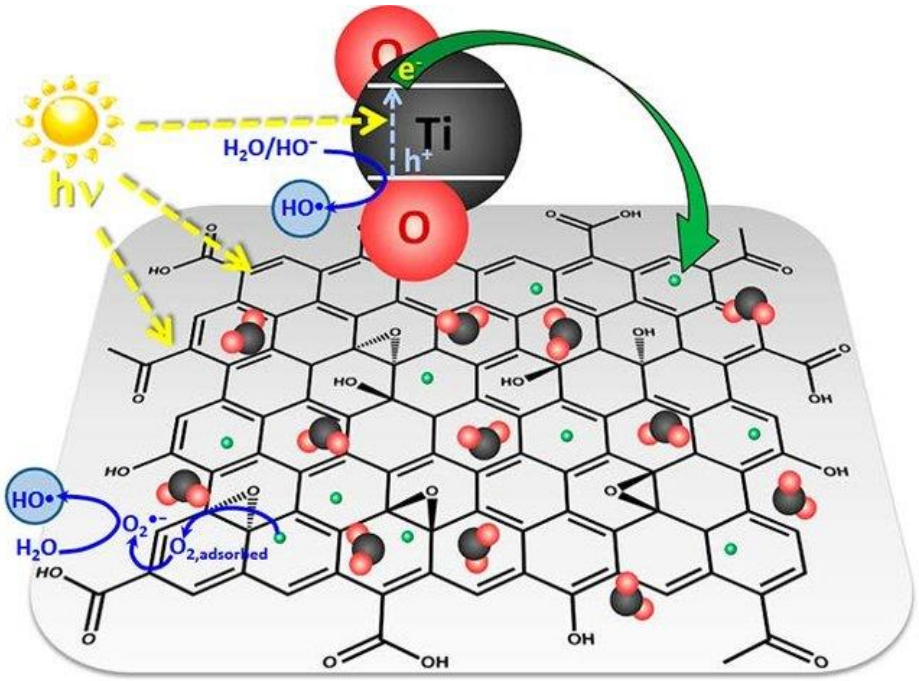

Figure 1.5. Preparation of a TiO_2/rGO composite with the reduction of GO and the formation of HO• under UV irradiation [137].

There have been several pathways to explain the photodegradation of pollutants in the presence of TiO_2/rGO composites. Liu et al. studied the degradation of methylene blue (MB) in water using rGO-wrapped TiO_2 photocatalysts and indicated that rGO acted as a

sink for photo-generated electrons [138]. By the irreversible adsorption process on the surface of the catalyst, adsorbed MB molecules would be oxidized by $O_2^{\bullet-}$ produced from the reaction between a dissolved O_2 molecule and an electron contained in rGO surface. The photogenerated holes in TiO_2 could also generate the active $HO^{\bullet}$. Chen et al. prepared TiO_2/rGO composites and observed that with the behavior of p-type semiconductor, GO also presented as a sensitizer improving the visible-light photocatalytic activity [139]. Similarly, Du et al. also confirmed the role of GO as a sensitizer by investigating the interface between the graphene and TiO_2 rutile [140]. They found that a significant charge was transferred to TiO_2 from graphene, producing a hole doping in the graphene layer. Therefore, under this hypothesis, electrons can be excited and transferred from graphene to the CB of TiO_2 under visible-light irradiation.

1.3.2. Synthesis of TiO_2/graphene photocatalysts

In recent years, many efforts have been devoted on the synthesis of TiO_2/graphene photocatalysts with varied morphologies. Various methods have been proposed, for example, mechanical mixing, hydrothermal/solvothermal, sol-gel, vacuum activation, heterogeneous coagulation, and so on. This section summarizes synthetic methods widely used in literature for the preparation of TiO_2/graphene.

Mechanical mixing method

Among the synthetic methods for TiO_2/graphene photocatalysts, mechanical mixing is the easiest one, which includes mixing and sonication steps between TiO_2 NPs and graphene or GO. The formation of chemical bonds is not expected in this case, resulting in the weak interaction of the two phases [136]. Zhang et al. synthesized P25/GO/Pt hybrid photocatalyst based on a mechanical mixing strategy [141]. The obtained photocatalyst presented improved photocatalytic performance in the hydrogen production via water

splitting even though the weak interaction between the hybrids was found. Kamegawa et al. utilized a mixing process at high temperature to crystallize TiO_2 NPs on a mesoporous silica support along with graphene coating [142]. The synthesized photocatalyst showed high performance in the photodegradation of 2-propanol. This improvement was attributed to the transfer of electron to graphene, enhancing the charge carrier separation and also to the high adsorption ability of the material.

Hydrothermal and solvothermal methods

Hydrothermal and solvothermal methods are popular methods for the production of TiO_2/rGO composites. The methods involve treatment under elevated temperature and pressure using a stainless steel autoclave to convert GO into rGO. The term "hydrothermal" indicates a strategy in which crystals are grown in an aqueous medium at high temperature and pressure. High pressure comes from the usage of water above its boiling point and the use of high temperature is beneficial to produce high-quality crystals of the material. In the hydrothermal technique, TiO_2 NPs and nanowires are utilized as TiO_2 sources [143]. In addition, other precursors such as $TiCl_4$, $(NH_4)_2TiF_6$, or titanium alkoxides are also alternatively used to prepare TiO_2/graphene nanocomposites [144]. For examples, Zhang et al. prepared TiO_2-P25/rGO composites by a hydrothermal method [145], which maintained the surface area and identical crystalline structure of TiO_2-P25. However, a poor connection between TiO_2 NPs and rGO sheets was observed in the produced composite. To deal with this limitation, Liang et al. synthesized similar composites by a two-step method consisting of the deposition of TiO_2 on GO sheets by a slow hydrolysis of titanium tetra-*n*-butoxide and then a hydrothermal treatment to convert TiO_2 into the anatase form [146]. Liu et al. also synthesized the composites through a two-phase strategy [147]. First, TiO_2 nanorods were dispersed in toluene and then stabilized with oleic acid to form the first phase. The second phase was formed by dispersing GO sheets in deionized water. The self-assembly of

these two materials took place at the water/toluene interface. The usage of ecofriendly reducing agents was also considered to reduce GO in the hydrothermal method. For examples, Shen et al. introduced glucose as a reducing agent to prepare TiO_2/rGO composites; nonetheless, the utilization of glucose led to incomplete reduction of GO under hydrothermal conditions [148].

Similar to the definition of the hydrothermal method, the term solvothermal process illustrates the growth of crystals at high temperature and pressure but in a non-aqueous solution. Nevertheless, the operated temperature can be much higher than that in the hydrothermal strategy due to the usage of high boiling points organic solvents. It has been reported that compared to hydrothermal one, the solvothermal method usually presents a better control in the shape, size distribution and crystallinity of the TiO_2 NPs, thus it is more widely used to prepare NPs with narrow size range and dispersity [149–151]. A variety of research works on the synthesis of TiO_2/graphene nanocomposite have been published based on the solvothermal method. For example, Li et al. synthesized TiO_2/graphene nanocomposites using a solvothermal method with the aid of a surfactant to prevent the agglomeration of TiO_2 NPs and increase the surface area of the nanocomposites [152]. The formed TiO_2/graphene nanocomposites presented high photocatalytic activity and stability in the visible-light photodegradation of dye molecules. This high activity was ascribed to the band gap narrowing, the improvement of textural properties, and restricted charge career recombination in the prepared nanocomposites. The next efforts on the synthesis of TiO_2/graphene nanocomposites based on a solvothermal method introduced a sort of structure-directing agents to control the shape and the morphology of the nanocomposites [153–156]. For instance, Xie et al. utilized glucose to control the morphology and shape of TiO_2/graphene [153]. They found that through the surface hydroxyl groups, a low content of glucose can bridge chemically the GO surface and TiO_2 nanoparticles, resulting in the

formation of the well-dispersed TiO_2/graphene nanocomposites. A similar result in controlling the shape and morphology of the TiO_2/graphene nanocomposites was also obtained using HF [157–160], ethylene glycol [161], or ammonia [162,163].

Sol-gel method

The sol-gel method is a technique to prepare inorganic ceramics from a solution by converting a liquid precursor to a sol, which is subsequently transformed to a gel network [164]. The precursors are firstly mixed together in a liquid phase. Then via hydrolysis and condensation processes, a stable colloidal suspension is formed, called as a sol. Subsequently, the colloidal particles in the sol aggregate to form a three-dimensional network structure of the gel. The final products are obtained after drying and/or calcination processes. The particle sizes of the nanomaterials can be tuned by controlling pH, solution composition, and reaction temperature [165]. This method has been widely used in the synthesis of TiO_2/graphene nanocomposites. The main advantage of the sol-gel method is the mild synthetic condition, in which high temperature and pressure are not required. In addition, the controllability and low cost are also the highlights of this synthetic method [166]. Wang et al utilized the sol-gel method for in-situ growth of nanocrystalline TiO_2 on graphene sheets [167]. At first, the sol was formed by mixing graphene sheets, titanium sources, sulfate surfactants, and solvents. Subsequently, the nucleation and condensation processes led to the in-situ crystallization of TiO_2 on graphene sheets with a desired phase and morphology. In another work, Liu et al. prepared TiO_2/graphene nanocomposites via the sol-gel method using titanium isopropoxide as the TiO_2 precursor and graphene (formed by a reduction of GO using hydrazine hydrate) [168]. Titanium isopropoxide was dropwise added into a graphene dispersion in ethanol in the presence of cetyltrimethylammonium bromide as a cationic surfactant. Water was then added dropwise into the mixture. The

obtained TiO_2/graphene nanocomposite exhibited an excellent visible-light photocatalytic performance in the photodegradation of methylene blue.

1.4 Research objective

Owing to the expeditious growth of industry and the environmental pollution in both quantity and quality, clean water shortage is becoming more and more serious. Thus, the development of efficient and low-cost water treatment technologies is of paramount importance. Several economical and safe methods for water treatment have been established like filtration, biodegradation, coagulation/precipitation, Fenton oxidation, etc. However, the pipe blockages due to the production of a large amount of sludge is one of the main drawbacks of these conventional methods. AOPs have emerged as innovated alternatives for water treatment. Among AOPs approaches, heterogeneous photocatalysis is one of the promising methods owing to its low cost and high efficiency to decompose a wide range of organic pollutants into non-toxic compounds and even achieving their mineralization.

TiO_2 has received an enormous interest as a photocatalyst in a wide range of applications and especially in water treatment because of its ambient operation conditions, low cost, and an ability to mineralize completely the pollutants and their intermediate compounds. However, the large band gap, a short lifetime of photo-excited electron-hole pairs, and the low adsorption ability limit the photocatalytic efficiency of TiO_2. Considerable efforts have been made to eliminate these pitfalls of TiO_2 including doping with metallic or non-metallic elements, introducing heterojunctions, or surface modification with organic ligands. Among these modifications, hybridization of TiO_2 with graphene is a promising approach.

In recent years, many efforts have been reported on the synthesis of TiO_2/graphene nanocomposites. In these efforts, nanocomposites were mostly prepared from GO, in which GO sheets were coupled with TiO_2 or some molecular precursor such as titanium alkoxides, and then reduced to rGO. Compared to the commercial TiO_2-P25, the produced nanocomposites exhibited an enhancement in the photocatalytic activity in the visible-light region. However, the reported improvements are still unsatisfactory for practical applications. This is partly because the GO reduction process can generate a large amount of defects on the graphene framework [169–171]. These defects inevitably affect the electronic properties of the photocatalyst by the decrease of the ballistic transport path length and the introduction of scattering centers. In addition, the aggregation of TiO_2 was usually observed because the sensitivity of titanium alkoxide to water (GO usually contains) significantly impedes the uniform and controlled growth of TiO_2 on graphene

Thus, the aims of this thesis are to explore a novel and effective approach for the preparation of the TiO_2/graphene nanocomposites which can solve the above-mentioned difficulties in the conventional synthetic methods, and to develop excellent visible-light photocatalysts for water treatment application. These objectives are effectuated and developed in the following three chapters of this thesis.

Chapter 2 demonstrates a novel GO-free route to synthesize the TiO_2/graphene nanocomposites. Via the chemical exfoliation of graphite in titanium tetra-*n*-butoxide, a graphene dispersion was obtained, which was used for the sol-gel reaction to produce the TiO_2/graphene nanocomposites in the presence of different catalysts. Featured with various advantages for effective visible-light photocatalysts, the obtained the TiO_2/graphene nanocomposites exhibited excellent performance for the photocatalytic decomposition of methylene blue in an aqueous medium.

Chapter 3 focuses on the solvent exploration for the liquid-phase exfoliation of graphite under ultrasonication. By screening different solvents and their mixtures, various of new exfoliating solvents were found. A synergistic effect among different effective functional groups had been identified. The synergism was found to be more effective in a form of solvent mixtures. In addition, this solvent-mixture strategy was also effective for the preparation of a graphene dispersion with metal alkoxides, precursors for the synthesis of oxide@graphene nanocomposite.

Chapter 4 presents further improvement in the visible-light photocatalytic performance of the TiO_2/graphene nanocomposites by doping chlorine. Chlorine-doped TiO_2/graphene nanocomposites were synthesized based on the synthetic method discovered in Chapter 2. With the aid of chlorine radicals in accelerating the photodecomposition of organic compounds, dramatic improvement in the visible-light photocatalytic activity was achieved.

This thesis is expected to be useful for the synthesis of excellent visible-light TiO_2/graphene photocatalysts in particular and for the synthesis of a variety of oxide@graphene nanocomposites with desirable properties for a wide range of applications in general.

1.5 References

[1] Tollefson, J. How green is my future? UN panel foresees big growth in renewable energy, but policies will dictate just how big. Nature 2011; 473(7346):134–6.

[2] Rodell, M., Velicogna, I., Famiglietti, J. S. Satellite-based estimates of groundwater depletion in India. Nature 2009; 460(7258):999–1002.

[3] Richardson, S. D. Environmental mass spectrometry: Emerging contaminants and current issues. Anal. Chem. 2012; 84(2):747–78.

[4] Carlsen, L., Bruggemann, R., Sailaukhanuly, Y. Application of selected partial order tools to analyze fate and toxicity indicators of environmentally hazardous chemicals. Ecol. Indic. 2013; 29:191–202.

[5] Heikkinen, M., Poutiainen, H., Liukkonen, M., Heikkinen, T., Hiltunen, Y. Subtraction analysis based on self-organizing maps for an industrial wastewater treatment process. Math. Comput. Simulat. 2011; 82(3):450–9.

[6] Biati, A., Moattar, F., Karbassi, A. R., Hassani, A. H. Role of saline water in removal of heavy elements from industrial wastewaters. Int. J. Environ. Res. 2010; 4(1):177–82.

[7] Tajeddine, L., Nemmaoui, M., Mountacer, H., Dahchour, A., Sarakha, M. Photodegradation of fenamiphos on the surface of clays and soils. Environ. Chem. Lett. 2010; 8(2):123–8.

[8] Malato, S., Fernández-Ibáñez, P., Maldonado, M. I., Blanco, J., Gernjak, W. Decontamination and disinfection of water by solar photocatalysis: Recent overview and trends. Catal. Today 2009; 147(1):1–59.

[9] Dhall, P., Kumar, R., Kumar, A. Biodegradation of sewage wastewater using autochthonous bacteria. Sci. World J. 2012; 2012:861903.

[10] Massot, A., Estève, K., Noilet, P., Méoule, C., Poupot, C., Mietton-Peuchot, M. Biodegradation of phytosanitary products in biological wastewater treatment. Water Res. 2012; 46(6):1785–92.

[11] Burakov, A. E., Galunin, E. V., Burakova, I. V., Kucherova, A. E., Agarwal, S., Tkachev, A. G., *et al.* Adsorption of heavy metals on conventional and nanostructured materials for wastewater treatment purposes: A review. Ecotoxicol. Environ. Saf. 2018; 148:702–712.

[12] Sun, Y., Zhou, S., Chiang, P. C., Shah, K. J. Evaluation and optimization of enhanced coagulation process: Water and energy Nexus. Water-Energy Nexus 2020; 2(1):25–36.

[13] Keeley, J., Jarvis, P., Judd, S. J. Coagulant recovery from water treatment residuals: A review of applicable technologies. Crit. Rev. Environ. Sci. Technol. 2014; 44(24):2675–719.

[14] Zhang, M. H., Dong, H., Zhao, L., Wang, D. X., Meng, D. A review on Fenton process for organic wastewater treatment based on optimization perspective. Sci. Total Environ. 2019; 670:110–21.

[15] Chen, Y., Cheng, Y., Guan, X., Liu, Y., Nie, J., Li, C. A rapid Fenton treatment of bio-treated dyeing and finishing wastewater at second-scale intervals: Kinetics by stopped-flow technique and application in a full-scale plant. Sci. Rep. 2019; 9(1):1–11.

[16] Liberatore, L., Bressan, M., Belli, C., Lustrato, G., Ranalli, G. Chemical and biological combined treatments for the removal of pesticides from wastewaters. Water Air Soil Pollut. 2012; 223(8):4751–9.

[17] López, J. C., Reina, A. C., Gómez, E. O., Martín, M. B., Rodríguez, S. M., Pérez, J. S. Integration of solar photocatalysis and membrane bioreactor for pesticides degradation. Sep. Sci. Technol. 2010; 45(11):1571–8.

[18] Bressan, M., Liberatore, L., d'Alessandro, N., Tonucci, L., Belli, C., Ranalli, G. Improved combined chemical and biological treatments of olive oil mill wastewaters. J. Agric. Food Chem. 2004; 52(5):1228–33.

[19] Tahir, M. S., Saleem, M., Malik, S. R., Khan, J. R., Siebenhofer, M. An innovative and advanced oxidation process for effluent treatment through wet tube-type electrostatic precipitation. Chem. Eng. Process. 2012; 52:16–20.

[20] de Mello Ferreira, A., Marchesiello, M., Thivel, P. X. Removal of copper, zinc and nickel present in natural water containing Ca^{2+} and HCO^{3-} ions by electrocoagulation. Sep. Purif. Technol. 2013; 107:109–17.

[21] Mansour, L. B., Kesentini, I. Treatment of effluents from cardboard industry by coagulation-electroflotation. J. Hazard. Mater. 2008; 153(3):1067–70.

[22] Hanay, Ö., Hasar, H. Effect of anions on removing Cu^{2+}, Mn^{2+} and Zn^{2+} in electrocoagulation process using aluminum electrodes. J. Hazard. Mater. 2011;189(1–2):572–6.

[23] Ghosh, P., Samanta, A. N., Ray, S. Reduction of COD and removal of Zn^{2+} from rayon industry wastewater by combined electro-Fenton treatment and chemical precipitation. Desalination 2011; 266(1–3):213–7.

[24] Lin, S. H., Chang, C. C. Treatment of landfill leachate by combined electro-Fenton oxidation and sequencing batch reactor method. Water Res. 2000; 34(17):4243–9.

[25] Ayodele, O. B., Hameed, B. H. Synthesis of copper pillared bentonite ferrioxalate catalyst for degradation of 4-nitrophenol in visible-light assisted Fenton process. J. Ind. Eng. Chem. 2013; 19(3):966–74.

[26] Monteagudo, J. M., Durán, A., San Martin, I., Aguirre, M. Catalytic degradation of Orange II in a ferrioxalate-assisted photo-Fenton process using a combined UV-A/C-solar pilot-plant system. Appl. Catal. B: Environ. 2010; 95(1–2):120–9.

[27] Martins, R. C., Quinta-Ferreira, R. M. Remediation of phenolic wastewaters by advanced oxidation processes (AOPs) at ambient conditions: Comparative studies. Chem. Eng. Sci. 2011; 66(14):3243–50.

[28] Lei, W., Portehault, D., Liu, D., Qin, S., Chen, Y. Porous boron nitride nanosheets for effective water cleaning. Nat. Commun. 2013; 4(1):1–7.

[29] Deng, Y., Zhao, R. Advanced oxidation processes (AOPs) in wastewater treatment. Curr. Pollut. Rep. 2015; 1(3):167–76.

[30] Devi, L. G., Kavitha, R. A review on non-metal ion doped titania for the photocatalytic degradation of organic pollutants under UV/solar light: Role of photogenerated charge carrier dynamics in enhancing the activity. Appl. Catal. B: Environ. 2013; 140:559–87.

[31] Amr, S. S. A., Aziz, H. A., Adlan, M. N., Aziz, S. Q. Effect of ozone and ozone/Fenton in the advanced oxidation process on biodegradable characteristics of semi-aerobic stabilized leachate. CLEAN-Soil, Air, Water 2013; 41(2):148–52.

[32] Nottrott, A., Kleissl, J., Washom, B. Energy dispatch schedule optimization and cost benefit analysis for grid-connected, photovoltaic-battery storage systems. Renew. Energy 2013; 55:230–40.

[33] Lewis, N. S. Toward cost-effective solar energy use. Science 2007; 315(5813):798–801.

[34] Bouadila, S., Kooli, S., Lazaar, M., Skouri, S., Farhat, A. Performance of a new solar air heater with packed-bed latent storage energy for nocturnal use. Appl. Energy 2013; 110:267–75.

[35] Shavisi, Y., Sharifnia, S., Zendehzaban, M., Mirghavami, M. L., Kakehazar, S. Application of solar light for degradation of ammonia in petrochemical wastewater by a floating TiO_2/LECA photocatalyst. J. Ind. Eng. Chem. 2014; 20(5):2806–13.

[36] Fujishima, A., Honda, K. Electrochemical photolysis of water at a semiconductor electrode. Nature 1972; 238(5358):37–8.

[37] Kim, S., Kang, M. Hydrogen production from methanol steam reforming over Cu-Ti-P oxide catalysts. J. Ind. Eng. Chem. 2012; 18(3):969–78.

[38] Moriya, Y., Takata, T., Domen, K. Recent progress in the development of (oxy) nitride photocatalysts for water splitting under visible-light irradiation. Coord. Chem. Rev. 2013; 257(13–14):1957–69.

[39] Clatworthy, E. B., Yick, S., Murdock, A. T., Allison, M. C., Bendavid, A., Masters, A. F., Maschmeyer, T. Enhanced Photocatalytic Hydrogen Evolution with TiO_2-TiN Nanoparticle Composites. J. Phys. Chem. C 2019; 123(6):3740–9.

[40] Li, Y., Peng, Y. K., Hu, L., Zheng, J., Prabhakaran, D., Wu, S., *et al.* Photocatalytic water splitting by N-TiO_2 on MgO (111) with exceptional quantum efficiencies at elevated temperatures. Nat. Commun. 2019; 10(1):1–9.

[41] Binas, V., Venieri, D., Kotzias, D., Kiriakidis, G. Modified TiO_2 based photocatalysts for improved air and health quality. J. Materiomics 2017; 3(1):3–16.

[42] Paz, Y. Application of TiO_2 photocatalysis for air treatment: Patents' overview. Appl. Catal. B: Environ. 2010; 99(3–4):448–60.

[43] Mo, J., Zhang, Y., Xu, Q., Lamson, J. J., Zhao, R. Photocatalytic purification of volatile organic compounds in indoor air: a literature review. Atmos. Environ. 2009; 43(14):2229–46.

[44] Lee, C. K. Comparative corrosion resistance of electroless Ni-P/nano-TiO_2 and Ni-P/nano-CNT composite coatings on 5083 aluminum alloy. Int. J. Electrochem. Sci. 2012; 7:12941–54.

[45] Li, S., Fu, J. Improvement in corrosion protection properties of TiO_2 coatings by chromium doping. Corros. Sci. 2013; 68:101–10.

[46] Zhang, L., Kanki, T., Sano, N., Toyoda, A. Development of TiO_2 photocatalyst reaction for water purification. Sep. Purif. Technol. 2003; 31(1):105–10.

[47] Banerjee, S., Dionysiou, D. D., Pillai, S. C. Self-cleaning applications of TiO_2 by photoinduced hydrophilicity and photocatalysis. Appl. Catal. B: Environ. 2015; 176:396–428.

[48] Benedix, R., Dehn, F., Quaas, J., Orgass, M. Application of titanium dioxide photocatalysis to create self-cleaning building materials. Lacer 2000; 5:157–68.

[49] Verdier, T., Coutand, M., Bertron, A., Roques, C. Antibacterial activity of TiO_2 photocatalyst alone or in coatings on E. coli: The influence of methodological aspects. Coatings 2014; 4(3):670–86.

[50] Nagay, B. E., Dini, C., Cordeiro, J. M., Ricomini-Filho, A. P., De Avila, E. D., Rangel, E. C., *et al.* Visible-light-induced photocatalytic and antibacterial activity of TiO_2 codoped with nitrogen and bismuth: New perspectives to control implant-biofilm-related diseases. ACS Appl. Mater. Inter. 2019; 11(20):18186–202.

[51] Yu, J. G., Yu, H. G., Cheng, B., Zhao, X. J., Yu, J. C., *et al.* The effect of calcination temperature on the surface microstructure and photocatalytic activity of TiO_2 thin films prepared by liquid phase deposition. J. Phys. Chem. B 2003; 107(50):13871–9.

[52] Zhang, L., Jimmy, C. Y. A sonochemical approach to hierarchical porous titania spheres with enhanced photocatalytic activity. Chem. Commun. 2003; 16:2078–9.

[53] Gaya, U. I., Abdullah, A. H. Heterogeneous photocatalytic degradation of organic contaminants over titanium dioxide: A review of fundamentals, progress and problems. J. Photochem. Photobiol. C: Photochem. Rev. 2008; 9(1):1–12.

[54] Kaur, P., Sud, D. Photocatalytic degradation of quinalphos in aqueous TiO_2 suspension: Reaction pathway and identification of intermediates by GC/MS. J. Mol. Catal. A: Chem. 2012; 365:32–8.

[55] Zhao, J., Yang, X. Photocatalytic oxidation for indoor air purification: A literature review. Build. Environ. 2003; 38(5):645–54.

[56] Fujishima, A., Rao, T. N., Tryk, D. A. Titanium dioxide photocatalysis. J. Photochem. Photobiol. C: Photochem. Rev. 2000; 1:1–21.

[57] Jacoby, W. A., Blake, D. M., Penned, J. A., Boulter, J. E., Vargo, L. M., George, M. C., *et al.* Heterogeneous photocatalysis for control of volatile organic compounds in indoor air. J. Air Waste Manag. Assoc. 1996; 46(9):891–8.

[58] Sleiman, M., Conchon, P., Ferronato, C., Chovelon, J. M. Iodosulfuron degradation by TiO_2 photocatalysis: Kinetic and reactional pathway investigations. Appl. Catal. B: Environ. 2007; 71(3–4):279–90.

[59] Hoffmann, E. H., Tilgner, A., Wolke, R., Böge, O., Walter, A., Herrmann, H. Oxidation of substituted aromatic hydrocarbons in the tropospheric aqueous phase: Kinetic mechanism development and modelling. Phys. Chem. Chem. Phys. 2018; 20(16):10960–77.

[60] Herrmann, J. M. Heterogeneous photocatalysis: Fundamentals and applications to the removal of various types of aqueous pollutants. Catal. Today 1999; 53(1):115–29.

[61] Fogler, H. S. Elements of Chemical Reaction Engineering: Chapter 10: Catalysis and catalytic reactors. Prentice-Hall PTR Inc. 1999; 581–685.

[62] Vinodgopal, K., Kamat, P. V. Photochemistry on surfaces: Photodegradation of 1,3-diphenylisobenzofuran over metal oxide particles. J. Phys. Chem. 1992; 96(12):5053–9.

[63] Yin, S., Zhang, Q., Saito, F., Sato, T. Preparation of visible-light-activated titania photocatalyst by mechanochemical method. Chem. Lett. 2003; 32(4):358–9.

[64] Zaleska, A. Doped-TiO_2: A review. Recent patents on engineering 2008; 2(3):157–64.

[65] Chong, M. N., Jin, B., Chow, C. W., Saint, C. Recent developments in photocatalytic water treatment technology: A review. Water Res. 2010; 44(10):2997–3027.

[66] Gao, B., Yap, P. S., Lim, T. M., Lim, T. T. Adsorption-photocatalytic degradation of Acid Red 88 by supported TiO_2: Effect of activated carbon support and aqueous anions. Chem. Eng. 2011; 171(3):1098–107.

[67] Mallakpour, S., Nikkhoo, E. Surface modification of nano-TiO_2 with trimellitylimido-amino acid-based diacids for preventing aggregation of nanoparticles. Adv. Powder Technol. 2014; 25(1):348–53.

[68] Kusiak-Nejman, E., Morawski, A. W. TiO_2/graphene-based nanocomposites for water treatment: A brief overview of charge carrier transfer, antimicrobial and photocatalytic performance. Appl. Catal. B: Environ. 2019; 253:179–86.

[69] Roy, N., Sohn, Y., Leung, K. T., Pradhan, D. Engineered electronic states of transition metal doped TiO_2 nanocrystals for low overpotential oxygen evolution reaction. J. Phys. Chem. C 2014; 118(51):29499–506.

[70] Sood, S., Umar, A., Mehta, S. K., Kansal, S. K. Highly effective Fe-doped TiO_2 nanoparticles photocatalysts for visible-light driven photocatalytic degradation of toxic organic compounds. J. Colloid. Interface Sci. 2015; 450:213–23.

[71] Xu, A. W., Gao, Y., Xu, H. Q. Preparation, characterization, and their photocatalytic activities of rare earth doped TiO_2 nanoparticles. J. Catal. 2002; 207:151–7.

[72] Li, F. B., Li, X. Z., Hou, M. F. Photocatalytic degradation of 2-mercaptobenzothiazole in aqueous La^{3+}-TiO_2 suspension for odor control. Appl. Catal. B: Environ. 2004; 48:185–94.

[73] Yang, X., Cao, C., Erickson, L., Hohn, K., Maghirang, R., Klabunde, K. Synthesis of visible-light-active TiO_2-based photocatalysts by carbon and nitrogen doping. J. Catal. 2008; 260(1):128–33.

[74] Bakar, S. A., Ribeiro, C. Rapid and morphology controlled synthesis of anionic S-doped TiO_2 photocatalysts for the visible-light-driven photodegradation of organic pollutants. RSC Adv. 2016; 6(43):36516–27.

[75] Umebayashi, T., Yamaki, T., Itoh, H., Asai, K. Band gap narrowing of titanium dioxide by sulfur doping. Appl. Phys. Lett. 2002; 81(3):454–6.

[76] Umebayashi, T., Yamaki, T., Yamamoto, S., Miyashita, A., Tanaka, S., Sumita, T., *et al.* Sulfur-doping of rutile-titanium dioxide by ion implantation: Photocurrent spectroscopy and first-principles band calculation studies. J. Appl. Phys. 2003; 93(9):5156–60.

[77] Lu, J., Wang, Y., Huang, J., Fei, J., Cao, L., Li, C. In situ synthesis of mesoporous C-doped TiO_2 single crystal with oxygen vacancy and its enhanced sunlight photocatalytic properties. Dyes Pigm. 2017; 144:203–11.

[78] Zhang, J., Zhao, Z., Wang, X., Yu, T., Guan, J., Yu, Z., *et al*. Increasing the oxygen vacancy density on the TiO_2 surface by La-doping for dye-sensitized solar cells. J. Phys. Chem. C 2010; 114(43):18396–400.

[79] Rumaiz, A. K., Woicik, J. C., Cockayne, E., Lin, H. Y., Jaffari, G. H., Shah, S. I. Oxygen vacancies in N doped anatase TiO_2: Experiment and first-principles calculations. Appl. Phys. Lett. 2009; 95(26):262111.

[80] Pan, X., Yang, M. Q., Fu, X., Zhang, N., Xu, Y. J. Defective TiO_2 with oxygen vacancies: Synthesis, properties and photocatalytic applications. Nanoscale 2013; 5(9):3601–4.

[81] Ambrus, Z., Balasz, N., Alapi, T., Wittmann, G., Sipos, P., Dombi, A., *et al.* Synthesis, structure and photocatalytic properties of Fe(III)-doped TiO_2 prepared from $TiCl_3$. Appl. Catal. B: Environ. 2008; 81:27–37.

[82] Tong, T., Zhang, J., Tian, B., Chen, F., He, D. Preparation of Fe^{3+}-doped TiO_2 catalysts by controlled hydrolysis of titanium alkoxide and study on their photocatalytic activity for methyl orange degradation. J. Hazard. Mater. 2008; 155:572–9.

[83] Zhang, J., Wu, Y., Xing, M., Leghari, S.A.K., Sajjad, S. Development of modified N doped TiO_2 photocatalyst with metals, nonmetals and metal oxides. Energy Environ. Sci. 2010; 3:715–26.

[84] Dong, F., Guo, S., Wang, H. Q., Li, X. F., Wu, Z. B. Enhancement of the visible-light photocatalytic activity of C-doped TiO_2 nanomaterials prepared by a green synthetic approach. J. Phys. Chem. C 2011; 115:13285–92.

[85] Ziylan-Yavas, A., Mizukoshi, Y., Maeda, Y., Ince, N. H. Supporting of pristine TiO_2 with noble metals to enhance the oxidation and mineralization of paracetamol by sonolysis and sonophotolysis. Appl. Catal. B: Environ. 2015, 172:7–17.

[86] Verbruggen, S. W., Keulemans, M., Filippousi, M., Flahaut, D., Van Tendeloo, D., Lacombe, S., *et al*. Plasmonic gold-silver alloy on TiO_2 photocatalysts with tunable visible-light activity. Appl. Catal. B: Environ. 2014; 156–157:116–21.

[87] Gou, X., Cheng, Y., Liu, B., Yang, B., Yan, X. Fabrication and photocatalytic properties of TiO_2/reduced graphene oxide/Ag nanocomposites with UV/Vis response. Eur. J. Inorg. Chem. 2015; 2015:2222–8.

[88] Linic, S., Christopher, P., Ingram, D. B. Plasmonic-metal nanostructures for efficient conversion of solar to chemical energy. Nat. Mater. 2011; 10(12):911–21.

[89] Wang, H., Zhang, L., Chen, Z., Hu, J., Li, S., Wang, Z., *et al*. Semiconductor heterojunction photocatalysts: Design, construction, and photocatalytic performances. Chem. Soc. Rev. 2014; 43(15):5234–44.

[90] Xu, H., Ouyang, S., Liu, L., Wang, D., Kako, T., Ye, J. Porous-structured Cu_2O/TiO_2 nanojunction material toward efficient CO_2 photoreduction. Nanotechnology 2014; 25(16):165402.

[91] Liu, D., Fernández, Y., Ola, O., Mackintosh, S., Maroto-Valer, M., Parlett, C. M., *et al*. On the impact of Cu dispersion on CO_2 photoreduction over Cu/TiO_2. Catal. Commun. 2012; 25:78–82.

[92] Wang, J., Ji, G., Liu, Y., Gondal, M. A., Chang, X. Cu_2O/TiO_2 heterostructure nanotube arrays prepared by an electrodeposition method exhibiting enhanced photocatalytic activity for CO_2 reduction to methanol. Catal. Commun. 2014; 46:17–21.

[93] Júnior, M. A. M., Morais, A., Nogueira, A. F. Boosting the solar-light-driven methanol production through CO_2 photoreduction by loading Cu_2O on TiO_2-pillared $K_2Ti_4O_9$. Microporous Mesoporous Mater. 2016; 234:1–11.

[94] In, S. I., Vaughn, D. D., Schaak, R. E. Hybrid CuO-$TiO_{2-x}N_x$ hollow nanocubes for photocatalytic conversion of CO_2 into methane under solar irradiation. Angew. Chem. Int. Ed. 2012; 51(16):3915–8.

[95] Beigi, A. A., Fatemi, S., Salehi, Z. Synthesis of nanocomposite CdS/TiO_2 and investigation of its photocatalytic activity for CO_2 reduction to CO and CH_4 under visible light irradiation. J. CO_2 Util. 2014; 7:23–9.

[96] Li, X., Liu, H., Luo, D., Li, J., Huang, Y., Li, H., *et al*. Adsorption of CO_2 on heterostructure CdS (Bi_2S_3)/TiO_2 nanotube photocatalysts and their photocatalytic activities in the reduction of CO_2 to methanol under visible light irradiation. Chem. Eng. J. 2012; 180:151–8.

[97] Qin, N., Liu, Y., Wu, W., Shen, L., Chen, X., Li, Z., *et al*. One-dimensional CdS/TiO_2 nanofiber composites as efficient visible-light-driven photocatalysts for selective organic transformation: Synthesis, characterization, and performance. Langmuir 2015; 31(3):1203–9.

[98] Song, G., Xin, F., Chen, J., Yin, X. Photocatalytic reduction of CO_2 in cyclohexanol on CdS/TiO_2 heterostructured photocatalyst. Appl. Catal. A: Gen. 2014; 473:90–5.

[99] Gao, X. F., Sun, W. T., Hu, Z. D., Ai, G., Zhang, Y. L., Feng, S., *et al*. An efficient method to form heterojunction CdS/TiO_2 photoelectrodes using highly ordered TiO_2 nanotube array films. J. Phys. Chem. C 2009; 113(47):20481–5.

[100] Brahimi, R., Bessekhouad, Y., Bouguelia, A., Trari, M. Visible light induced hydrogen evolution over the heterosystem Bi_2S_3/TiO_2. Catal. Today 2007; 122(1–2):62–5.

[101] Han, M., Jia, J. 3D Bi_2S_3/TiO_2 cross-linked heterostructure: An efficient strategy to improve charge transport and separation for high photoelectrochemical performance. J. Power Sources 2016; 329:23–30.

[102] Djouadi, L., Khalaf, H., Boukhatem, H., Boutoumi, H., Kezzime, A., Santaballa, J. A., *et al*. Degradation of aqueous ketoprofen by heterogeneous photocatalysis using Bi_2S_3/TiO_2-Montmorillonite nanocomposites under simulated solar irradiation. Appl. Clay Sci. 2018; 166:27–7.

[103] Liu, C., Yang, Y., Li, W., Li, J., Li, Y., Chen, Q. A novel Bi_2S_3 nanowire@TiO_2 nanorod heterogeneous nanostructure for photoelectrochemical hydrogen generation. Chem. Eng. J. 2016; 302:717–24.

[104] Kim, J., Kang, M. High photocatalytic hydrogen production over the band gap-tuned urchin-like Bi_2S_3-loaded TiO_2 composites system. Int. J. Hydrogen Energ. 2012; 37(10):8249–56.

[105] Ratanatawanate, C., Tao, Y., Balkus Jr, K. J. Photocatalytic activity of PbS quantum dot/TiO_2 nanotube composites. J. Phys. Chem. C 2009; 113(24):10755–60.

[106] Zhang, H., Gao, Y., Zhu, G., Li, B., Gou, J., Cheng, X. Synthesis of PbS/TiO_2 nanotubes photoelectrode and its enhanced visible light driven photocatalytic performance and mechanism for purification of 4-chlorobenzoic acid. Sep. Purif. Technol. 2019; 227:115697.

[107] Wang, P., Wang, L., Ma, B., Li, B., Qiu, Y. TiO_2 surface modification and characterization with nanosized PbS in dye-sensitized solar cells. J. Phys. Chem. B 2006; 110(29):14406–9.

[108] Wang, C., Thompson, R. L., Ohodnicki, P., Baltrus, J., Matranga, C. Size-dependent photocatalytic reduction of CO_2 with PbS quantum dot sensitized TiO_2 heterostructured photocatalysts. J. Mater. Chem. 2011; 21(35):13452–7.

[109] Tian, J., Sang, Y., Zhao, Z., Zhou, W., Wang, D., Kang, X., *et al*. Enhanced photocatalytic performances of CeO_2/TiO_2 nanobelt heterostructures. Small 2013; 9(22):3864–72.

[110] Muñoz-Batista, M. J., Gómez-Cerezo, M. N., Kubacka, A., Tudela, D., Fernández-García, M. Role of interface contact in CeO_2-TiO_2 photocatalytic composite materials. ACS Catal. 2014; 4(1):63–72.

[111] Yang, H., Zhang, K., Shi, R., Tang, A. Sol-gel synthesis and photocatalytic activity of CeO_2/TiO_2 nanocomposites. J. Am. Ceram. Soc. 2007; 90(5):1370–4.

[112] Jiao, J., Wei, Y., Zhao, Z., Liu, J., Li, J., Duan, A., *et al*. Photocatalysts of 3D ordered macroporous TiO_2-supported CeO_2 nanolayers: Design, preparation, and their catalytic performances for the reduction of CO_2 with H_2O under simulated solar irradiation. Ind. Eng. Chem. Res. 2014; 53(44):17345–54.

[113] Kamat, P.V., Fox, M.A. Photo-sensitization of TiO_2 colloids by Erythrosin-B in acetonitrile. Chem. Phys. Lett. 1983; 102:379–84.

[114] Patrick, B., Kamat, P.V. Photoelectrochemistry in semiconductor particulate systems. J. Phys. Chem. 1992; 96:1423–8.

[115] O'Regan, B., Graetzel, M. A low-cost, high-efficiency solar cell based on dye-sensitized colloidal TiO_2 films. Nature 1991; 353:737–40.

[116] Yang, M., Thompson, D.W., Meyer, G.J. Charge-transfer studies of iron cyano compounds bound to nanocrystalline TiO_2 surfaces. Inorg. Chem. 2002; 41:1254–62.

[117] Yu, J. C., Xie, Y., Tang, H. Y., Zhang, L., Chan, H. C., Zhao, J. Visible-light-assisted bactericidal effect of metal phthalocyanine-sensitized titanium dioxide films. J. Photochem. Photobiol. A: Chem. 2003; 156:235–41.

[118] Bae, E., Choi, W. Highly enhanced photoreductive degradation of perchlorinated compounds on dye-sensitized metal/TiO_2 under visible light. Environ. Sci. Technol. 2003; 37(1):147–52.

[119] Cho, Y., Choi, W., Lee, C. H., Hyeon, T., Lee, H. I. Visible light-induced degradation of carbon tetrachloride on dye-sensitized TiO_2. Environ. Sci. Technol. 2001; 35(5):966–70.

[120] Zhao, J., Wu, T., Wu, K., Oikawa, K., Hidaka, H., Serpone, N. Photoassisted degradation of dye pollutants. 3. Degradation of the cationic dye rhodamine B in aqueous anionic surfactant/TiO_2 dispersions under visible-light irradiation: Evidence for the need of substrate adsorption on TiO_2 particles. Environ. Sci. Technol. 1998; 32:2394–400.

[121] Rehman, S., Ullah, R., Butt, A., Gohar, N. D. Strategies of making TiO_2 and ZnO visible light active. J. Hazard. Mater. 2009; 170(2–3):560–9.

[122] Jiang, D., Xu, Y., Hou, B., Wu, D., Sun, Y. H. Synthesis of visible-light-activated TiO_2 photocatalyst via surface organic modification. J. Solid State Chem. 2007; 180:1787–91.

[123] Chen, F., Zou, W. W., Qu, W. W., Zhang, J. L. Photocatalytic performance of a visible-light TiO_2 photocatalyst prepared by a surface chemical modification process. Catal. Commun. 2009; 10:1510–3.

[124] Sampaio M. J., Silva C. G., Marques R. R. N., Silva A. M. T., Faria J. L. Carbon nanotube-TiO_2 thin films for photocatalytic applications. Catal. Today 2011; 161:91–6.

[125] Yu J., Ma T., Liu G., Cheng B. Enhanced photocatalytic activity of bimodal mesoporous titania powders by C60 modification. Dalton Trans. 2011; 40:6635–44.

[126] Wang F., Zhang K. Physicochemical and photocatalytic activities of self-assembling TiO_2 nanoparticles on nanocarbons surface. Curr. Appl. Phys. 2012; 12:346–52.

[127] Tang B., Hu G. X. Two kinds of graphene-based composites for photoanode applying in dye-sensitized solar cell. J. Power Sources 2012; 220:95–102.

[128] Tang B., Hu G. X. Preparation of few layers three-dimensional graphene networks by CVD for energy storage application. Chem. Vapor Depos. 2014; 20:14–22.

[129] Sun Y. F., Wang X. B., Tang B., Ban J. M., He Y. F., Huang W. Q., *et al.* Three-dimensional graphene networks modified photocatalyst with high performance under visible-light irradiation. Mater. Lett. 2017; 189:54–5

[130] Tang B., Hu G. X. Growth mechanism and influences from kinetic factors on carbon materials with Cu and silica substrates during atmospheric pressure chemical vapor deposition. J. Phys. Chem. C 2013; 117:25175–84.

[131] Novoselov, K. S., Geim, A. K., Morozov, S. V., Jiang, D., Zhang, Y., Dubonos, S. V. *et al.* Electric field effect in atomically thin carbon films. Science 2004; 306(5696):666–9.

[132] Neto A. H. C., Guinea F., Peres N. M. R., Novoselov K. S., Geim A. K. The electronic properties of graphene. Rev. Mod. Phys. 2009; 81:109–62.

[133] Mak, K. F., Sfeir, M. Y., Misewich, J. A., Heinz, T. F. The evolution of electronic structure in few-layer graphene revealed by optical spectroscopy. Proc. Natl. Acad. Sci. 2010; 107(34), 14999–5004.

[134] Xu Z. X., Gao H. Y., Hu G. X. Solution-based synthesis and characterization of a silver nanoparticle-graphene hybrid film. Carbon 2011; 49:4731–4738.

[135] Ton, N. N. T., Dao, A. T. N., Kato, K., Ikenaga, T., Trinh, D. X., Taniike, T. One-pot synthesis of TiO_2/graphene nanocomposites for excellent visible-light photocatalysis based on chemical exfoliation method. Carbon 2018; 133:109–17.

[136] Williams, G., Seger, B., Kamat, P. V. UV-assisted photocatalytic reduction of graphene oxide. ACS Nano 2008; 2:1487–917.

[137] Morales-Torres, S., Pastrana-Martínez, L. M., Figueiredo, J. L., Faria, J. L., Silva, A. M. Design of graphene-based TiO_2 photocatalysts-A review. Environ. Sci. Pollut. Res. 2012; 19(9):3676–3687.

[138] Liu, J., Wang, Z., Liu, L., Chen, W. Reduced graphene oxide as capturer of dyes and electrons during photocatalysis: Surface wrapping and capture promoted efficiency. Phys. Chem. Chem. Phys. 2011; 13(29):13216–21.

[139] Chen C., Cai W., Long M., Zhou B., Wu Y., Wu D., *et al.* Synthesis of visible-light responsive graphene oxide/TiO_2 composites with p/n heterojunction. ACS Nano 2010; 4:6425–32.

[140] Du A., Ng Y. H., Bell N. J., Zhu Z., Amal R., Smith S. C. Hybrid graphene/titania nanocomposite: Interface charge transfer, hole doping, and sensitization for visible-light response. J. Phys. Chem. Lett. 2011; 2:894–9.

[141] Zhang, L., Xi, Z., Xing, M., Zhang, J. Effects of the preparation order of the ternary P25/GO/Pt hybrid photocatalysts on hydrogen production. Int. J. Hydrogen Energ. 2013; 38(22):9169–77.

[142] Kamegawa, T., Yamahana, D., Yamashita, H. Graphene coating of TiO_2 nanoparticles loaded on mesoporous silica for enhancement of photocatalytic activity. J. Phys. Chem. C 2010; 114(35):15049–53.

[143] Perera, S. D., Mariano, R. G., Vu, K., Nour, N., Seitz, O., Chabal, Y., *et al*. Hydrothermal synthesis of graphene-TiO_2 nanotube composites with enhanced photocatalytic activity. Acs Catal. 2012; 2(6):949–56.

[144] Bai, X., Zhang, X., Hua, Z., Ma, W., Dai, Z., Huang, X., *et al*. Uniformly distributed anatase TiO_2 nanoparticles on graphene: Synthesis, characterization, and photocatalytic application. J. Alloys Compd. 2014; 599:10–8.

[145] Zhang H., Lv X., Li Y., Wang Y., Li J. P25-graphene composite as a high performance photocatalyst. ACS Nano 2010; 4:380–6.

[146] Liang Y., Wang H., Casalongue H. S., Chen Z., Dai H. TiO_2 Nanocrystals grown on graphene as advanced photocatalytic hybrid materials. Nano Res. 2010; 3:701–5.

[147] Liu J., Bai H., Wang Y., Liu Z., Zhang X., Sun D. D. Self-assembling TiO_2 nanorods on large graphene oxide sheets at a two-phase interface and their anti-recombination in photocatalytic applications. Adv. Funct. Mater. 2010; 20:4175–81.

[148] Shen J., Yan B., Shi M., Ma H., Li N., Ye M. One step hydrothermal synthesis of TiO_2-reduced graphene oxide sheets. J. Mater. Chem. 2011; 21:3415–21.

[149] Li, X. L., Peng, Q., Yi, J. X., Wang, X., Li, Y. Near monodisperse TiO_2 nanoparticles and nanorods. Chem. Eur. J. 2006; 12(8):2383–91.

[150] Xu, J., Ge, J. P., Li, Y. D. Solvothermal synthesis of monodisperse PbSe nanocrystals. J. Phys. Chem. B 2006; 110(6):2497–501.

[151] Wang, X., Zhuang, J., Peng, Q., Li, Y. A general strategy for nanocrystal synthesis. Nature 2005; 437(7055):121–4.

[152] Li, K., Xiong, J., Chen, T., Yan, L., Dai, Y., Song, D., *et al*. Preparation of graphene/TiO_2 composites by nonionic surfactant strategy and their simulated sunlight and visible light photocatalytic activity towards representative aqueous POPs degradation. J. Hazard. Mater. 2013; 250:19–28.

[153] Taguchi, T., Saito, Y., Sarukawa, K., Ohno, T., Matsumura, M. Formation of new crystal faces on TiO_2 particles by treatment with aqueous HF solution or hot sulfuric acid. New J. Chem. 2003; 27(9):1304–6.

[154] Sugimoto, T., Zhou, X., Muramatsu, A. Synthesis of uniform anatase TiO_2 nanoparticles by gel-sol method: 4. Shape control. J. Colloid Interface Sci. 2003; 259(1):53–61.

[155] Kanie, K., Sugimoto, T. Shape control of anatase TiO_2 nanoparticles by amino acids in a gel-sol system. Chem. Commun. 2004; 14:1584–5.

[156] Dai, Y., Cobley, C. M., Zeng, J., Sun, Y., Xia, Y. Synthesis of anatase TiO_2 nanocrystals with exposed {001} facets. Nano Lett. 2009; 9(6):2455–9.

[157] Gu, L., Wang, J., Cheng, H., Zhao, Y., Liu, L., Han, X. One-step preparation of graphene-supported anatase TiO_2 with exposed {001} facets and mechanism of enhanced photocatalytic properties. ACS Appl. Mater. Interfaces 2013; 5(8):3085–93.

[158] Taguchi, T., Saito, Y., Sarukawa, K., Ohno, T., Matsumura, M. Formation of new crystal faces on TiO_2 particles by treatment with aqueous HF solution or hot sulfuric acid. New J. Chem. 2003; 27(9):1304–6.

[159] Sun, L., Zhao, Z., Zhou, Y., Liu, L. Anatase TiO_2 nanocrystals with exposed {001} facets on graphene sheets via molecular grafting for enhanced photocatalytic activity. Nanoscale 2012; 4(2):613–20.

[160] Yang, H. G., Liu, G., Qiao, S. Z., Sun, C. H., Jin, Y. G., Smith, S. C., *et al*. Solvothermal synthesis and photoreactivity of anatase TiO_2 nanosheets with dominant {001} facets. J. Am. Chem. Soc. 2009; 131(11):4078–83.

[161] Cai, D., Lian, P., Zhu, X., Liang, S., Yang, W., Wang, H. High specific capacity of TiO_2-graphene nanocomposite as an anode material for lithium-ion batteries in an enlarged potential window. Electrochim. Acta 2012; 74:65–72.

[162] Sugimoto, T., Okada, K., Itoh, H. Synthetic of uniform spindle-type titania particles by the gel-sol method. J. Colloid Interface Sci. 1997; 193(1997):140–3.

[163] Sugimoto, T., Okada, K., Itoh, H. Formation mechanism of uniform spindle-type titania particles in the gel-sol process. J. Disper. Sci. Tech. 1998; 19(2–3):143–61.

[164] Brinker, C. J., Scherer, G. W. Sol-gel science: The physics and chemistry of sol-gel processing. Academic press. 1990.

[165] Burda, C., Chen, X., Narayanan, R., El-Sayed, M. A. Chemistry and properties of nanocrystals of different shapes. Chem. Rev. 2005; 105(4):1025–102.

[166] Hamadanian, M., Rostami, M., Jabbari, V. Graphene-supported C-N-S tridoped TiO_2 photo-catalyst with improved band gap and charge transfer properties. J. Mater. Sci.: Mater. Electron. 2017; 28(20):15637–46.

[167] Wang, D., Choi, D., Li, J., Yang, Z., Nie, Z., Kou, R., *et al*. Self-assembled TiO_2-graphene hybrid nanostructures for enhanced Li-ion insertion. ACS nano 2009; 3(4):907–14.

[168] Liu, S., Sun, H., Liu, S., Wang, S. Graphene facilitated visible light photodegradation of methylene blue over titanium dioxide photocatalysts. Chem. Eng. J. 2013; 214:298–303.

[169] Liu, X., Pan, L., Lv, T., Zhu, G., Lu, T., Sun, Z., *et al*. Microwave-assisted synthesis of TiO_2-reduced graphene oxide composites for the photocatalytic reduction of Cr(VI). RSC Adv. 2011; 1(7):1245–9.

[170] Xu, T., Zhang, L., Cheng, H., Zhu, Y. Significantly enhanced photocatalytic performance of ZnO via graphene hybridization and the mechanism study. Appl. Catal. B: Environ. 2011; 101(3–4): 382–7.

[171] Larciprete, R., Fabris, S., Sun, T., Lacovig, P., Baraldi, A., Lizzit, S. Dual path mechanism in the thermal reduction of graphene oxide. J. Am. Chem. Soc. 2011; 133(43):17315–21.

CHAPTER 2: Synthesis of TiO_2/graphene nanocomposites based on chemical exfoliation method.

Abstract

Facile electron-hole recombination and the broad band gap are two major bottlenecks of titanium dioxide (TiO_2) applied in visible-light photocatalysis. Hybridization of TiO_2 with graphene is a promising strategy to alleviate these drawbacks. In this paper, we demonstrate a novel technique to synthesize TiO_2/graphene nanocomposites without the use of graphene oxide (GO). Graphene dispersion was obtained through the chemical exfoliation of graphite in titanium tetra-*n*-butoxide by ultrasonication. The dispersion was directly used for the sol-gel reaction in the presence of different catalysts, affording TiO_2/graphene nanocomposites featured with several advantages: i) the formation of a TiO_2 nano layer that uniformly and thinly covered graphene sheets, ii) a trace amount of defects on graphene sheets, iii) a significant extension of the absorption edge into the visible light region, and iv) a dramatic suppression of electron-hole recombination. When tested for methylene blue decomposition under visible light, our nanocomposites exhibited the photocatalytic activity 15 and 5 times greater than that of TiO_2-P25 and a conventional GO-based nanocomposite, respectively.

Chapter 2

2.1. Introduction

The advantages of TiO_2 as a photocatalyst are recognized by its superior properties including chemical stability [1], strong oxidizing power [2], and nontoxicity, as well as a wide spectrum of applications in solar cell [3], gas sensor [4], optoelectronic devices [5], and so on. However, the broad band gap (3.2 eV) and a short lifetime of photoexcited electron-hole pairs (2 to 3 μs) [6] are the major drawbacks of TiO_2 in visible-light photocatalysis. Since the early 2000's, considerable efforts have been devoted to lighten the said shortfalls of TiO_2. For example, implanting with foreign metal ions or non-metals [7–12] can narrow the band gap of TiO_2. Tailored heterojunction with other semiconductors [13,14], noble metal doping [15–17], and grafting of organic chelating ligands [18–20] are effective ways to improve the charge carrier separation. Among these modifications, graphene is the newest material to be paired with TiO_2. In addition to the extremely high specific surface area as a support [21–23], graphene plays a role in collecting photoexcited electrons from the conduction band of TiO_2 [24]. The appropriate work function of graphene (4.42 eV) [25], as well as the 2D π-conjugate structure, ensures the effective charge carrier separation.

Owing to the expected advantages of the TiO_2/graphene nanocomposites in visible-light photocatalysis, a variety of synthetic approaches have been explored, in which most of the fabrication processes have employed graphene oxide (GO) as a starting material. GO was coupled with TiO_2 and then or simultaneously reduced to graphene by chemical [26–29], thermal [30,31], solvothermal [25,32], microwave-assisted [33], or photochemical [34,35] reduction. Nevertheless, the use of a reduction process to prepare graphene can generate a non-negligible amount of defects on the graphene framework including vacancies [36] and residual oxygen-containing functional groups [37,38]. A large amount of defects on the graphene framework unavoidably affect the electronic properties of the

nanocomposites by introducing scattering centers and decreasing the ballistic transport path length. Thus, the defect-rich graphene can obstruct the charge carrier separation probability in the TiO_2/graphene nanocomposites [39]. In addition, the sensitivity of titanium alkoxide to water (GO usually contains) significantly impedes the uniform and controlled growth of TiO_2 on graphene [40]. To the best of my knowledge, these problems are still challenging in the fabrication of TiO_2/graphene nanocomposites. It is expected that minimization of defects on graphene sheets lets the photoexcited electrons be more successfully stored and shuttled away from the TiO_2/graphene interfaces [41,42]. Moreover, the interfacial contact between graphene sheets and nano-sized TiO_2 particles or films is also considered as a crucial factor for the effective transfer of photoexcited electrons [43,44].

In this chapter, I propose a novel GO-free route to synthesize TiO_2/graphene nanocomposites, starting from a graphene dispersion in titanium alkoxide. The dispersion was obtained using the chemical exfoliation of graphite in titanium tetra-*n*-butoxide with the aid of ultrasonication. To the obtained dispersion, an aqueous solution of a catalyst was added for promoting the sol-gel reaction in the presence of dispersed graphene sheets and eventually affording TiO_2/graphene nanocomposites with defect-less graphene sheets uniformly and thinly covered by a TiO_2 nano layer. The nanocomposites presented a significant extension of the absorption edge into the visible-light region as well as dramatically enhancement in the electron-hole separation efficiency. The visible-light photocatalytic ability of the nanocomposites was tested in the methylene blue degradation, in which the developed TiO_2/graphene nanocomposites exhibited the activity 15 times greater than TiO_2-P25 and 5 times greater than a conventional GO-based nanocomposite.

2.2. Materials and methods

2.2.1. Materials

Graphite powder (≥ 98%, 45 μm) and benzylamine (> 98%) were obtained from Wako Pure Chemical Industries, aqueous ammonia solution (NH_3) (28–30%) from Kanto Chemical, and titanium tetra-*n*-butoxide (Ti(O*n*Bu)$_4$, ≥ 97%) from Sigma Aldrich. Graphene nanoplatelets (GNP) (Strem Chemicals) with the surface area of 750 m^2 g^{-1} and anatase TiO_2-TKP 101 (Tayca) with the primary crystallite size of 6 nm were used to estimate the graphene content in TiO_2/graphene nanocomposites. A commercial photocatalyst, TiO_2-P25 (Sigma Aldrich) with the primary crystallite size of 21 nm was utilized after calcination at 400 °C for 2 h under nitrogen as a reference sample. Hexane and acetone (Kanto Chemical) were used after being dried over molecular sieves 4A under nitrogen bubbling. 1,2-dichlorobenzene (> 99%) was obtained from TCI Chemicals. Methylene blue (MB) (≥ 98.5%) was obtained from Kanto Chemical, which was used as a dye for the photocatalytic test. GO was prepared from graphite powder using the modified Hummers method [45]. It was used as a graphene source to prepare a conventional nanocomposite, *i.e.* TiO_2/reduced graphene oxide (termed as TiO_2/rGO).

2.2.2. Synthesis of TiO_2/graphene nanocomposites

2.2.2.1 Preparation of graphene dispersion in Ti(OnBu)$_4$

A graphene dispersion in Ti(O*n*Bu)$_4$ was prepared from graphite by a chemical exfoliation method [46]. Briefly, 44.0 mg of graphite was sonicated in 5.5 mL of Ti(O*n*Bu)$_4$ at 43 kHz and 60 °C for 4 h under N_2 atmosphere. The resultant black mixture was centrifuged at 3000 rpm for 4 h in order to precipitate non-exfoliated graphite. Finally, a graphene dispersion in Ti(O*n*Bu)$_4$ at 0.18 mg/mL was obtained as the supernatant. For

comparison, a graphene dispersion was also prepared in benzylamine, which is one of the most widely used exfoliating solvents [47,48].

2.2.2.2 Synthesis of TiO_2/graphene nanocomposites using the sol-gel process

A TiO_2/graphene nanocomposite was obtained via the sol-gel method from the graphene dispersion in Ti(O*n*Bu)$_4$. The synthetic procedure was as follows: H_2O or aqueous NH_3 mixed with benzylamine at different volume ratios (total 5.0 mL) was dropwise added into 5.0 mL of the graphene dispersion in Ti(O*n*Bu)$_4$ under vigorous magnetic stirring and N_2 atmosphere. After 2 h of the reaction at room temperature, a grayish gel was obtained, which was subsequently washed with anhydrous hexane and acetone for three times, alternately. Finally, the precipitate was fully dried in vacuum at 70 °C for 12 h. All of the TiO_2/graphene nanocomposites prepared in this chapter are summarized in Table 2.1.

Table 2.1. Synthetic conditions for TiO_2/graphene nanocomposites.

Sample	Catalyst for the sol-gel reaction[a]	Powder appearance
TG-H_2O	Only H_2O	Non-uniform, grayish
TG-H_2O/9BA	H_2O/BA (1/9 v/v)	Uniform, yellowish
TG-NH_3	Only *aq.* NH_3	Non-uniform, grayish
TG-NH_3/1BA	*aq.* NH_3/BA (1/1 v/v)	Uniform, yellowish
TG-NH_3/3BA	*aq.* NH_3/BA (1/3 v/v)	
TG-NH_3/5BA	*aq.* NH_3/BA (1/5 v/v)	
TG-NH_3/5BA (washed)[b]	*aq.* NH_3/BA (1/5 v/v)	Uniform, yellowish

[a] Benzylamine is abbreviated as BA.
[b] Obtained by additionally washing TG-NH_3/5BA with methanol for 3 times.

2.2.2.3 Preparation of TiO_2/rGO nanocomposite

For comparison, a TiO_2/rGO nanocomposite was also synthesized by following the procedure reported by Jiang et al. [49]: 1.0 mg of GO was dispersed in 36.7 mL of methanol by ultrasonic treatment at 43 kHz and room temperature for 30 min, and then 5.7 mL of

$Ti(OnBu)_4$ was dropwise added into the dispersion under stirring and N_2 atmosphere for 1 h. Thereafter, the mixture was transferred under nitrogen into a Teflon-lined autoclave (100 mL) and subjected to a solvothermal treatment at 180 °C for 24 h, followed by natural cooling to room temperature. The precipitate was collected by centrifugation at 4000 rpm, then washed thoroughly by ethanol and DI water for three times alternately. After drying in vacuum at 80 °C for 12 h, the product was calcined at 400 °C for 2 h under nitrogen. The obtained sample is denoted as TiO_2/rGO.

2.2.3. Characterizations

The Raman spectra of graphene in the dispersion and the nanocomposites were recorded on a laser Raman spectrometer (NRS-4100, JASCO) with a 532 nm laser. The graphene dispersion in $Ti(OnBu)_4$ as well as that in benzylamine (for a comparison purpose) were dropped on a glass slide and dried under nitrogen flow at room temperature prior to the measurements. The measurements were carried out using the slit of 100 × 8000 μm with the exposure time of 80 s and 50 accumulations. In the case of the nanocomposites, dried powder samples were directly placed on a glass slide. The measurements were executed using the slit of 10 × 8000 μm with the exposure time of 30 s and 10 accumulations. For the Raman-active modes of TiO_2, the E_g bands are related to the symmetric stretching vibration of O−Ti−O bonds, while the B_{1g} and A_{1g} bands are attributed to the symmetric and asymmetric bending vibrations of O−Ti−O [50–52]. In the case of graphene, the G band provides information on the in-plane vibration of sp^2 carbon atoms [53], while the D band suggests the presence of defects on the graphene sheets [54]. The intensity ratio of the D and G bands (I_D/I_G) is a measure of the concentration of defects with respect to the sp^2 hybridized graphene domains [55]. The broadness and shift of the 2D band can be utilized to estimate the number of the graphene layers [56].

The thickness of graphene samples was measured by an atomic force microscope (AFM, HITACHI SII SPI-3800/SPA400) equipped with a SI-DF40 cantilever. A graphene dispersion was diluted in *o*-dichlorobenzene, then casted on a SiO_2/Si substrate under N_2 atmosphere, and finally washed by anhydrous hexane and dried at 70 °C prior to the measurements. Images were obtained based on dynamic force mapping at a scan rate of 1.5 Hz and a resolution of 512 pixels and 512 lines.

The appearance of the nanocomposites was captured by a digital microscope (VHX-900F, KEYENCE), in which a dried powder sample was loaded on a glass slide. The images were captured using a 1/1.8-inch CMOS image sensor with the resolution of 1600 × 1200 pixels. The morphology of the nanocomposites was studied by a transmission electron microscope (TEM) (H-7100, HITACHI) operated at a voltage of 100 kV and a high-resolution TEM (HR-TEM, HITACHI H-9000NAR) operated at 300 kV. A carbon-coated copper grid was used as a sample holder. A powder sample was suspended in methanol, then cast onto the grid and dried overnight at room temperature prior to the measurements. Fourier-transformed infrared (FTIR) spectra were acquired on JASCO FT/IR-6100 at room temperature and over the range of 4000–400 cm^{-1} with a resolution of 4 cm^{-1}. KBr pellets were prepared from powder samples (1.0 wt%) thoroughly ground with dried KBr. X-ray diffraction (XRD) patterns were acquired in a reflection geometry on a Rigaku Smartlab X-ray diffractometer using a Cu Kα radiation (1.542 Å) at a voltage of 40 kV and a current of 30 mA. The measurements were performed at room temperature in the range of 2θ of 10–80º with a scan speed of 0.3º min^{-1}.

UV-Vis spectra were recorded in the diffuse reflectance (DRS) mode for the powder samples and in the transmittance mode to measure the concentration of a MB solution for photocatalysis. The UV-Vis DRS spectra of the powder samples were obtained on a UV-Vis spectrometer (V630, JASCO) equipped with an ISN-470 integrating sphere assembly. The

powder samples were thoroughly ground by mortar and pestle and then loaded into a quartz cuvette. The measurements were performed in the range of 300-800 nm at a resolution of 2 nm and a scanning rate of 100 nm min^{-1}, where a $BaSO_4$ plate was used as the background. The reflectance spectra were converted to the absorption spectra according to the Kubelka-Munk (K-M) function ($F(R_\infty)$). The optical band gap was derived from the Tauc equation (Equation 2.1) [57],

$$(h\upsilon F(R_\infty))^{1/n} = A\,(h\upsilon - E_{bandgap}) \qquad (2.1)$$

where h is the Plank constant, υ is the photon frequency, and A is a proportion constant. The exponent ($1/n$) reflects the nature of the electron transition [58] and is set to ½ in the case of TiO_2 (corresponding to an indirect transition). The band gap is obtained as the x-intercept of a linear part of $(h\upsilon F(R_\infty))^{1/2}$ as a function of $h\upsilon$. The UV-Vis DRS spectra were also used for the estimation of the graphene content in the TiO_2/graphene nanocomposites: The absorbance at 750 nm was converted into the graphene content in wt% based on a calibration curve, which was derived by separate measurements for TiO_2-TKP 101 ground with 0.02–0.08 wt% of GNP. In determining the concentration of MB, the absorbance at 665 nm was used.

Photoluminescence (PL) emission spectra were recorded at room temperature on a spectrofluorometer (FP-6500, JASCO) equipped with a powder holder accessory. The excitation wavelength was set at 300 nm, and the emission spectra were collected from 360 to 520 nm at the scanning rate of 50 nm/min, the excitation and emission bandwidths of 5 nm, and the response time of 2 s.

2.2.4. Photocatalytic test

The photocatalytic degradation of MB was chosen as a model reaction to evaluate the photocatalytic activity of the samples. A specified amount of catalyst powder was

suspended in 25 mL of an aqueous solution of MB at 50 mg/L. The suspension was kept in dark under constant stirring for 12 h to ensure the adsorption/desorption equilibrium. After reaching the equilibrium, 2.0 mL of the suspension was extracted in order to determine the concentration of MB in the supernatant. Then, the suspension was irradiated under visible light for 6 h, where temperature was maintained at room temperature. The light source was provided by a light irradiator (MAX-303, Asahi spectra) using a 300 W xenon short arc lamp and a 422 nm longpass filter. A guide light rod unit (LG series, Asahi spectra) was inserted in the suspension at the location of 4 cm away from the reactor bottom. During the irradiation, 2.0 mL of the MB solution was sampled every 2 h to track the concentration of MB. The photocatalytic activity of a catalyst was evaluated by the amount of MB decomposed per gram of the catalyst per hour. The activity was reported as an average of at least three catalytic tests per sample.

2.2.5. Investigation of active species

Active species produced in the TiO_2/graphene photocatalysts under the visible light were investigated by adding different types of scavengers. Tert-butyl alcohol, ammonium oxalate, and benzoquinone were used as scavengers for hydroxyl radicals, holes, and superoxide radicals, respectively. A scavenger which lets the activity of a catalyst reduced by its addition dictates the importance of the corresponding active species. The photodegradation of MB was utilized to investigate the inhibition effect. In brief, 25 mg of a catalyst was dispersed in 25 mL of an aqueous MB solution at 100 ppm. After stirring in dark for 12 h to achieve the adsorption/desorption equilibrium, a specified amount of a scavenger was added into the dispersion before irradiation (24 μL for tert-butyl alcohol, 7.8 mg of ammonium oxalate, and 0.3 mg of benzoquinone). During the reaction, 2.0 mL of the MB solution was sampled to track the consumption of MB every 40 minutes.

2.3. Results and discussion

2.3.1. Synthesis of the TiO_2/graphene nanocomposites

The quality of graphene, that was obtained by chemical exfoliation, was investigated by Raman spectroscopy (Figure 2.1a). It was found that the quality of graphene produced in Ti(O*n*Bu)$_4$ was superior to that produced in benzylamine, in which a sharp 2D band with a relatively low FWHM value (28 cm^{-1}) suggested successful preparation of bi-layer graphene [59] in Ti(O*n*Bu)$_4$. In the case of graphene prepared in benylamine, the broadening of the 2D band together with a relatively high FWHM value (70 cm^{-1}) indicated the formation of few-layer graphene [59]. Lorentzian fitting for the 2D band supported the formation of bi-layer graphene when prepared from Ti(O*n*Bu)$_4$ and few-layer graphene for benzylamine (Figure 2.1b,c). AFM was also employed to determine the layer number of the exfoliated graphene. The acquired AFM images are shown in Figure 2.2. It is known that the thickness of graphene layers measured by AFM depends on the substrates, *i.e.* on a SiO_2/Si substrate the thickness of single-layer graphene (SLG) is around 1 nm [60], while on mica it is around 0.4 nm [61]. This difference is generally related to the interaction of graphene with the substrate and the AFM probe [62]. It is possible to determine the layer number by measuring the thickness of graphene sheets and then dividing it by the thickness of SLG. The graphene prepared using Ti(O*n*Bu)$_4$ exhibited the thickness around 2 nm, corresponding to bi-layers on the employed SiO_2/Si substrate. On the other hand, the thickness of the graphene produced using benzylamine was measured as *ca.* 4 nm, corresponding to four layers. Thus, the AFM results were highly consistent with the estimation from the 2D band of Raman spectroscopy. In addition, Ti(O*n*Bu)$_4$ also exhibited its potentiality to produce high-quality graphene. As shown in Figure 2.1a, the I_D/I_G ratio of

graphene prepared in Ti(O*n*Bu)$_4$ was 0.20, much lower than 0.69 for graphene produced in benylamine, and than values reported in literature such as 0.67 for electrochemical exfoliation of graphite [63,64], over 0.87 for reduced graphene oxide [65–67], and over 1.6 for pyrolysis-based graphene [68,69]. It is also noted that the spectrum of graphene produced in Ti(O*n*Bu)$_4$ was free from the D' band, while it existed at 1620 cm^{-1} for graphene prepared in benzylamine [70,71]. These results revealed the excellent performance of Ti(O*n*Bu)$_4$ for the production of a high-quality graphene, which is indeed an ideal precursor for the synthesis of TiO_2/graphene nanocomposites (as demonstrated below).

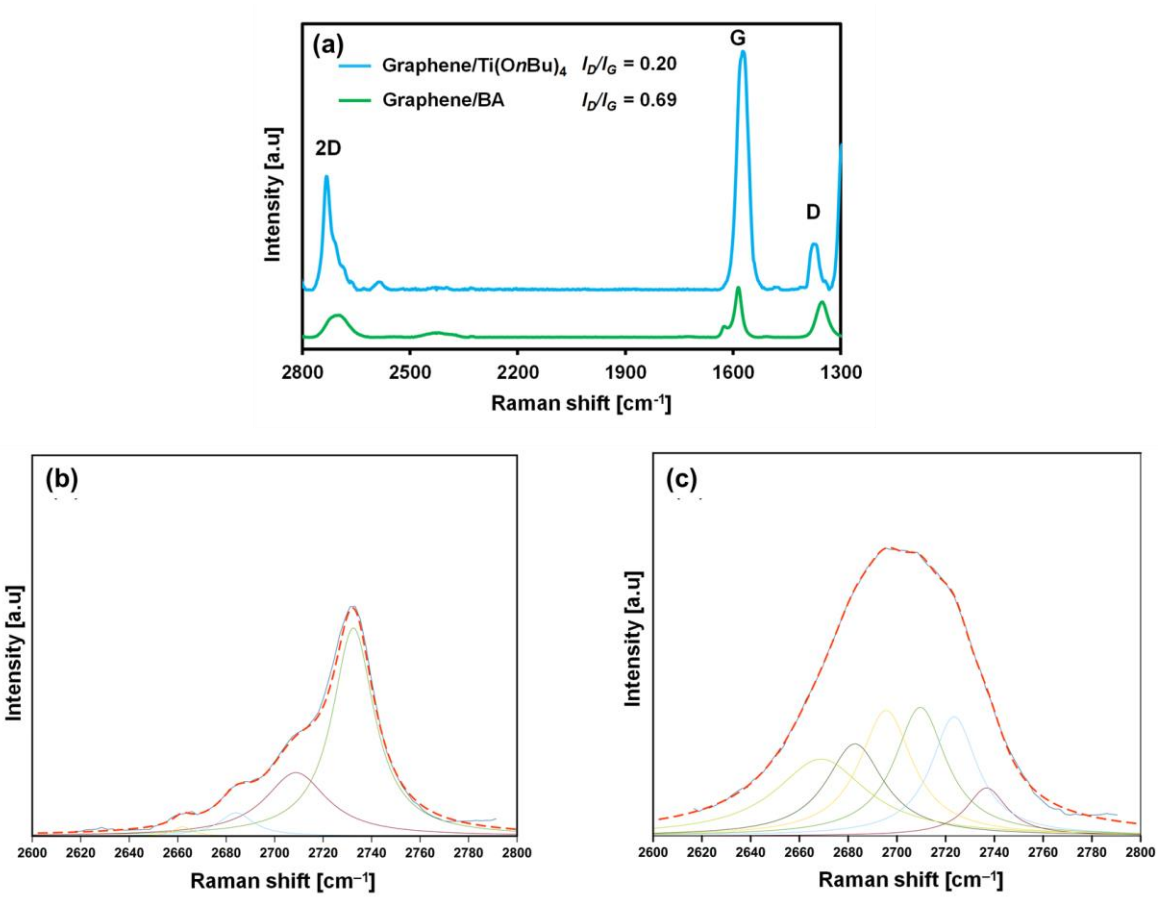

Figure 2.1. a) Raman spectra of graphene prepared using Ti(O*n*Bu)$_4$ and benzylamine. The 2D band of the graphene prepared using b) Ti(O*n*Bu)$_4$, and c) benzylamine was fitted with four and six Lorentzian components, corresponding to bi-layer and few-layer graphene, respectively [72,73].

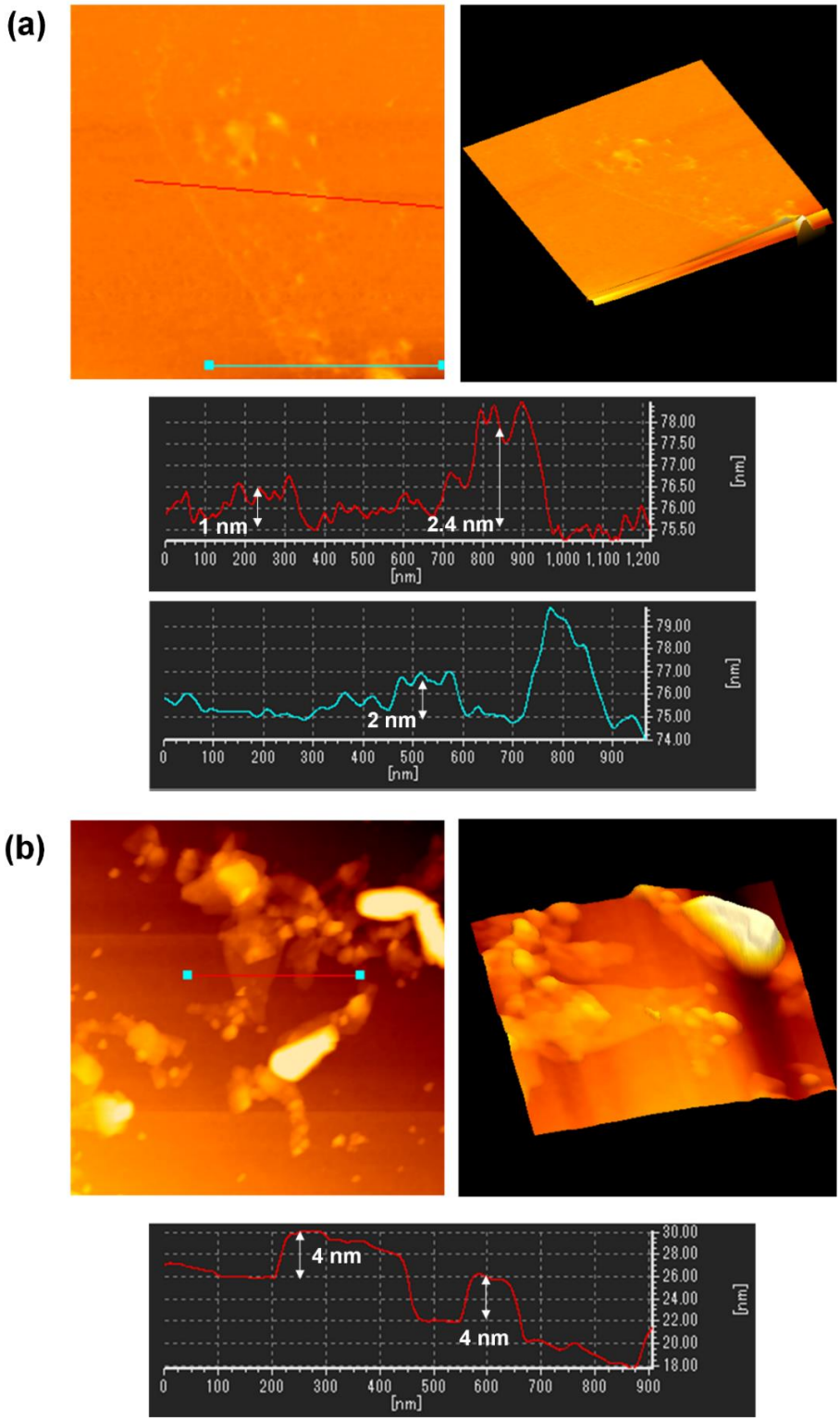

Figure 2.2. AFM images and line profiles for graphene prepared using a) Ti(O*n*Bu)$_4$ and b) benzylamine.

In performing the sol-gel reaction, a variety of conditions was examined in order to convert Ti(O*n*Bu)$_4$ into TiO_2 without losing the uniformity of the dispersion. Obviously, the dropwise addition of pure water or an aqueous NH_3 solution caused sedimentation of graphene as graphite before being embedded in the TiO_2 matrix, thus leading to a non-uniform white/black precipitate (Figure 2.3). A successful sol-gel reaction was performed when water or aqueous NH_3 was mixed with benzylamine, a catalyst having an exfoliation ability by itself. The dropwise addition of this mixture afforded uniform precipitates (Figure 2.3).

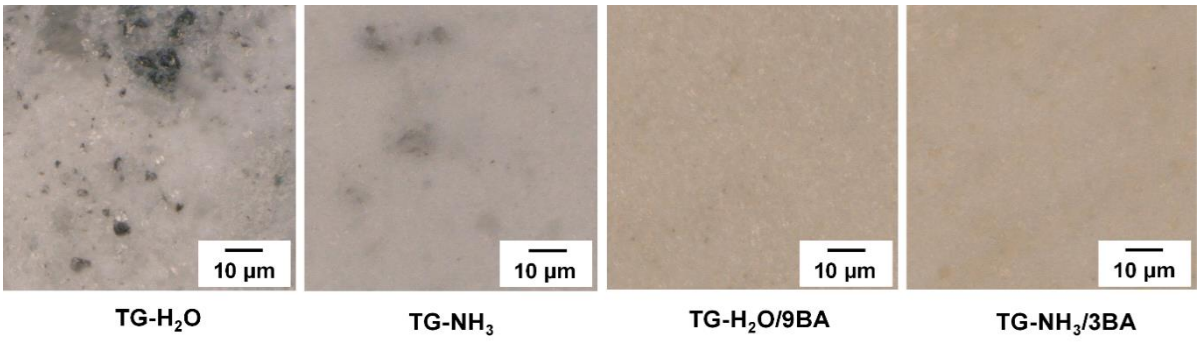

Figure 2.3. Optical microscope images of TiO_2/graphene precipitates prepared in different conditions.

Figure 2.4a shows the FTIR spectra of the TiO_2/graphene nanocomposites prepared in different conditions. An intense and broad band in the range of 515–480 cm^{-1} was ascribed to the vibration of Ti–O of TiO_2 [74]. The peaks in 2940-2839 cm^{-1} (attributed to aliphatic C–H stretching vibration [75]) and the peak at 721 cm^{-1} (the rocking vibration of CH_3 groups [76]) indicated the presence of unreacted butoxide, which was significantly reduced in the presence of NH_3. When benzylamine was added, the resultant nanocomposites also contained residual peaks of benzylamine such as 1364 cm^{-1} for the C–N stretching [77,78],

1193, 1104, and 1028 cm^{-1} for the C–H in-plane ring bending [79], and 698 cm^{-1} for the C–H out-of-plane bending [80]. This residual benzylamine was never completely removed, even when the product was subjected to additional washing with methanol, and it was likely that a part of benzylamine was tightly immobilized in the product during the fabrication process. The formation of TiO_2 from the graphene dispersion in Ti(O*n*Bu)$_4$ was also confirmed in the Raman spectra of TG-H_2O/9BA and TG-NH_3/9BA nanocomposites (Figure 2.4b). The specific vibration modes located at 141 cm^{-1} [$E_g(1)$], 396 cm^{-1} [$B_{1g}(1)$], 514 cm^{-1} [$A_{1g} + B_{1g}(2)$], and 637 cm^{-1} [$E_g(2)$] indicated the formation of TiO_2 in the anatase form [81]. In addition to the TiO_2 modes, the D, G and 2D bands of graphene appeared at 1340, 1600 and 2615 cm^{-1}. The I_D/I_G ratio of the TiO_2/graphene nanocomposites synthesized in the presence of benzylamine was 0.29 for TG-H_2O/9BA and 0.21 for TG-NH_3/3BA nanocomposites, which were much smaller than 0.93 for the conventional TiO_2/rGO nanocomposite. These results confirmed the successful synthesis of the TiO_2/graphene nanocomposites with a greatly reduced amount of defects on the graphene framework. Figure 2.4c plots XRD patterns of TG-H_2O/9BA and TG-NH_3/3BA nanocomposites. Broad diffraction peaks were observed at 27.8º, 47.1º, and 62.5º, corresponding to the formation of TiO_2 in the anatase form. The broadness of the peaks was attributed to the formation of nano-sized crystallites.

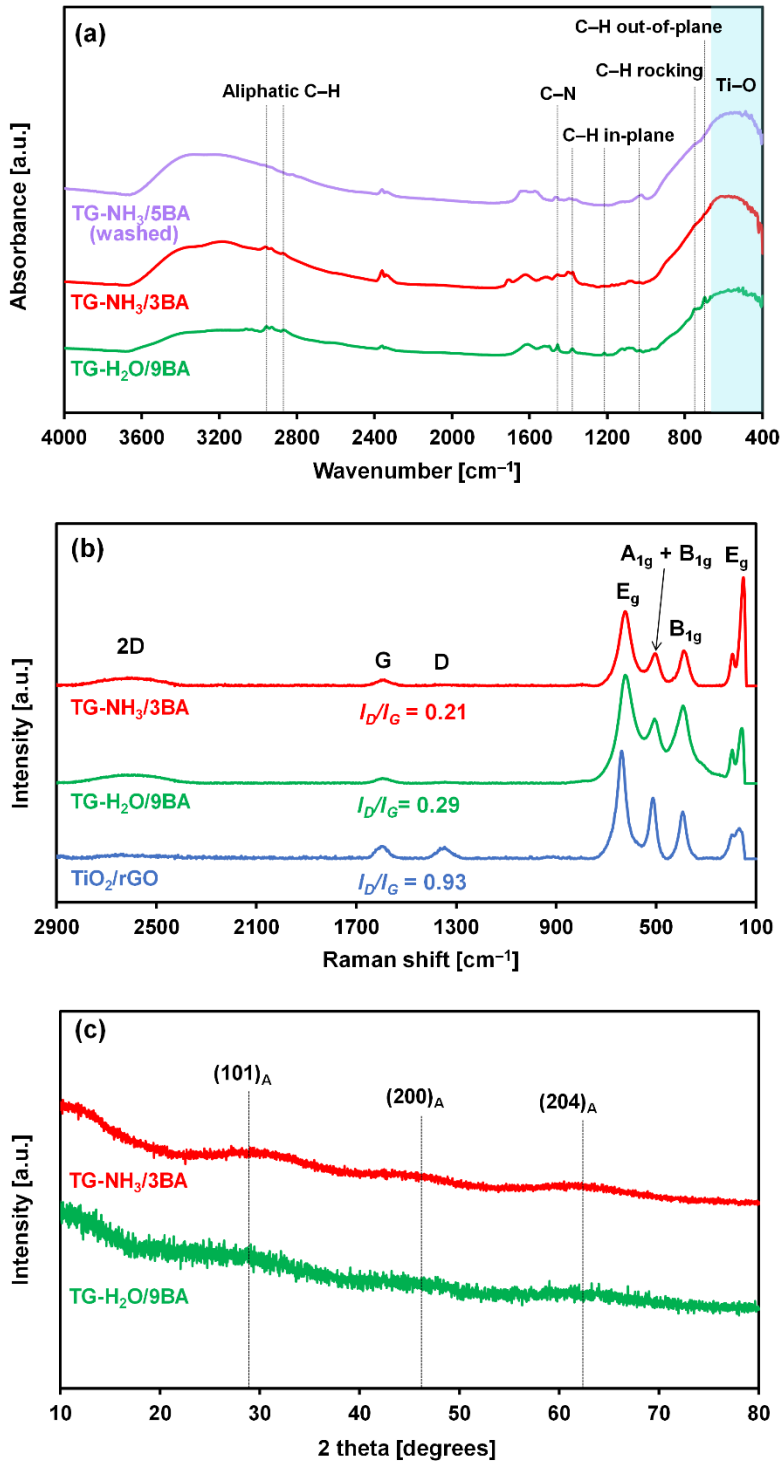

Figure 2.4. a) FTIR spectra, b) Raman spectra, and c) XRD patterns of TiO_2/graphene nanocomposites synthesized from a graphene dispersion in Ti(O*n*Bu)$_4$ under different conditions. As a reference, the Raman spectrum of a TiO_2/rGO nanocomposite prepared based on a conventional solvothermal method is added in b).

In Figure 2.5, TEM images of the TiO_2/graphene and TiO_2/rGO reference nanocomposites are compared. The morphology of the two types of the nanocomposites was found to be completely different: When the nanocomposites were prepared from the graphene dispersion in Ti(O*n*Bu)$_4$, the morphology was represented by sheet-like structures, and the periphery of these thin sheets was decorated by a layer with the thickness ranging from below 1 nm to 5 nm. It was suggested that the nanocomposites were composed by isolated graphene sheets that were uniformly and thinly covered by a TiO_2 nano layer. A HR-TEM image of the TG-NH_3/3BA nanocomposite (Figure 2.5g) displays a sheet-like morphology, and a magnified image detects the lattice fringe of *ca*. 0.35 nm, corresponding to that of the anatase (101) plane [82,83]. In contrast, the TiO_2/rGO reference nanocomposite consisted of agglomerated granular particles of *ca.* 10–20 nm, where the presence of sheet-like structures was hardly observed. As was reported in literature, the presence of water in GO could cause the formation and sedimentation of TiO_2 without preferential growth on graphene sheets [38]. Thus, it became evident that by starting from a uniform mixture of the two components, I could create a promising morphology for effective charge carrier separation, *i.e.* the largest interfacial connection with a short passage of carriers in TiO_2 [84,85].

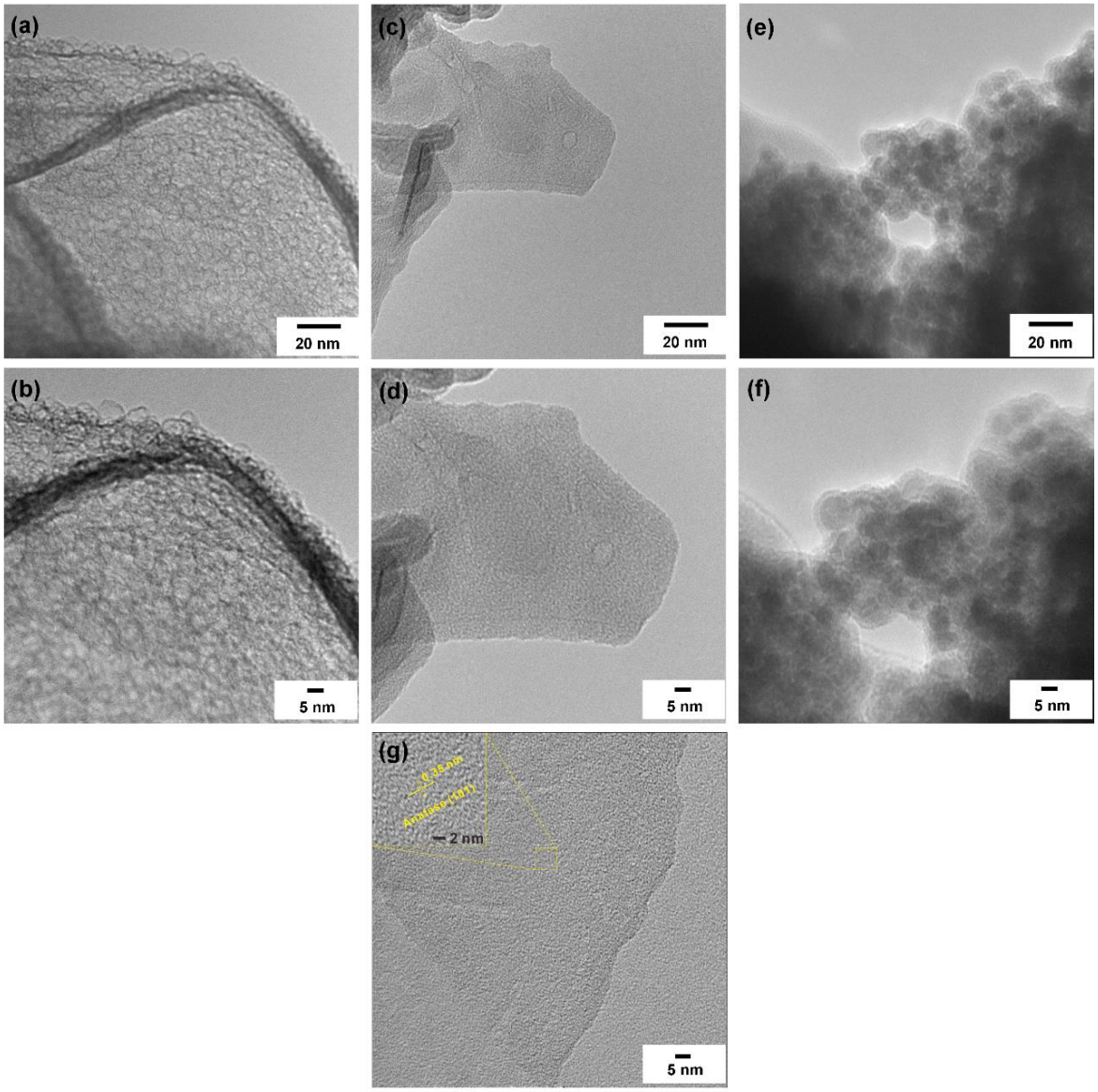

Figure 2.5. TEM images of TiO_2/graphene nanocomposites: a,b) TG-H_2O/9BA, c,d) TG-NH_3/3BA, and e,f) TiO_2/rGO. g) A HR-TEM image of TG-NH_3/3BA.

UV-Vis DRS spectra were used to study optical properties of the TiO_2/graphene nanocomposites. According to Figure 2.6a, an increase in the background absorption in the visible-light region was observed in the case of the nanocomposites due to the incorporation of graphene into the matrix of TiO_2 [86]. The graphene content in the TG-NH_3/3BA and TiO_2/rGO nanocomposites was respectively estimated as 0.065 and 0.115 wt% based on a calibration curve using physical mixtures of GNP and TiO_2-TKP 101 powder (Figure 2.7).

The absorption edge of the TiO_2/rGO sample (396 nm) was found to be comparable with that of TiO_2-P25 (390 nm). On the other hand, a remarkable extension of the absorption edge to 578 nm was obtained for the TG-NH_3/3BA sample. Note that the absorption edge of nano-sized TiO_2 in the anatase form is at 360 nm [87].

Based on the Tauc plot, the band gap was acquired by extrapolating a linear part of $(h\upsilon F(R_\infty))^{1/2}$ to the *x* axis [88–90] (Figure 2.6b, Table 2.2). A small reduction in the band gap energy of the TiO_2/rGO sample (3.25 eV) with respect to that of TiO_2-P25 (3.35 eV) was simply brought by the background absorption from graphene. In the case of TG-NH_3/3BA, the first band gap energy was located at 3.54 eV and the second one was at 2.33 eV. The increase in the first band gap as well as the blue-shift of the absorption edge of TG-NH_3/3BA nanocomposite can be explained due to the nano-sized of TiO_2. It has been reported that the band gap of semiconductor crystalline is a function of the particle size [91–93]. Below a certain threshold, the defects density of semiconductor crystalline increases with the decrease in particle size. Owing to the delocalization of molecular orbitals on the semiconductor surface, these defects can generate deep or shallow traps near the band edge of its electronic state, leading to the reduction of band gap or the red-shift in absorption spectrum [91,92]. On the other hand, when the particle size of semiconductor decreases from its bulk to that of Bohr radius, the size-quantization effect appears because of the charge carrier spatial confinement. As a consequence, electrons and holes in the quantum sized semiconductor are limited in a potential well and enable to undergo the delocalization occurring in the bulk. Thus, the band gap of the ultra-fine semiconductor increases with the decrease in the particle size when it smaller than the band gap minimum [91,92]. This phenomenon has been well examined and confirmed [94–96].

Table 2.2. The band gap energies of TiO_2-P25, TiO_2/rGO, and TiO_2/graphene nanocomposite.

Sample	Band gap[a] (eV)
TiO_2-P25	3.35
TiO_2/rGO	3.25
TG-NH_3/3BA	3.54, 2.33

[a] Derived from UV-Vis DRS spectra based on the Tauc plot (*cf.* Figure 2.6b).

In order to address the origin of this extraordinary extension, the UV-Vis DRS spectra of TiO_2/graphene nanocomposites synthesized using different catalysts were investigated (Figures 2.6c). First, the extension of the absorption edge was obtained only when the nanocomposites were prepared in the presence of benzylamine, in which residual benzylamine was always present (Figure 2.4a). Second, in spite of the significance of benzylamine in the extension of the absorption edge, the amount of benzylamine negligibly influenced this edge extension (Figure 2.6d). To the increase of the benzylamine amount by changing the ratio of NH_3 to benzylamine or the decrease of the benzylamine amount by additional washing, the change in the absorption edge extension of the resultant nanocomposites was trivial. Third, when benzylamine was added to TiO_2-P25 and the TiO_2/rGO nanocomposite, similar edge extension was hardly obtained (Figure 2.8). Finally, the calcination of the TiO_2/graphene nanocomposites at 400 °C for 24 h under dry air completely removed the residual benzylamine and it accompanied the disappearance of the second absorption edge (Figure 2.9). Till this point, I can conclude that a trace amount of benzylamine was firmly immobilized in the course of the synthesis through the formation of a charge-transfer complex, which significantly extended the absorption edge.

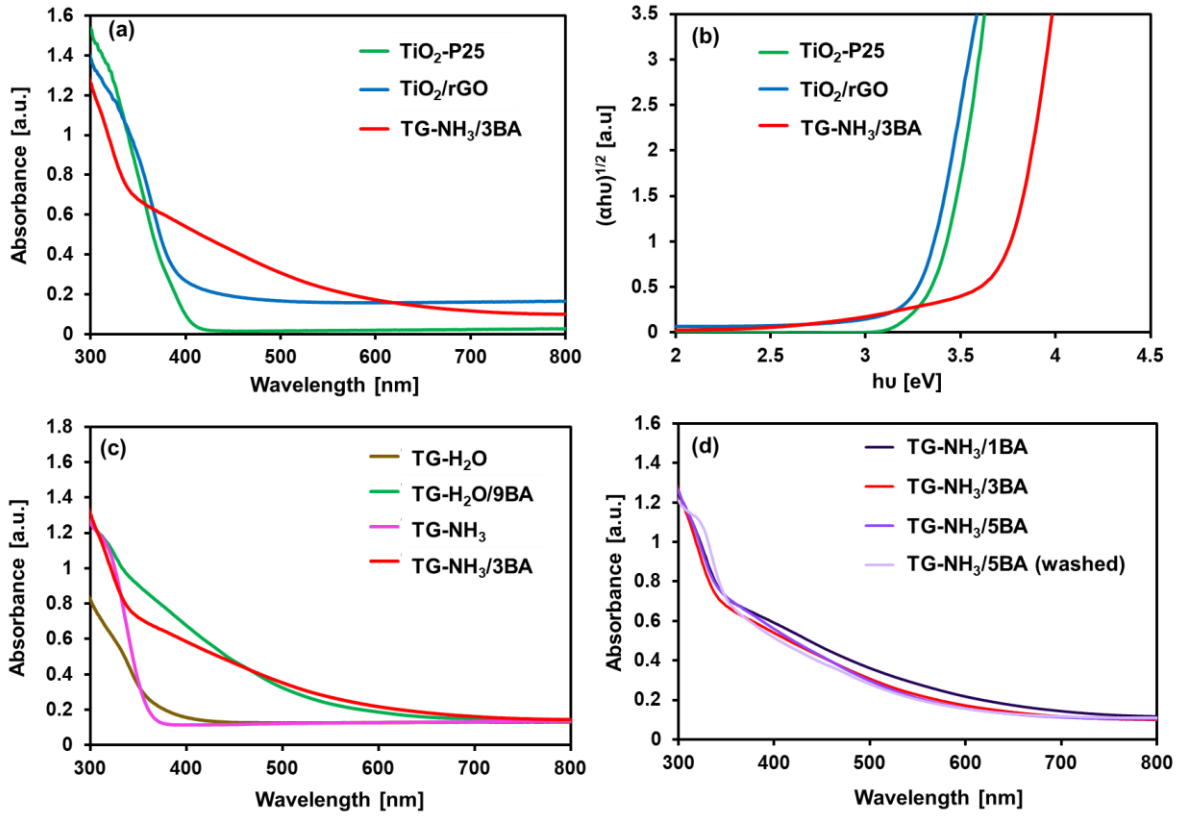

Figure 2.6. a) UV-Vis DRS spectra of TiO_2-P25, TiO_2/rGO, and TiO_2/graphene nanocomposites, b) Tauc plot, c) effect of the catalysts, and d) effect of the benzylamine amount on the absorption edge extension.

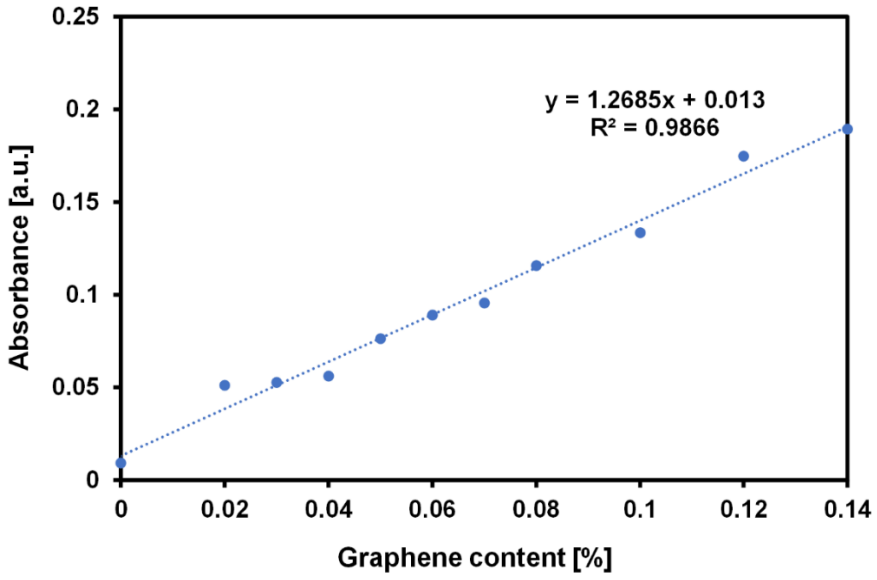

Figure 2.7. The calibration curve for the graphene content. The calibration curve was built using mixtures of GNP and TiO_2-TKP 101. The absorbance values at the wavelength of 750 nm in the UV-Vis DRS spectra were plotted against the graphene content.

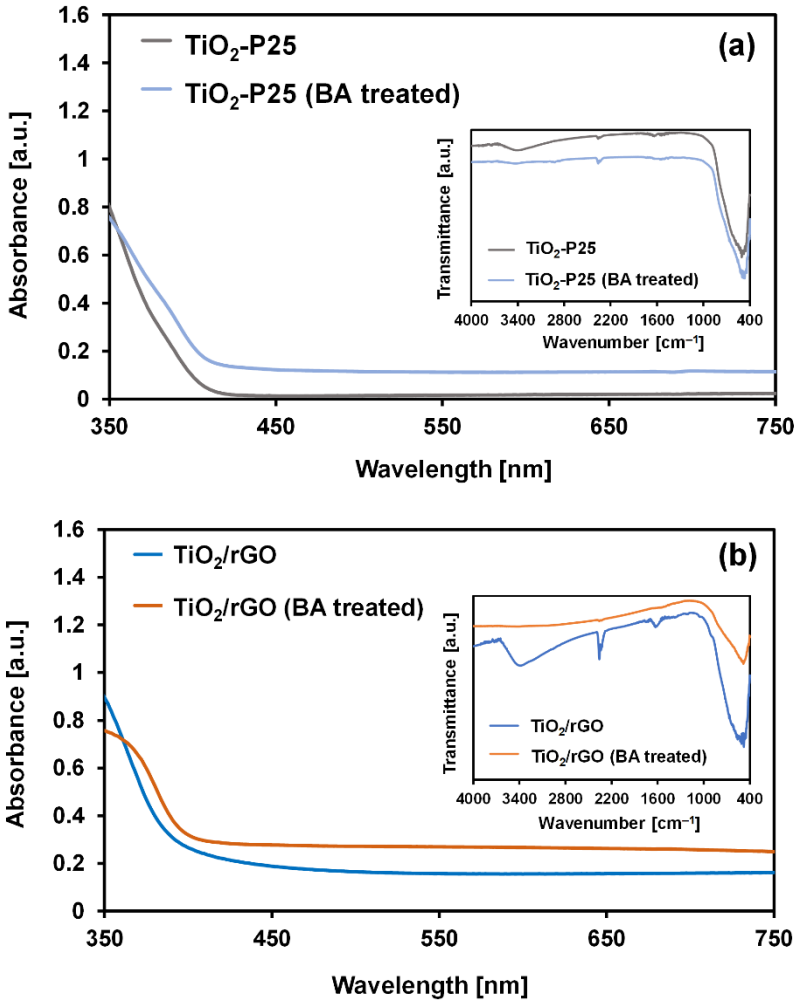

Figure 2.8. UV-Vis DRS spectra of TiO_2-P25 and the TiO_2/rGO nanocomposite before and after adding benzylamine. A treatment of TiO_2-P25 and TiO_2/rGO samples with benzylamine hardly extended the absorption edge in the UV-Vis DRS spectra. It is also noted that the complexation of benzylamine was not observed in the IR spectra (insets) for these samples.

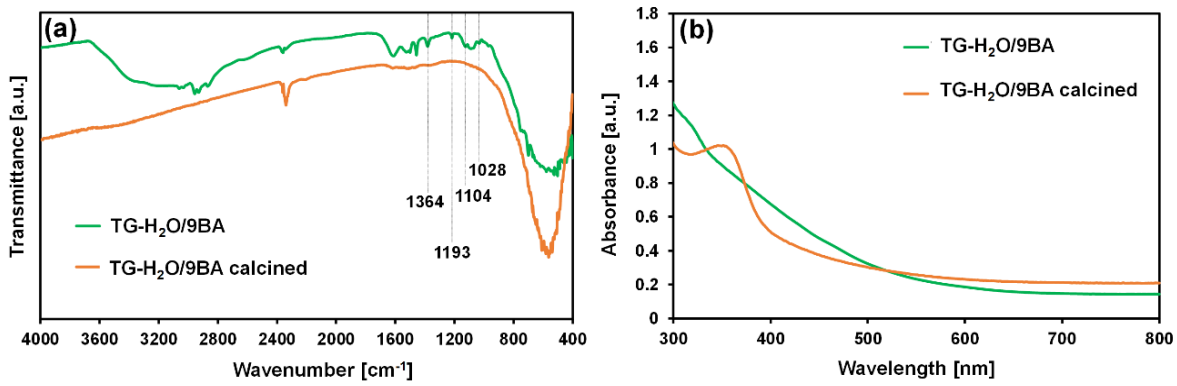

Figure 2.9. a) FTIR and b) UV-Vis DRS spectra of TG-H_2O/9BA before and after calcination at 400 °C for 24 h under dry air.

It is well-known that the PL emission spectrum is a powerful tool to study the efficiency of the charge carrier trapping, immigration, transfer, and separation in semiconductors since the photon emission arises from the recombination of the photoexcited electrons and holes. Therefore, a lower PL intensity is related to a lower recombination rate of the electrons and holes, suggesting higher separation efficiency under light irradiation. Figure 2.10 displays the PL spectra of TiO_2-P25 and TiO_2/graphene nanocomposites. The PL spectra of all the samples showed the emission peaks at 398, 420, 450, 468, 482, and 493 nm. The peak at 398 nm corresponds to the band gap energy of TiO_2 [97]. The peak at 420 nm was attributed to the radiative recombination process related to hydroxylated Ti^{3+} surface complexes [98] that are formed by the charge transfer excitation of TiO_2. The four peaks observed in the range of 450–493 nm resulted from excitonic PL of non-stoichiometric TiO_2 and surface oxygen vacancies of TiO_2. The peaks at 450 nm and 468 nm were likely attributed to band-edge free excitons, and the peaks at 483 nm and 493 nm were from bound excitons [99]. It was observed that the PL intensity of the TiO_2/rGO and TiO_2/graphene nanocomposites was significantly decreased compared to that of TiO_2-P25. This indicates that the recombination of electron-hole pairs in TiO_2 was suppressed by

being paired with graphene. In addition, the nanocomposites prepared from the graphene dispersion (TG-H_2O/9BA and TG-NH_3/3BA) presented the lowest PL intensities, which proved the excellence of the created morphology in suppressing the electron-hole recombination.

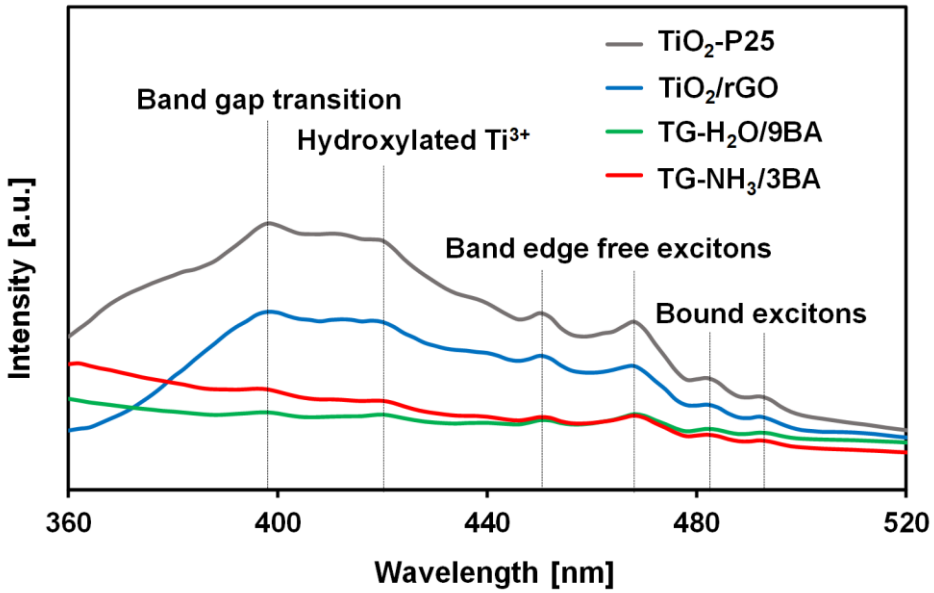

Figure 2.10. PL spectra of TiO_2-P25, TiO_2/rGO, and TiO_2/graphene nanocomposites. The excitation source of 300 nm was employed.

The specific charge carrier dynamics of TiO_2-P25 and the TiO_2/graphene nanocomposite was probed by the time-resolved PL spectroscopy (Figure 2.11). The emission decay curves of the two samples were fitted by biexponential kinetic function. The two decay components were derived (insert in Figure 2.11), where τ_1, fast decay component is caused by the nonradiative recombination of the surface trapped electron-hole pair; τ_2, slow decay component arises from the recombination of free excitons in the TiO_2 [100]. The average emission lifetime, which presents the overall emission decay behavior of the sample is calculated using Equation 2.2 [101].

$$\langle \tau \rangle = \sum_{i=1}^{n} \frac{A_i \tau_i^2}{A_i \tau_i} \tag{2.2}$$

In the case of TG-NH_3/3BA nanocomposite, the emission lifetime of both components is shorter than that of TiO_2-P25. The average emission lifetime of TG-NH_3/3BA nanocomposite (3.90 ns) also shows a significant decrease compared to that of TiO_2-P25 (8.70 ns). Lifetime reduction accompanying with the obvious PL quenching (Figure 2.10) indicated the formation of electron transfer channel from TiO_2 to graphene in a nonradiative quenching pathway [102].

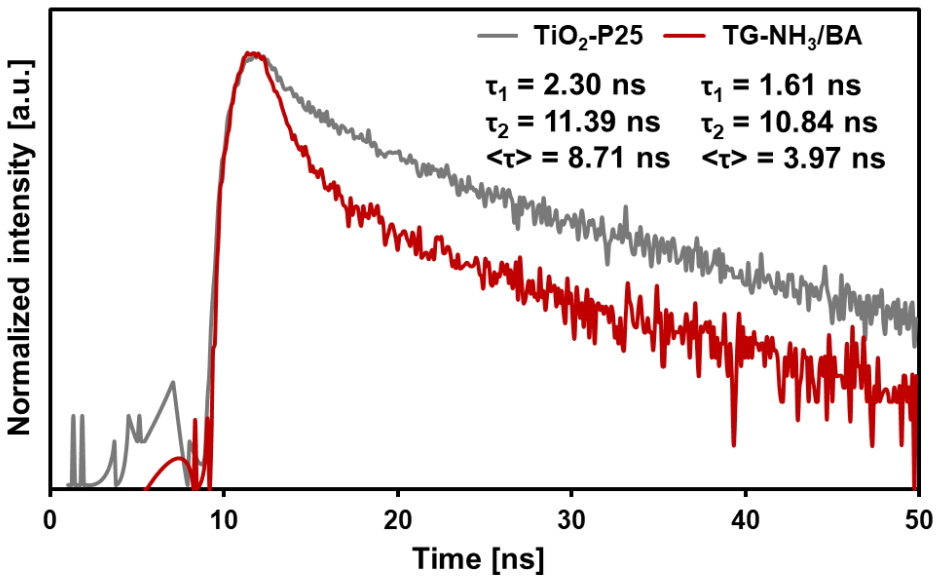

Figure 2.11. Time-resolved transient PL decay of TiO_2-P25 and TiO_2/graphene nanocomposite

2.3.2. Photocatalytic test

The photocatalytic activity of TiO_2-P25, TiO_2/rGO, and the TiO_2/graphene nanocomposites was evaluated based on the photodegradation of MB under visible light. First, the adsorption ability of the catalysts was evaluated by the adsorption of MB in dark

for 12 h, which was sufficiently long for reaching the adsorption/desorption equilibrium. Figure 2.11a compares the MB adsorption ability of the catalysts. It can be seen that the presence of graphene more or less enhanced the adsorption ability of the nanocomposites compared to that of TiO_2-P25, which could be attributed to both/either enhanced surface area and/or enhanced affinity of the catalysts towards conjugated molecules. It is well-known that, in aqueous phase, the adsorption of methylene blue on the photocatalyst contains three main steps: i) transport of the methylene blue from the bulk solution to the outer surface of the photocatalyst (film diffusion); ii) internal diffusion of the methylene blue molecules from the outer surface to the inner surface of the photocatalyst; and iii) adsorption of the methylene blue molecules on the external surface of the photocatalyst through binding of the adsorbate to the active sites [103–105]. With ideal sheet-like structure and the benefit of high surface area, the TiO_2/graphene nanocomposites prepared in the presence of benzylamine exhibited far the highest adsorption capacity. Moreover, with a uniform nanosized TiO_2 layer, it is possible for methylene blue molecules to diffuse deeper through TiO_2 layer and undergo the chemisorption with graphene based on the π–π stacking between the aromatic rings in MB molecules and the aromatic domains of graphene [106].

In order to normalize the significant difference in the MB adsorption capacity, the amount of the catalysts was adjusted to unify the initial concentration of MB before irradiation (after 12 h in dark). After the equilibration in dark, visible light was irradiated under constant stirring and the MB concentration in the supernatant was tracked along the irradiation time (inset of Figure 2.11b). Then, the activity of the three catalysts was quantified by the MB decomposition per gram-catalyst per hour (Figure 2.11b). The MB degradation rate was found to be greater in the order of TiO_2-P25 < TiO_2/rGO << TG-H_2O/9BA < TG-NH_3/3BA. The TiO_2/graphene nanocomposites that were prepared from the

graphene dispersion in the co-presence of NH_3 and benzylamine exhibited far the highest photocatalytic activity (0.201 mmol g_{cat}^{-1} h^{-1}), which was 5 times higher than that of the conventional TiO_2/rGO nanocomposite (0.041 mmol g_{cat}^{-1} h^{-1}) and 15 times higher than that of TiO_2-P25 (0.013 mmol g_{cat}^{-1} h^{-1}). Note that the self-decomposition of MB was negligible in the absence of the catalysts (Figure 2.12).

In understanding the origin of the highest photocatalytic activity of the TiO_2/graphene nanocomposites, three potential factors were identified in the characterization parts:

i) A special morphology, *i.e.* graphene sheets uniformly covered by a TiO_2 nano layer, led to far the greatest adsorption capacity of the nanocomposites.

ii) A significant extension of the absorption edge enhanced the utilization efficiency of the visible light.

iii) The thin TiO_2 layer covering graphene sheets as well as a low defect density of graphene promoted the most effective separation of charge carriers.

These three factors were necessarily accompanied as long as the nanocomposites were prepared from the graphene dispersion in the presence of benzylamine, so that it might be difficult to isolatedly discuss the impact of respective factors. Nonetheless, if one compares the catalyst activity based on the adsorption amount of MB rather than the gram catalyst, the factor i) could be distinguished from the other two factors (Figure 2.11c). For instance, the activity of TG-NH_3/BA was 5.0 times higher than that of TiO_2/rGO on the basis per gram catalyst, while it became 1.4 times per MB adsorption. This fact indicates that a large portion of the activity enhancement (*ca.* 70%) was attributed to the factor i). On the other hand, the 1.4 times enhancement in the activity per MB adsorption dictates non-negligible contributions of the factors ii, iii). Thus, I conclude that the highest activity of the developed TiO_2/graphene nanocomposites benefitted from the combination of all the advantages that were brought by the direct conversion of the graphene dispersion in Ti(O*n*Bu)$_4$.

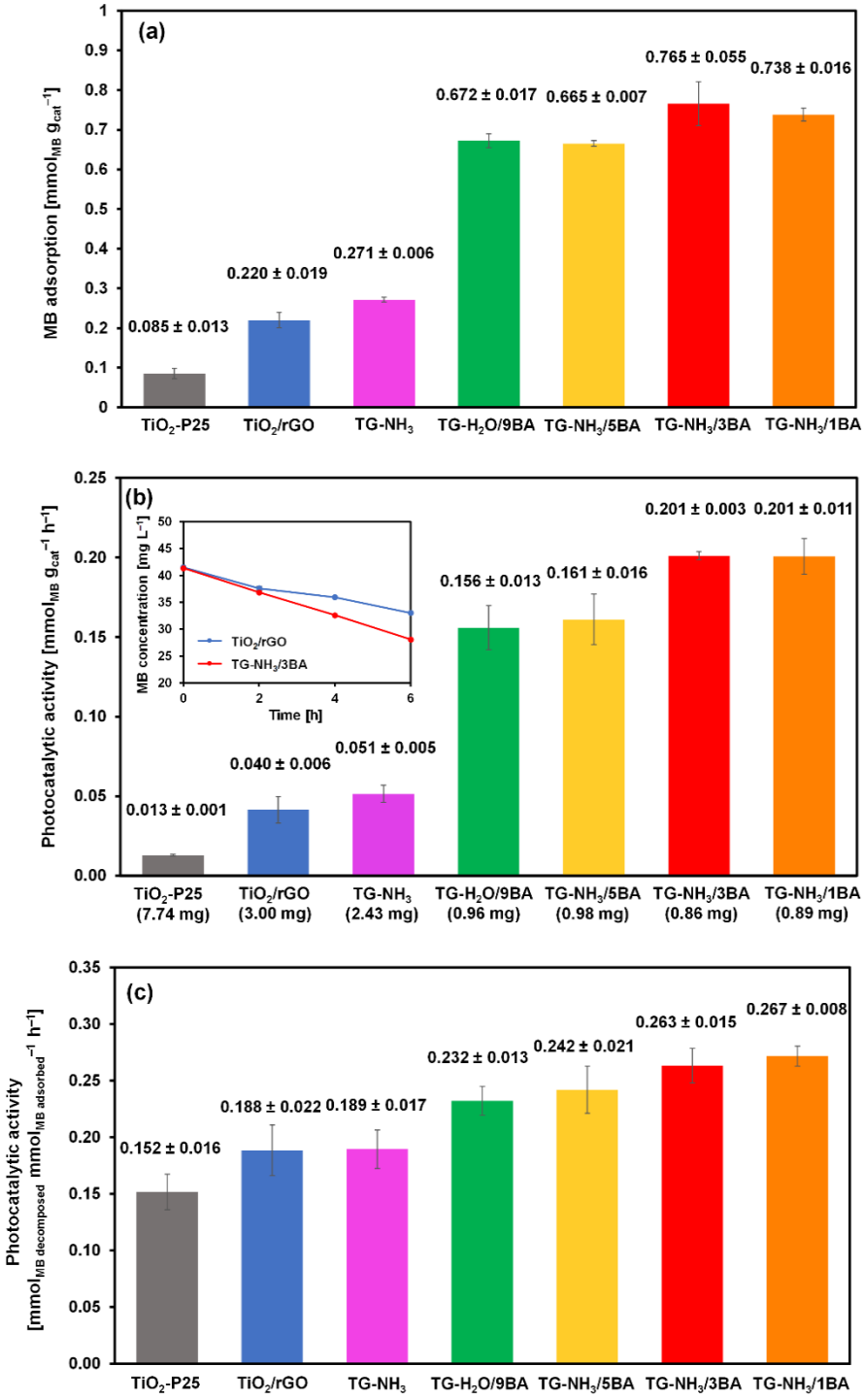

Figure 2.11. a) Equilibrium adsorption of MB on TiO_2-P25, TiO_2/rGO, and TiO_2/graphene nanocomposites. 3.0 mg of a sample was placed in 50 mg/mL aqueous solution of MB in dark for 12 h under constant stirring. The amount of the adsorption was derived by measuring the MB concentration in the supernatant after 12 h. b) Photocatalytic activity per

gram catalyst. The activity was evaluated from the loss of the MB concentration after 6 h irradiation. The grams in the parentheses correspond to the amount of the catalysts employed in the photocatalytic test in order to unify the initial concentration of MB in the supernatant (after 12 h in dark and before the irradiation). c) Photocatalytic activity per MB adsorption. The activity per gram catalyst in b) was normalized by the MB adsorption capacity per gram catalyst in a).

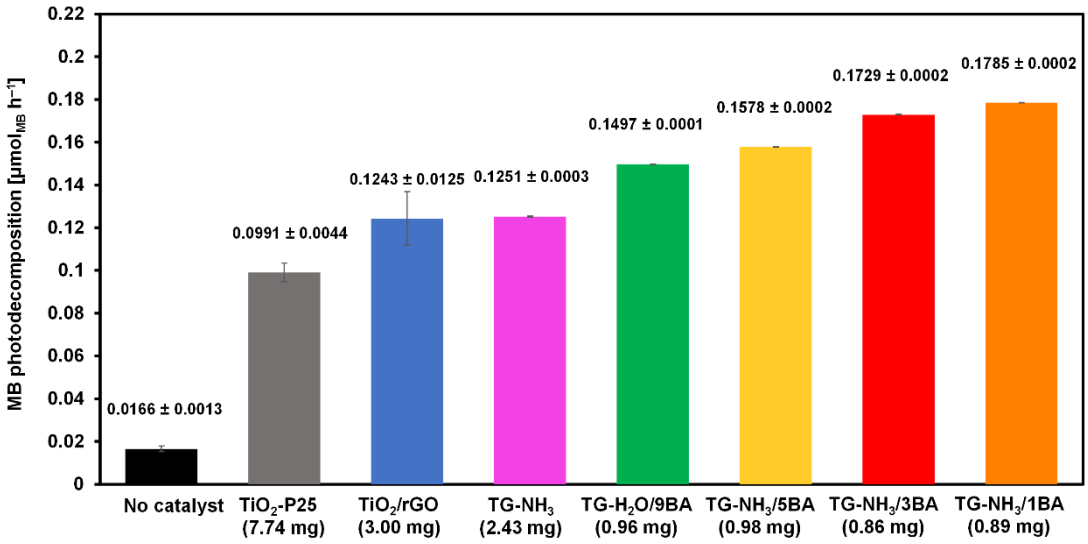

Figure 2.12. Photodecomposition of methylene blue.

2.3.3. Identification of active species

Figure 2.13 shows the impact of the addition of different scavengers on the activity of nanocomposites. The impact was quantified in terms of the MB decomposition rate with respect to that in the absence of any scavengers. It can be seen that the addition of ammonium oxalate, a hole scavenger, exhibited the largest impact on the activity for both catalysts, indicating the importance of holes in the photocatalytic degradation of MB. However, the impact was most pronouncedly observed for the TiO_2/graphene nanocomposite. The addition of tert-butyl alcohol, a scavenger for hydroxyl radicals,

reduced the activity of TiO_2/rGO when compared to that of the TiO_2/graphene nanocomposite. Last, the addition of benzoquinone, a superoxide radical scavenger, marginally influenced the photocatalytic performance of TiO_2/rGO nanocomposite. Contrary, the activity of the TiO_2/graphene nanocomposite was largely inhibited by the existence of benzoquinone.

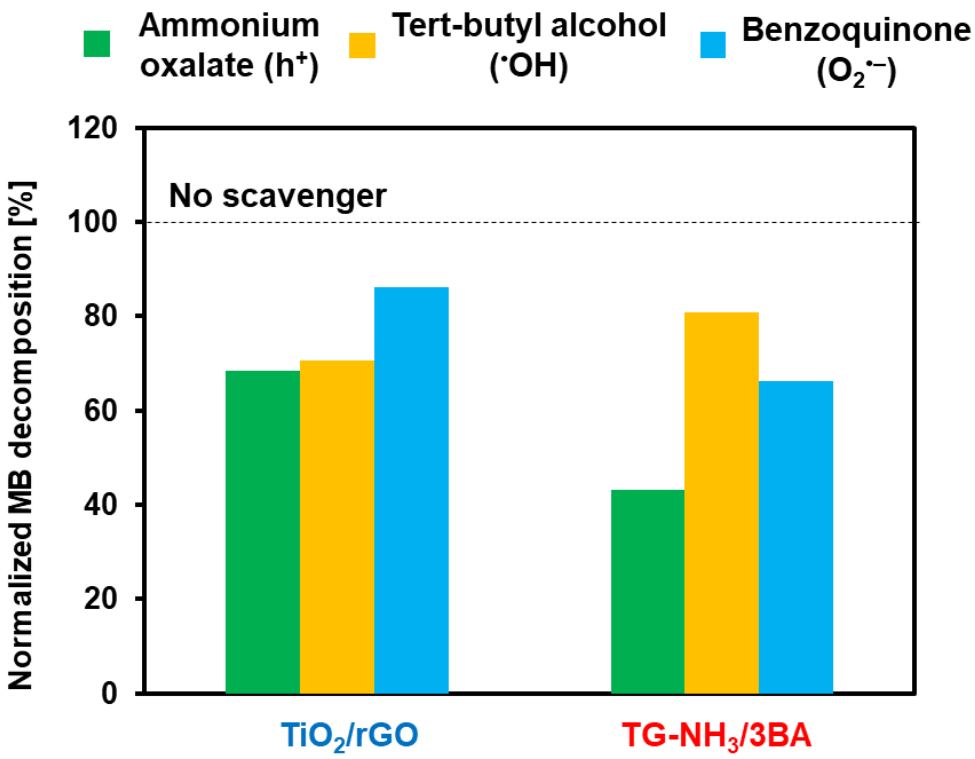

Figure 2.13. Effect of radical scavengers on the photocatalytic efficiency of TiO_2/rGO, and the TiO_2/graphene nanocomposite. The activity in the MB photodecomposition was compared in the presence and absence of a scavenger for individual catalysts.

In general, different types of active species can be generated during the photocatalytic process, such as electrons, holes, hydroxyl radicals, and, superoxide radicals [107–109]. The roles of these active species in the photodegradation reactions are different. Photo-excited

electrons can reduce the oxygen molecules adsorbed on the catalyst surface to produce superoxide radicals ($O_{2\ ads} + e^- \rightarrow O_2^{\bullet -}$) and/or can be directly involved in the reduction of various ionic pollutants [110]. Photo-induced holes can contribute to the formation of hydroxyl radicals ($HO^- + h^+ \rightarrow HO^\bullet$) and/or can be directly involved to oxidize organic pollutants ($R^\bullet + h^+ \rightarrow R^{\bullet +} \rightarrow$ intermediate(s)/final degradation products). Subsequently, the generated hydroxyl and superoxide radicals directly participate in the degradation of organic pollutants [111,112]. Thus, in my photocatalyst systems for the MB photodegradation, holes, hydroxyl, and superoxide radicals were considered as potential active species. In the case of TiO_2/rGO, holes and hydroxyl radicals were mainly involved in the photocatalytic reaction while for the TiO_2/graphene nanocomposite, holes and superoxide radicals played key roles for the photodegradation reaction. Whereas, hydroxyl radicals seemed not to be the major oxidation species in the TiO_2/graphene nanocomposite. Firstly, the sheet-like morphology of the TiO_2/graphene nanocomposite was advantageous in suppressing the electron-hole recombination. The large amount of photo-excited electrons subsequently reduced the adsorbed oxygen molecules to form superoxide radicals. Additionally, the ideal morphology of the TiO_2/graphene nanocomposite led to its excellent ability to adsorb organic pollutants (MB in this case). It was expected that MB molecules strongly adsorb on the surface of the TiO_2/graphene, and this facilitates the direct decomposition of MB by photo-induced holes (in turn decreases a chance for holes to generate hydroxyl radicals).

2.4. Conclusion

In this chapter, a new synthetic route for the preparation of TiO_2/graphene nanocomposites was developed, which was based on the chemical exfoliation of graphite in titanium alkoxide with the aid of ultrasonication, and subsequent sol-gel reaction in the

presence of a specific catalyst, *i.e.* benzylamine. It was found that the titanium alkoxide afforded the graphene dispersion of a high quality in terms of a trace amount of defects and a few layers of dispersed graphene. Moreover, the sol-gel reaction from this dispersion led to TiO_2/graphene nanocomposites featured with promising characteristics for visible-light photocatalysts: A special morphology composed by graphene sheets uniformly and thinly covered by a TiO_2 nano layer, a significant extension of the absorption edge to the visible-light region, and suppression of charge carrier recombination. These advantages were successfully demonstrated in the photocatalytic decomposition of methylene blue under visible-light irradiation. The TiO_2/graphene nanocomposites exhibited 15 and 5 times higher activity than TiO_2-P25 and a conventional TiO_2/reduced graphene oxide nanocomposite. Investigation of active species clarified the significance of holes and superoxide radicals in the photodegradation reaction using the TiO_2/graphene nanocomposites.

2.5. References

[1] Hamad, S., Catlow, C. R. A., Woodley, S. M., Lago, S., Mejias, J. A. Structure and stability of small TiO_2 nanoparticles. J. Phys. Chem. B 2005; 109(33):15741–8.

[2] Varghese, O. K., Paulose, M., LaTempa, T. J., Grimes, C. A. High-rate solar photocatalytic conversion of CO_2 and water vapor to hydrocarbon fuels. Nano Lett. 2009; 9(2):731–7.

[3] Adachi, M., Murata, Y., Takao, J., Jiu, J., Sakamoto, M., Wang, F. Highly efficient dye-sensitized solar cells with a titania thin-film electrode composed of a network structure of single-crystal-like TiO_2 nanowires made by the “oriented attachment” mechanism. J. Am. Chem. Soc. 2004; 126(45):14943−9.

[4] Zakrzewska, K. Mixed oxides as gas sensors. Thin Solid Films 2001; 391(2):229–38.

[5] Kalyanasundaram, K., Grätzel, M. Applications of functionalized transition metal complexes in photonic and optoelectronic devices. Coord. Chem. Rev. 1998; 177(1):347−414.

[6] Huber, R., Moser, J. E., Grätzel, M., Wachtveitl, J. Real-time observation of photoinduced adiabatic electron transfer in strongly coupled dye/semiconductor colloidal systems with a 6 fs time constant. J. Phys. Chem. B 2002; 106(25):6494−9.

[7] Anpo, M. Use of visible-light. Second-generation titanium oxide photocatalysts prepared by the application of an advanced metal ion-implantation method. Pure Appl. Chem. 2000; 72(9):1787–92.

[8] Hu, C., Lan, Y., Qu, J., Hu, X., Wang, A. Ag/AgBr/TiO_2 visible-light photocatalyst for destruction of azodyes and bacteria. J. Phys. Chem. B 2006; 110(9):4066–72.

[9] Khairy, M., Zakaria, W. Effect of metal-doping of TiO_2 nanoparticles on their photocatalytic activities toward removal of organic dyes. Egypt. J. Pet. 2014; 23(4):419–26.

[10] Zhu, J., Zheng, W., He, B., Zhang, J., Anpo, M. Characterization of Fe-TiO_2 photocatalysts synthesized by hydrothermal method and their photocatalytic reactivity for photodegradation of XRG dye diluted in water. J. Mol. Catal. A: Chem. 2004; 216(1):35–43.

[11] Chen, D., Jiang, Z., Geng, J., Wang, Q., Yang, D. Carbon and nitrogen co-doped TiO_2 with enhanced visible-light photocatalytic activity. Ind. Eng. Chem. Res. 2007; 46(9):2741−6.

[12] Dong, F., Guo, S., Wang, H., Li, X., Wu, Z. Enhancement of the visible-light photocatalytic activity of C-doped TiO_2 nanomaterials prepared by a green synthetic approach. J. Phys. Chem. C 2011; 115(27):13285−92.

[13] Gao, C., Li, J., Shan, Z., Huang, F., Shen, H. Preparation and visible-light photocatalytic activity of In_2S_3/TiO_2 composite. Mater. Chem. Phys. 2010; 122(1):183−7.

[14] Bessekhouad, Y., Robert, D., Weber, J. V. Bi_2S_3/TiO_2 and CdS/TiO_2 heterojunctions as an available configuration for photocatalytic degradation of organic pollutant. J. Photochem. Photobiol. A: Chem. 2004; 163(3):569–80.

[15] Kim, S., Hwang, S. J., Choi, W. Visible-light active platinum-ion-doped TiO_2 photocatalyst. J. Phys. Chem. B 2005; 109(51):24260–7.

[16] Sobana, N., Muruganadham, M., Swaminathan, M. Nano-Ag particles doped TiO_2 for efficient photodegradation of direct azo dyes. J. Mol. Catal. A: Chem. 2006; 258(1):124–32.

[17] Chen, B., Meng, Y., Sha, J., Zhong, C., Hu, W., Zhao, N. Preparation of MoS_2/TiO_2 based nanocomposites for photocatalysis and rechargeable batteries: Progress, challenges, and perspective. Nanoscale 2018; 10(1):34–68.

[18] Cozzoli, P. D., Kornowski, A., Weller, H. Low-temperature synthesis of soluble and processable organic-capped anatase TiO_2 nanorods. J. Am. Chem. Soc. 2003; 125(47):14539−48.

[19] Niederberger, M., Garnweitner, G., Krumeich, F., Nesper, R., Cölfen, H., Antonietti, M. Tailoring the surface and solubility properties of nanocrystalline titania by a nonaqueous *in situ* functionalization process. Chem. Mater. 2004; 16(7):1202−8.

[20] Li, X., Wang, D., Cheng, G., Luo, Q., An, J., Wang, Y. Preparation of polyaniline-modified TiO_2 nanoparticles and their photocatalytic activity under visible-light illumination. Appl. Catal. B: Environ. 2008; 81(3):267−73.

[21] Zhao, J., Chen, C., Ma, W. Photocatalytic degradation of organic pollutants under visible-light irradiation. Top. Catal. 2005; 35(3):269–78.

[22] Le, L. H., Trinh, D. X., Trung, N. B., Tran, T. P. N., Taniike, T. Fabrication of assembled membrane from malonate-functionalized graphene and evaluation of its permeation performance. Carbon 2017; 114:519–25.

[23] Tran, T. P. N., Thakur, A., Trinh, D. X., Dao, A. T. N., Taniike, T. Design of Pd@Graphene oxide framework nanocatalyst with improved activity and recyclability in Suzuki-Miyaura cross-coupling reaction. Appl. Catal. A: Gen. 2018; 549:60–7.

[24] Lui, G., Liao, J. Y., Duan, A., Zhang, Z., Fowler, M., Yu, A. Graphene-wrapped hierarchical TiO_2 nanoflower composites with enhanced photocatalytic performance. J. Mater. Chem. 2013; 1(39):12255–62.

[25] Zhou, K., Zhu, Y., Yang, X., Jiang, X., Li, C. Preparation of graphene-TiO_2 composites with enhanced photocatalytic activity. New J. Chem. 2011; 35(2):353–9.

[26] Eigler, S., Grimm, S., Enzelberger-Heim, M., Müller, P., Hirsch, A. Graphene oxide: Efficiency of reducing agents. Chem. Commun. 2013; 49(67):7391–3.

[27] Lambert, T. N., Chavez, C. A., Hernandez-Sanchez, B., Lu, P., Bell, N. S., Ambrosini, A., *et al*. Synthesis and characterization of titania-graphene nanocomposites. J. Phys. Chem. C 2009; 113(46):19812–23.

[28] Zhang, H., Lv, X., Li, Y., Wang, Y., Li, J. P25-graphene composite as a high performance photocatalyst. ACS Nano 2009; 4(1):380–6.

[29] Dreyer, D. R., Murali, S., Zhu, Y., Ruoff, R. S., Bielawski, C. W. Reduction of graphite oxide using alcohols. J. Mater. Chem. 2011; 21(10):3443–7.

[30] Han, Y., Wang, T., Gao, X., Li, T., Zhang, Q. Preparation of thermally reduced graphene oxide and the influence of its reduction temperature on the thermal, mechanical, flame retardant performances of PS nanocomposites. Compos. Part A: Appl. Sci. Manuf. 2016; 84:336–43.

[31] Zhang, Y., Pan, C. TiO_2/graphene composite from thermal reaction of graphene oxide and its photocatalytic activity in visible light. J. Mater. Sci. 2011; 46(8):2622–6.

[32] Dubin, S., Gilje, S., Wang, K., Tung, V. C., Cha, K., Hall, A. S., *et al*. A one-step, solvothermal reduction method for producing reduced graphene oxide dispersions in organic solvents. ACS Nano 2010; 4(7):3845–52.

[33] Chen, W., Yan, L., Bangal, P. R. Preparation of graphene by the rapid and mild thermal reduction of graphene oxide induced by microwaves. Carbon 2010; 48(4):1146–52.

[34] Hou, W. C., Chowdhury, I., Goodwin Jr, D. G., Henderson, W. M., Fairbrother, D. H., Bouchard, D., *et al*. Photochemical transformation of graphene oxide in sunlight. Environ. Sci. Technol. 2015; 49(6):3435–43.

[35] Wu, T., Liu, S., Li, H., Wang, L., Sun, X. Production of reduced graphene oxide by UV irradiation. J. Nanosci. Nanotechnol. 2011; 11(11):10078–81.

[36] Liu, X., Pan, L., Lv, T., Zhu, G., Lu, T., Sun, Z., *et al*. Microwave-assisted synthesis of TiO_2-reduced graphene oxide composites for the photocatalytic reduction of Cr(VI). RSC Adv. 2011; 1(7):1245–9.

[37] Xu, T., Zhang, L., Cheng, H., Zhu, Y. Significantly enhanced photocatalytic performance of ZnO via graphene hybridization and the mechanism study. Appl. Catal. B: Environ. 2011; 101(3):382–7.

[38] Larciprete, R., Fabris, S., Sun, T., Lacovig, P., Baraldi, A., Lizzit, S. Dual path mechanism in the thermal reduction of graphene oxide. J. Am. Chem. Soc. 2011; 133(43):17315–21.

[39] Sellappan, R., Sun, J., Galeckas, A., Lindvall, N., Yurgens, A., Kuznetsov, *et al*. Influence of graphene synthesizing techniques on the photocatalytic performance of graphene-TiO_2 nanocomposites. Phys. Chem. Chem. Phys. 2013; 15(37):15528–37.

[40] Jiang, G., Lin, Z., Chen, C., Zhu, L., Chang, Q., Wang, N., *et al.* TiO_2 nanoparticles assembled on graphene oxide nanosheets with high photocatalytic activity for removal of pollutants. Carbon 2011; 49(8):2693–701.

[41] Liang, Y. T., Vijayan, B. K., Gray, K. A., Hersam, M. C. Minimizing graphene defects enhances titania nanocomposite-based photocatalytic reduction of CO_2 for improved solar fuel production. Nano Lett. 2011; 11(7):2865–70.

[42] Ding, H., Zhang, S., Juan, P. C., Liu, T. Y., Du, Z. F., Zhao, D. L. Enhancing the photovoltaic performance of dye-sensitized solar cells by modifying TiO_2 photoanodes with exfoliated graphene sheets. RSC Adv. 2016; 6(47):41092–102.

[43] Zhang, Y., Zhang, N., Tang, Z. R., Xu, Y. J. Improving the photocatalytic performance of graphene-TiO_2 nanocomposites via a combined strategy of decreasing defects of graphene and increasing interfacial contact. Phys. Chem. Chem. Phys. 2012; 14(25):9167–75.

[44] Yang, M. Q., Xu, Y. J. Selective photoredox using graphene-based composite photocatalysts. Phys. Chem. Chem. Phys. 2013; 15(44):19102–18.

[45] Hummers Jr, W. S., Offeman, R. E. Preparation of graphitic oxide. J. Am. Chem. Soc. 1958; 80(6):1339.

[46] Taniike, T. JP Patent 229619, 2015.

[47] Cai, M., Thorpe, D., Adamson, H., Schniepp, H. C. Methods of graphite exfoliation. J. Mater. Chem. 2012; 22(48):24992–5002.

[48] Narayan, R., Kim, S. O. Surfactant mediated liquid phase exfoliation of graphene. Nano Converg. 2015; 2(1):20.

[49] Jiang, B., Tian, C., Pan, Q., Jiang, Z., Wang, J. Q., Yan, W., *et al*. Enhanced photocatalytic activity and electron transfer mechanisms of graphene/TiO_2 with exposed {001} facets. J. Phys. Chem. C 2011; 115(48):23718–25.

[50] Xiang, Q., Yu, J., Jaroniec, M. Enhanced photocatalytic H_2-production activity of graphene-modified titania nanosheets. Nanoscale 2011; 3(9):3670–8.

[51] Yang, D., Velamakanni, A., Bozoklu, G., Park, S., Stoller, M., Piner, R. D, *et al.* Chemical analysis of graphene oxide films after heat and chemical treatments by X-ray photoelectron and Micro-Raman spectroscopy. Carbon 2009; 47(1):145–52.

[52] Ohsaka, T., Izumi, F., Fujiki Y. Raman spectrum of anatase. J. Raman Spectrosc. 1978; 7(6):321−4.

[53] Pimenta, M. A., Dresselhaus, G., Dresselhaus, M. S., Cancado, L. G., Jorio, A., Saito, R. Studying disorder in graphite-based systems by Raman spectroscopy. Phys. Chem. Chem. Phys. 2007; 9(11):1276–90.

[54] Zhang, W., Cui, J., Tao, C. A., Wu, Y., Li, Z., Ma, L., *et al*. A strategy for producing pure single-layer graphene sheets based on a confined self-assembly approach. Angew. Chem. Int. Ed. 2009; 121(32):5978−82.

[55] Zhang, Y., Zhang, N., Tang, Z. R., Xu, Y. J. Improving the photocatalytic performance of graphene-TiO_2 nanocomposites via a combined strategy of decreasing defects of graphene and increasing interfacial contact. Phys. Chem. Chem. Phys. 2012 ; 14(25) :9167−75.

[56] Ferrari, A. C., Meyer, J. C., Scardaci, V., Casiraghi, C., Lazzeri, M., Mauri, F., *et al*. Raman spectrum of graphene and graphene layers. Phys. Rev. Lett. 2006; 97(18):187401.

[57] Testino, A., Bellobono, I. R., Buscaglia, V., Canevali, C., D'Arienzo, M., Polizzi, S., *et al*. Optimizing the photocatalytic properties of hydrothermal TiO_2 by the control of phase composition and particle morphology. J. Am. Chem. Soc. 2007; 129(12):3564–75.

[58] Davis, E. A., Mott, N. Conduction in non-crystalline systems V. Conductivity, optical absorption and photoconductivity in amorphous semiconductors. Philos. Mag. A 1970; 22(179):903–22.

[59] Hao, Y., Wang, Y., Wang, L., Ni, Z., Wang, Z., Wang, R., *et al*. Probing layer number and stacking order of few-layer graphene by Raman spectroscopy. Small 2010; 6(2):195–200.

[60] Bonaccorso, F., Lombardo, A., Hasan, T., Sun, Z., Colombo, L., Ferrari, A. C. Production and processing of graphene and 2d crystals. Mater. Today 2012; 15(12):564–89.

[61] C. Valles, C. Drummond, H. Saadaoui, C.A. Furtado, M. He, O. Roubeau, *et al*. Solutions of negatively charged graphene sheets and ribbons. J. Am. Chem. Soc. 2008; 130(47):15802–4.

[62] Shearer, C. J., Slattery, A. D., Stapleton, A. J., Shapter, J. G., Gibson, C. T. Accurate thickness measurement of graphene. Nanotechnol. 2016; 27(12):125704.

[63] Tuinstra, F., Koenig, J. L. Raman spectrum of graphite. J. Chem. Phys. 1970; 53(3):1126–30.

[64] Kudin, K. N., Ozbas, B., Schniepp, H. C., Prud'Homme, R. K., Aksay, I. A., Car, R. Raman spectra of graphite oxide and functionalized graphene sheets. Nano Lett. 2008; 8(1):36–41.

[65] Rao, K. S., Senthilnathan, J., Liu, Y. F., Yoshimura, M. Role of peroxide ions in formation of graphene nanosheets by electrochemical exfoliation of graphite. Sci. Rep. 2014; 4:4237.

[66] Yu, P., Lowe, S. E., Simon, G. P., Zhong, Y. L. Electrochemical exfoliation of graphite and production of functional graphene. Curr. Opin. Colloid Interf. Sci. 2015; 20(5):329–38.

[67] Yang, Y., Liu, E., Dai, H., Kang, L., Wu, H., Fan, J., *et al*. Photocatalytic activity of Ag-TiO_2-graphene ternary nanocomposites and application in hydrogen evolution by water splitting. Int. J. Hydrog. Energy. 2014; 39(15):7664−71.

[68] Chen, D., Zou, L., Li, S., Zheng, F. Nanospherical like reduced graphene oxide decorated TiO_2 nanoparticles: An advanced catalyst for the hydrogen evolution reaction. Sci. Rep. 2016; 6:20335.

[69] Zheng, C., He, C., Zhang, H., Wang, W., Lei, X. TiO_2-reduced graphene oxide nanocomposite for high-rate application of Lithium ion batteries. Ionics 2015; 21(1):51–8.

[70] Zou, B., Wang, X. X., Huang, X. X., Wang, J. N. Continuous synthesis of graphene sheets by spray pyrolysis and their use as catalysts for fuel cells. Chem. Commun. 2015; 51(4):741–4.

[71] Yang, J., Liao, Q., Zhou, X., Liu, X., Tang, J. Efficient synthesis of graphene-based powder via *in situ* spray pyrolysis and its application in Lithium ion batteries. RSC Adv. 2013; 3(37):16449–55.

[72] Malard, L. M., Nilsson, J., Elias, D. C., Brant, J. C., Plentz, F., Alves, E. S., *et al*. Probing the electronic structure of bilayer graphene by Raman scattering. Phys. Rev. B 2007; 76(20):201401.

[73] Lin, Z., Ye, X., Han, J., Chen, Q., Fan, P., Zhang, H., *et al*. Precise control of the number of layers of graphene by picosecond laser thinning. Sci. Rep. 2015; 5:11662.

[74] Yang, N., Zhai, J., Wang, D., Chen, Y., Jiang, L. Two-dimensional graphene bridges enhanced photoinduced charge transport in dye-sensitized solar cells. ACS Nano 2010; 4(2):887–94.

[75] Mangal, M., Jangid, V. Synthesis and antimicrobial studies of indolyl pyrimidines. Heterocycl. Lett. 2016; 6(4):795–803.

[76] Wang, H., Yan, S., Salley, S. O., Ng, K. S. Support effects on hydrotreating of soybean oil over NiMo carbide catalyst. Fuel 2013; 111:81–7.

[77] Neto, N., Ambrosino, F., Califano, S. Vibrational assignment of phenazine and phenazine-d_8: Crystal spectra in polarized light and force constants calculations. Spectrochim. Acta 1964; 20(10):1503–16.

[78] Ćirić-Marjanović, G., Blinova, N. V., Trchová, M., Stejskal, J. Chemical oxidative polymerization of safranines. J. Phys. Chem. B 2007; 111(9):2188–99.

[79] Devi, L., Arjunan, V., Marchewka, M. K., Mohan, S. Conformational analysis, structural and vibrational investigations of trans-2-chlorocinnamic acid and trans-4-chlorocinnamic acid. In: J. Ebenezar (eds). Recent Trends in Materials Science and Applications. Springer Proceedings in Physics, vol 189. Springer, Cham; 2017:563–98.

[80] Ding, P., Qu, B. Synthesis and characterization of exfoliated polystyrene/ZnAl layered double hydroxide nanocomposite via emulsion polymerization. J. Colloid Interf. Sci. 2005; 291(1):13–8.

[81] Zhang, Y., Tang, Z. R., Fu, X., Xu, Y. J. TiO_2-graphene nanocomposites for gas-phase photocatalytic degradation of volatile aromatic pollutant: Is TiO_2-graphene truly different from other TiO_2-carbon composite materials? ACS Nano 2010; 4(12):7303–14.

[82] Anjusree, G. S., Nair, A. S., Nair, S. V., Vadukumpully, S. One-pot hydrothermal synthesis of TiO_2/graphene nanocomposites for enhanced visible-light photocatalysis and photovoltaics. RSC Adv. 2013; 3(31):12933–8.

[83] Chen, L., Tuo, L., Rao, J., Zhou, X. TiO_2 doped with different ratios of graphene and optimized application in CdS/CdSe quantum dot-sensitized solar cells. Mater. Lett. 2014, 124:161–4.

[84] Kumar, S. G., Rao, K. S. R. K. Comparison of modification strategies towards enhanced charge carrier separation and photocatalytic degradation activity of metal oxide semiconductors (TiO_2, WO_3 and ZnO). Appl. Surf. Sci. 2017; 391:124–48.

[85] Park, H., Kim, H. I., Moon, G. H., Choi, W. Photoinduced charge transfer processes in solar photocatalysis based on modified TiO_2. Energy Environ. Sci. 2016; 9(2):411–33.

[86] Beams, R., Cançado, L. G., Novotny, L. Raman characterization of defects and dopants in graphene. J. Phys.: Condens. Matter. 2015; 27(8):083002.

[87] Reddy, K. M., Reddy, C. G., Manorama, S. V. Preparation, characterization, and spectral studies on nanocrystalline anatase TiO_2. J. Solid State Chem. 2001; 158(2):180–6.

[88] Aarik, J., Mandar, H., Kirm, M. Spectroscopic characterization of ZrO_2 thin films grown by atomic layer deposition. Proc. Estonian Acad. Sci. Phys. Math. 2003; 52(3):289–98.

[89] Murphy, A. B. Band-gap determination from diffuse reflectance measurements of semiconductor films, and application to photoelectrochemical water-splitting. Sol. Energy Mater. Sol. Cells 2007; 91(14):1326–37.

[90] Masnadi-Shirazi, M., Lewis, R. B., Bahrami-Yekta, V., Tiedje, T., Chicoine, M., Servati, P. Bandgap and optical absorption edge of $GaAs_{1-x}Bi_x$ alloys with $0 < x < 17.8\%$. J. Appl. Phys. 2014; 116(22):223506.

[91] Brus, L. E. Electron-electron and electron-hole interactions in small semiconductor crystallites: The size dependence of the lowest excited electronic state. J. Chem. Phys. 1984; 80(9):4403–9.

[92] Brus, L. Electronic wave functions in semiconductor clusters: experiment and theory. The J. Phys. Chem. 1986; 90(12):2555–60.

[93] Rino, J. P., Studart, N. Structural correlations in titanium dioxide. Phys. Rev. B 1999; 59(10):6643–9.

[94] Anpo, M., Shima, T., Kodama, S., Kubokawa, Y. Photocatalytic hydrogenation of propyne with water on small-particle titania: Size quantization effects and reaction intermediates. J. Phys. Chem. 1987; 91(16):4305–10.

[95] Kormann, C., Bahnemann, D. W., Hoffmann, M. R. Preparation and characterization of quantum-size titanium dioxide. J. Phys. Chem. 1988; 92(18):5196–201.

[96] Lin, H., Huang, C. P., Li, W., Ni, C., Shah, S. I., Tseng, Y. H. Size dependency of nanocrystalline TiO_2 on its optical property and photocatalytic reactivity exemplified by 2-chlorophenol. Appl. Catal. B: Environ. 2006; 68(1–2):1–11.

[97] Tang, H., Berger, H., Schmid, P. E., Levy, F., Burri, G. Photoluminescence in TiO_2 anatase single crystals. Solid State Commun. 1993; 87(9):847–50.

[98] Tang, H., Prasad, K., Sanjines, R., Schmid, P. E., Levy, F. Electrical and optical properties of TiO_2 anatase thin films. J. Appl. Phys. 1994; 75(4):2042–7.

[99] Anpo, M., Aikawa, N., Kubokawa, Y., Che, M., Louis, C., Giamello, E. Photoluminescence and photocatalytic activity of highly dispersed titanium oxide anchored onto porous Vycor glass. J. Phys. Chem. 1985; 89(23):5017–21.

[100] Yadav, A., Yadav, M., Gupta, S., Popat, Y., Gangan, A., Chakraborty, B., *et al.* Effect of graphene oxide loading on TiO_2: Morphological, optical, interfacial charge dynamics-A combined experimental and theoretical study. Carbon 2019; 143:51–62.

[101] Williams, G., Kamat, P. V. Graphene–semiconductor nanocomposites: Excited-state interactions between ZnO nanoparticles and graphene oxide. Langmuir 2009; 25(24):13869–73.

[102] Yang, M. Q., Xu, Y. J., Lu, W., Zeng, K., Zhu, H., Xu, Q. H., *et al.* Self-surface charge exfoliation and electrostatically coordinated 2D hetero-layered hybrids. Nat. Commun. 2017; 8(1): 1–9.

[103] Mohan, D., Singh, K. P. Single-and multi-component adsorption of cadmium and zinc using activated carbon derived from bagasse-an agricultural waste. Water Res. 2002; 36(9):2304–18.

[104] Kumar, K. V., Porkodi, K. Mass transfer, kinetics and equilibrium studies for the biosorption of methylene blue using Paspalum notatum. J. Hazard. Mater. 2007; 146(1–2):214–26.

[105] Arasteh, R., Masoumi, M., Rashidi, A. M., Moradi, L., Samimi, V., Mostafavi, S. T. Adsorption of 2-nitrophenol by multi-wall carbon nanotubes from aqueous solutions. Appl. Surf. Sci. 2010; 256(14):4447–55.

[106] Liu, F., Chung, S., Oh, G., Seo, T. S. Three-dimensional graphene oxide nanostructure for fast and efficient water-soluble dye removal. ACS Appl. Mater. Interf. 2012; 4(2):922–7.

[107] Zhou, H., Smith, D. W. Advanced technologies in water and wastewater treatment. J. Environ. Eng. Sci. 2002; 1(4):247–64.

[108] Li, W., Li, D., Wang, J., Shao, Y., You, J., Teng, F. Exploration of the active species in the photocatalytic degradation of methyl orange under UV light irradiation. J. Mol. Catal. A: Chem. 2013; 380:10–7.

[109] Zhang, D., Qiu, R., Song, L., Eric, B., Mo, Y., Huang, X. Role of oxygen active species in the photocatalytic degradation of phenol using polymer sensitized TiO_2 under visible light irradiation. J. Hazard. Mater. 2009; 163(2–3):843–7.

[110] Mohamed, H. H., Bahnemann, D. W. The role of electron transfer in photocatalysis: Fact and fictions. Appl. Catal. B: Environ. 2012; 128:91–104.

[111] Korycka-Dahl, M., Richardson, T. Initiation of oxidative changes in foods. J. Dairy Sci. 1980; 63(7):1181–98.

[112] Pignatello, J. J., Oliveros, E., MacKay, A. Advanced oxidation processes for organic contaminant destruction based on the Fenton reaction and related chemistry. Crit. Rev. Environ. Sci. Technol. 2006; 36(1):1–84.

CHAPTER 3: Solvents screening for efficient chemical exfoliation of graphite

Abstract

Chemical exfoliation of graphite is an effective method to produce graphene of relative high quality, where the choice of solvents plays an important role in the product yield and quality. Here, screening of different solvents and their mixtures for the liquid-phase exfoliation of graphite was performed under ultrasonication. A synergistic effect among aromatic, amine, and halogen groups was identified. The synergy was more effectively exploited when these functional groups were combined through solvent mixtures compared to when they were introduced in the molecular structure of single solvents.

Chapter 3

3.1. Introduction

Novoselov and Geim demonstrated the production of graphene by peeling graphite with a Scotch tape [1]. As such, one of the advantages of graphene over the other carbon nanomaterials is that it is directly producible from graphite in a top-down manner. This fact indicates that the cost of graphene would be comparable to that of graphite if the production process became highly efficient. Currently, the production of graphene at a relatively large scale mainly relies on the graphene oxide (GO) route [2–5]. Graphite is oxidized by potassium permanganate in a sulfuric acid media [6]. This leads to GO with various oxygen-containing functional groups introduced onto graphene sheets. Thermal or chemical reduction of GO eventually affords graphene, also termed reduced GO. Disadvantages of the GO route are that it emits a huge amount of harmful wastes and that it leaves non-negligible chemical and structural defects on graphene sheets [7–11].

Thus, liquid-phase exfoliation without relying on chemical energy is regarded a promising alternative for the mass production of graphene of a higher quality [12]. Here, the higher quality refers to graphene consisting of fewer layers with a reduced defect density. The route requires physical energy for achieving exfoliation as well as a solvent for stabilizing produced graphene sheets as a dispersion. The most frequently employed physical energy is cavitation, which includes ultrasonication [13–15], jet cavitation [16–19], and high-pressure homogenization [20,21]. A variety of solvents have been reported as effective for liquid-phase exfoliation of graphite. Among these, N-methylpyrrolidone [22,23], 1,2-dichlorobenzene [24,25], and benzylamine [26,27] are the most popular solvents, which are originally used to disperse other carbon nanomaterials, and indeed afford high-quality graphene. Other known solvents include N,N-dimethylformamide [28], dimethyl sulfoxide [29], 1,3-dimethyl-2-imidazolidinone, N,N-dimethylacetamide, γ-butyrolactone [23], and etc. Early attempts to find exfoliation solvents focused on the

production of high-quality graphene at a higher yield. In general, the yield and quality of graphene are not solely determined by the choice of the solvents. For instance, prolonged ultrasonication monotonously enhances the graphene yield in cost of defect formation, and centrifugation at a higher speed provides thinner graphene sheets by sacrificing the yield. Nonetheless, the yield in literature mostly fell in the range of 0.1–1 mg of graphene per milliliter of a solvent [22–29]. Another focus of solvent exploration is the development of a green process. The addition of a surfactant or a polymer compensates a gap of the surface tension [13,30–35]. This enables exfoliation of graphite even in water, while the persistence of the additive during the solvent removal is an important issue to be solved. Last, exploration of exfoliation solvents finds its motivation in the diversification of the solvent library. Such research aims not only to provide proper solvents for individual applications, but also to understand molecular features that determine the yield and quality of produced graphene. Many of exfoliation solvents possess surface tension close to that of graphene (40 mJ m^{-2}) [36], but this does not explain large deviation of the yield among solvents with comparable surface tension. Other features such as the Hildebrand and Hansen solubility parameters also posed a similar problem, arising from the difficulty to describe molecular interaction based on macroscopic parameters. In 2009, Bourlinos et al. reported a number of new exfoliating solvents [30]. Starting from the finding of perfluorinated aromatic molecules as exfoliation solvents, they hypothesized a role of electron withdrawing groups in augmenting π–π interaction through charge transfer. Then, they claimed electron donating groups may hold a similar augmenting role as pyridine was usable as an exfoliation solvent. However, these features in addition to the surface tension matching still do not completely describe the inability of some solvents such as aniline, pyrrole, and thiophene.

This Chapter delivers my efforts on further solvent exploration for the liquid-phase exfoliation of graphite under ultrasonication. A number of exfoliation solvents were newly identified. In particular, chlorobenzylamine, a combination of the molecular structures of two famous exfoliation solvents, i.e. chlorobenzene and benzylamine, exhibited the highest graphene yield. Titanium alkoxide gave a reasonable yield even though its surface tension was much lower than that of graphene. The most important finding of this study is that a synergy of combining different functional groups is better exploited in a form of solvent mixtures, e.g. a chlorobenzene/benzylamine mixture gave a better yield than chlorobenzylamine.

3.2. Materials and methods

3.2.1. Materials

Graphite powder (≥ 98%, 45 μm) was obtained from Wako Pure Chemical Industries. Graphene nanoplatelets (GNP) (Strem Chemicals) with the surface area of 750 m^2 g^{-1} was used to estimate the concentration of a graphene dispersion. Solvents, as an exfoliation media of graphite, were purchased from either of TCI Chemicals, TCI Chemicals, and Wako Pure Chemical Industries. Air/water-sensitive chemicals (such as benzylamine derivatives, titanium alkoxide) were appropriately stored and handled in an inert atmosphere.

3.2.2. Chemical exfoliation of graphite

44 mg of graphite suspended in 5.0 mL of a solvent was sonicated at 43 kHz and 60 ℃ for 4 h. The resultant mixture was centrifuged at 2000 rpm for 2 h to precipitate a non-exfoliated portion of graphite. A graphene dispersion was obtained as the supernatant. The performance of a solvent or solvent mixture was evaluated in two stages. First, the

appearance of a supernatant was classified into clear (no graphene yield), gray (yield below 0.1 mg mL^{-1}), and black (yield over 0.1 mg mL^{-1}). When classified into black, the graphene concentration of the supernatant was determined based on the absorbance at 550 nm (JASCO V-670 UV-Vis spectrometer). The measured absorbance was referenced to a calibration curve that was externally acquired using GNP dispersions.

3.3. Results and discussion

3.3.1. Screening of single solvents

First, 57 single solvents were screened for the liquid-phase exfoliation of graphite under ultrasonication. These commercially available solvents were selected for variation in chemical structures and for reasons described later. The screening was performed in two steps: When the supernatant looked clear or grayish, the yield was regarded to be 0 or < 0.1 mg mL^{-1}, respectively; When black, the graphene concentration was quantified based on UV/Vis measurements. Table 3.1 summarizes the screening results for the 57 single solvents. The surface tension values are also shown when they are available in literature.

The screening was started from the four most popular solvents: N-methylpyrrolidone (NMP), N,N-dimethylformamide (DMF), benzylamine (BA), and 1,2-dichlorobenzene (ODCB), corresponding to Runs 1–4 in Table 3.1. They possess surface tension comparable to that of graphene and exhibited an exfoliation ability from weak to reasonable. Then, the screening was extended to derivatives and related compounds of BA and ODCB (note that few derivatives are commercially available for NMP and DMF). Such selection was based on a consideration that combinations of specific functional groups could be important in addition to the surface tension matching. This consideration was indeed effective to identify new solvents: A combination of an aliphatic amine and an aromatic ring led to relatively

high exfoliation yields (Runs 5,7), unless the amine was ternary (Run 6). The utilization of an aromatic amine instead of aliphatic one (Runs 8–10), the lack of the aromatic ring (Runs 11,12), and the substitution with electron-withdrawing groups (Runs 13,14) were found to be all negative. Regarding BA and relevant solvents, one can notice that the surface tension matching hardly explains the exfoliation capability of these solvents. In general, surface tension is related to the strength of intermolecular interactions within a liquid and does not describe an interaction between solvent molecules and graphene. The essentiality of the aromatic ring clearly indicates an interaction based on π–π stacking. One potential scenario is that an aliphatic amine orients outwards to assist the solvation of solvent-decorated graphene sheets. This would explain the necessity of a hydrocarbon spacer (between the aromatic ring and the amine) and the N–H bond for stronger solvation. Among ODCB-related compounds, only chlorobenzens exhibited the exfoliation capability in moderate yields (Runs 15,16). Substitution with heavier halogens failed plausibly due to their insufficient acceptor ability for π–π stacking (Runs 17,18) [36,37]. Aliphatic chlorides also failed simply due to the lack of the aromatic ring.

According to the above results and discussion, combinations of effective functional groups were expected to be more reliable than the surface tension for describing the exfoliation ability. Thus, halogenated benzylamine derivatives were tested (Runs 23–25). It was found that these solvents bearing three effective functional groups improved the exfoliation yield 1.5–2 times compared to BA and ODCB having only two functional groups. At the best of my knowledge, a synergism among different functional groups was not reported elsewhere, and this implies a cooperative mechanism in stabilizing exfoliated graphene, e.g. aryl chloride for π–π stacking [38] and alkyl amine for solvation.

At the end of the screening of single solvents, a variety of unproven solvents were tested. Briefly, only 2-ethylhaxanol and 2-methoxyethanol exhibited a weak exfoliation ability

among alcohols (Runs 27–36). No exfoliation ability was observed for ketones (Runs 37,38), esters (Runs 39–41), and aliphatic and aromatic hydrocarbons (Runs 42–53). In Chapter 2, I reported the exfoliation of graphite using titanium tetra-*n*-butoxide, and the obtained dispersion was used to prepare TiO_2/graphene nanocomposites as highly efficient photocatalysts under visible light [11]. Here, the exfoliation ability of titanium alkoxides was confirmed (Runs 54,55). Conversely, titanium tetrachloride and silicon tetraethoxysilane did not show exfoliation (Runs 56,57). The formation of stable intercalation compounds due to strong donor-acceptor interactions was reported for many Lewis acidic compounds including metal chlorides [39]. Probably, a moderate donor-acceptor interaction is required for the exfoliation, as an excessively strong interaction results in an assembled intercalation compound.

Table 3.1. Screening results for single solvents

Run	Solvent	Functional groups	Surface tension[40–47] [mJ m^{-2}]	Yield[a] [mg mL^{-1}]
1	N-Methylpyrrolidone	Cycloalkylamide	40.79	0.2
2	N,N-Dimethylformamide	Alkylamide	36.42	<0.1
3	Benzylamine	R–NH_2, aromatic	38.82	0.2
4	1,2-Dichlorobenzene	Aryl halide (Cl)	36.61	0.1
5	N-Methylbenzylamine	R_2–NH, aromatic	n.d.	0.3
6	N,N-Dimethylbenzylamine	R_3–N, aromatic	38.81	0
7	3-Phenylpropylamine	R–NH_2, aromatic	37.6	0.3
8	2,6-Diisopropylaniline	Ar–NH_2	33.9	<0.1
9	2,4,6-Trimethylaniline	Ar–NH_2	33.92	<0.1
10	Aniline	Ar–NH_2	43.40	0
11	Triethylamine	R_3–N	20.22	0
12	Ethylenediamine	R–NH_2	42	0
13	Benzonitrile	Nitrile, aromatic	38.79	0
14	Nitrobenzene	Nitro, aromatic	46.34	0
15	1,2,4-Trichlorobenzene	Aryl halide (Cl)	39.1	0.2
16	Monochlorobenzene	Aryl halide (Cl)	33.60	0.2
17	Bromobenzene	Aryl halide (Br)	36.50	0
18	Iodobenzene	Aryl halide (I)	39.70	0
19	Chloroform	Alkyl halide (Cl)	27.50	0
20	1,2-Dichloroethane	Alkyl halide (Cl)	33.30	0
21	Dichloromethane	Alkyl halide (Cl)	26.50	0
22	Tetrachloroethylene	Alkenyl halide (Cl)	31.74	0
23	2-Chlorobenzylamine	R–NH_2, aryl halide (Cl)	42.0	0.5
24	4-Chlorobenzylamine	R–NH_2, aryl halide (Cl)	42.0	0.4
25	2-Fluorobenzylamine	R–NH_2, aryl halide (F)	n.d.	0.3
26	2-Chloroaniline	Ar–NH_2, aryl halide	43.66	0

27	Benzylalcohol	Alcohol	39.00	0
28	2-Ethylhexanol	Alcohol	28.00	0.1
29	2-Methoxyethanol	Alcohol, ether	30.84	<0.1
30	Methanol	Alcohol	22.70	0
31	Ethanol	Alcohol	22.10	0
32	1-Propanol	Alcohol	23.75	0
33	2-Propanol	Alcohol	23.00	0
34	1-Butanol	Alcohol	24.93	0
35	2-Butanol	Alcohol	23.0	0
36	2-Methyl-1-propanol	Alcohol	23.0	0
37	Acetone	Ketone	25.20	0
38	2-Butanone	Ketone	23.97	0
39	Methylmethacrylate	Ester	28	0
40	Diethylphthalate	Aromatic, ester	37.5	0
41	Dibutylphthalate	Aromatic, ester	34	0
42	Styrene	Aromatic hydrocarbon	32.3	0
43	4-Methylstyrene	Aromatic hydrocarbon	n.d.	0
44	Benzene	Aromatic hydrocarbon	28.88	0
45	Xylene	Aromatic hydrocarbon	30.10	0
46	Toluene	Aromatic hydrocarbon	28.40	0
47	1-Octene	Aliphatic hydrocarbon	21.76	0
48	1-Decene	Aliphatic hydrocarbon	24	0
49	Octane	Aliphatic hydrocarbon	21.62	0
50	Hexane	Aliphatic hydrocarbon	18.43	0
51	n-Tetradecane	Aliphatic hydrocarbon	26.56	0
52	Hexadecane	Aliphatic hydrocarbon	27.47	0
53	Cyclohexane	Aliphatic hydrocarbon	24.95	0
54	Titanium tetra-*n*-butoxide	Titanium alkoxide	28.0	0.3
55	Titanium tetraethoxide	Titanium alkoxide	23.1	0.2
56	Titanium tetrachloride	Titanium halide (Cl)	n.d.	0
57	Tetraethoxysilane	Silicone alkoxide	22.8	0

[a] The screening was performed in two steps: When the supernatant looked clear or grayish, the graphene yield was regarded to be 0 or < 0.1 mg mL^{-1}, respectively; When black, the graphene concentration was quantified based on UV/Vis measurements.

3.3.2. Screening of solvent mixtures

In the screening of single solvents, synergism of combining effective functional groups was suggested. However, to achieve the coexistence of multiple functional groups within a single molecule is not practical in terms of synthetic elaboration and the temperature range of a liquid state. It was considered that if these functional groups owed different roles in stabilizing exfoliated graphene sheets, synergism would be also exploited in the form of solvent mixtures. Thus, a series of solvent mixtures were screened. The results are shown in Table 3.2. The mixtures consisted of two or three solvents, at least one of which was selected from effective solvents. In this study, the screening was limited to equivolume mixtures so that the yield would be improved from the reported values through optimization

of the mixture composition. The surface tension of a mixture was estimated based on the mole-fraction-weighted average of the surface tension of individual components [48].

As can be seen in Table 3.2, the equivolume mixtures of BA and a chlorobenzene (i.e. combinations of two effective solvents) led to a graphene yield, which was far greater than those for the corresponding two solvents, or their average yields (Runs 58–60). Among these, the performance of the BA/ODCB mixture was even superior to that of 2-chlorobenzylamine, the best single solvent. These results proved my hypothesis that the synergism of combining effective functional groups holds even when the combination is achieved based on a solvent mixture. It is hard to determine which intra- or intermolecular combination was superior since the composition of the effective functional groups was not identical (e.g. the amine/aromatic ring molar ratio is ca. 1/2 for BA/ODCB and 1/1 for 2-chlorobenzylamine). However, the solvent mixture is considered as more advantageous due to the above-mentioned reasons as well as due to the tunability of the composition for desired applications.

Next, binary mixtures of strong solvents (those with the graphene yield above 0.1 mg mL^{-1}) and weak solvents (those with the graphene yield equal to or below 0.1 mg mL^{-1}) were tested (Runs 61–67). It can be seen that these mixtures gave yield values not far greater than those for the corresponding strong solvents (e.g. 0.3 mg mL^{-1} for 2-ethylhexanol/BA vs. 0.3 mg mL^{-1} for BA), but still greater than the estimation from the average (0.3 mg mL^{-1} (measured) vs. 0.16 mg mL^{-1} (estimated) for 2-ethylhexanol/BA). Thus, the synergism of effective functional groups was again confirmed in these mixtures. Exceptions were also observed. When two chlorozbenzens were mixed, the graphene yield became completely zero (Runs 68–70). It is known that organic halides undergo polymerization and decomposition when subjected to elongated ultrasonication [25,28,49,50]. Probably, the mixtures accelerated such decomposition as compared to single

solvents. It was also found that the addition of non-solvents (i.e. no exfoliation ability) strongly deteriorates the ability of effective solvents. In Runs 71–81, the addition of ethanol or methanol eliminated or greatly diminished the yields. Similar synergism (Runs 82–85) and antagonism (Runs 86,87) were observed in ternary mixtures.

To the end of the screening, an alternative merit of studying solvent mixtures is denoted. Titanium alkoxides possessed an ability to stabilize exfoliated graphene sheets (Runs 54,55). In the previous Chapter, the graphene dispersion in titanium tetra-*n*-butoxide was used as a direct precursor to prepare TiO_2/graphene nanocomposites suitable for visible-light photocatalysis [11]. On the other hand, it is known that most of Lewis acidic metal alkoxides are solids at normal temperature. The solvent-mixture strategy can alleviate such the problem. In Run 88, 500 mg of aluminum isopropoxide, a crystalline solid at room temperature, was dissolved in 5.0 mL of ODCB. Then, this solution was used to obtain a graphene dispersion by ultrasonication, which would derive to graphene@Al_2O_3 nanocomposites in relation to highly thermal conductive fillers with electric insulation coating [51].

Table 3.2. Screening results for solvent mixtures

Run	Solvent mixture[a]	Surface tension[b] [mJ m^{-2}]	Yield [mg mL^{-1}]
58	Benzylamine/1,2-dichlorobenzene	37.73	0.6
59	Benzylamine/monochlorobenzene	36.11	0.5
60	Benzylamine/1,2,4-trichlorobenzene	38.95	0.4
61	2-Ethylhexanol/2-chlorobenzylamine	35.90	0.5
62	2-Ethylhexanol/benzylamine	34.37	0.3
63	2-Ethylhexanol/1,2,4-trichlorobenzene	34.18	0.2
64	N,N-Dimethylformamide/benzylamine	37.42	0.3
65	N,N-Dimethylformamide/monochlorobenzene	35.20	0.1
66	N,N-Dimethylformamide/1,2-dichlorobenzene	36.49	0.3
67	N,N-Dimethylformamide/1,2,4-trichlorobenzene	37.45	0.3
68	Monochlorobenzene/1,2-dichlorobenzene	35.01	0
69	Monochlorobenzene/1,2,4-trichlorobenzene	36.07	0
70	1,2-Dichlorobenzene/1,2,4-trichlorobenzene	37.79	0
71	Ethanol/N,N-dimethylformamide	28.26	<0.1

72	Ethanol/benzylamine	27.93	<0.1
73	Ethanol/1,2,4-trichlorobenzene	27.53	0
74	Ethanol/monochlorobenzene	26.30	0
75	Ethanol/2-ethylhexanol	23.70	0
76	Methanol/N,N-dimethylformamide	27.41	0
77	Methanol/benzylamine	26.83	0
78	Methanol/monohlorobenzene	25.81	0
79	Methanol/1,2-dichlorobenzene	26.36	0
80	Methanol/1,2,4-trichlorobenzene	26.73	0
81	Methanol/2-ethylhexanol	23.79	0
82	2-Ethylhexanol/benzylamine/1,2,4-trichlorobenzene	35.98	0.8
83	2-Ethylhexanol/benzylamine/1,2-dichlorobenzene	35.18	0.7
84	2-Ethylhexanol/benzylamine/monochlorobenzene	34.08	0.5
85	2-Ethylhexanol/benzylamine/2-chlorobenzylamine	37.02	0.5
86	Ethanol/1,2-dichlorobenzene/benzylamine	30.11	0
87	Methanol/1,2-dichlorobenzene/benzylamine	29.03	0
88[c]	Aluminum isopropropoxide/1,2-dichlorobenzene	n.d.	<0.1

[a] Equivolume mixtures of two or three solvents.
[b] The surface tension of a solvent mixture was derived based on the mole-fraction-weighted average of the surface tension of individual solvents.
[c] 500 mg of aluminum isopropropoxide in a solid state was dissolved in 5.0 mL of 1,2-dichlorobenzene, and the resultant mixture was used for the exfoliation of graphite.

3.4. Conclusion

Liquid-phase exfoliation of graphite is a promising method for large-scale production of high-quality graphene. A solvent plays a role of stabilizing exfoliated graphene sheets and exerts a significant influence on the productivity of the process. Here, screening of different solvents and their mixtures for the liquid-phase exfoliation of graphite was performed under ultrasonication. The aims of such screening were to diversify available solvents for individual applications, and to understand molecular features that determine the graphene yield. The major findings were summarized below.

i) Out of 57 single solvents tested, 17 solvents exhibited an ability to stabilize exfoliated graphene sheets. A combination of effective functional groups was effective for exploring

new solvents. In particular, chlorobenzylamine, which possesses aryl chloride and aliphatic amine as effective functional groups, exhibited the best yield among the single solvents.

ii) The most important finding here is that synergism among effective functional groups is obtained not only when they were introduced in the molecular structure of single solvents but also when they were combined through solvent mixtures. Solvent mixture as a choice of the exfoliation medium are advantageous in terms of the availability, diversity and tunability compared with single solvents.

iii) Based on the strategy of solvent mixtures, it was possible to prepare a graphene dispersion with metal alkoxides, as precursors for functional oxide@graphene nanocomposites.

I believe these findings are useful in further exploration of exfoliation solvents, as well as in applied studies of using high-quality graphene as functional nanomaterials.

3.5. References

[1] Novoselov, K. S., Geim, A. K., Morozov, S. V., Jiang, D., Zhang, Y., Dubonos, S. V., *et al.* Electric field effect in atomically thin carbon films. Science 2004; 306(5696):666–9.

[2] Stankovich, S., Dikin, D. A., Piner, R. D., Kohlhaas, K. A., Kleinhammes, A., Jia, Y., *et al.* Synthesis of graphene-based nanosheets via chemical reduction of exfoliated graphite oxide. Carbon 2007; 45(7):1558–65.

[3] Eigler, S., Grimm, S., Enzelberger-Heim, M., Müller, P., Hirsch, A. Graphene oxide: Efficiency of reducing agents. Chem. Commun. 2013; 49(67):7391–3.

[4] Zhu, Y., Murali, S., Cai, W., Li, X., Suk, J. W., Potts, J. R., *et al.* Graphene and graphene oxide: Synthesis, properties, and applications. Adv. Mater. 2010; 22(35):3906–24.

[5] Dreyer, D. R., Murali, S., Zhu, Y., Ruoff, R. S., Bielawski, C. W. Reduction of graphite oxide using alcohols. J. Mater. Chem. 2011; 21(10):3443–7.

[6] Hummers Jr, W. S., Offeman, R. E. Preparation of graphitic oxide. J. Am. Chem. Soc. 1958; 80(6):1339.

[7] Jiang, G., Lin, Z., Chen, C., Zhu, L., Chang, Q., Wang, N., *et al.* TiO_2 nanoparticles assembled on graphene oxide nanosheets with high photocatalytic activity for removal of pollutants. Carbon 2011; 49(8):2693–701.

[8] Xu, T., Zhang, L., Cheng, H., Zhu, Y. Significantly enhanced photocatalytic performance of ZnO via graphene hybridization and the mechanism study. Appl. Catal. B: Environ. 2011; 101(3–4):382–7.

[9] Larciprete, R., Fabris, S., Sun, T., Lacovig, P., Baraldi, A., Lizzit, S. Dual path mechanism in the thermal reduction of graphene oxide. J. Am. Chem. Soc. 2011; 133(43):17315–21.

[10] Liu, X., Pan, L., Lv, T., Zhu, G., Lu, T., Sun, Z., *et al.* Microwave-assisted synthesis of TiO_2-reduced graphene oxide composites for the photocatalytic reduction of Cr(VI). RSC Adv. 2011; 1(7):1245–9.

[11] Ton, N. N. T., Dao, A. T. N., Kato, K., Ikenaga, T., Trinh, D. X., Taniike, T. One-pot synthesis of TiO_2/graphene nanocomposites for excellent visible light photocatalysis based on chemical exfoliation method. Carbon 2018; 133:109–17.

[12] Nicolosi, V., Chhowalla, M., Kanatzidis, M. G., Strano, M. S., Coleman, J. N. Liquid exfoliation of layered materials. Science 2013; 340(6139):1226419.

[13] Lotya, M., King, P. J., Khan, U., De, S., Coleman, J. N. High-concentration, surfactant-stabilized graphene dispersions. ACS Nano 2010; 4:3155–62.

[14] Khan, U., Neill, A. O., Lotya, M., De, S., Coleman, J. N. High-concentration solvent exfoliation of graphene. Small 2010; 6:864–71.

[15] Shen, J., He, Y., Wu, J., Gao, C., Keyshar, K., Zhang, X., *et al.* Liquid phase exfoliation of two-dimensional materials by directly probing and matching surface tension components. Nano Lett. 2015; 15(8):5449–54.

[16] Shen, Z., Li, J., Yi, M., Zhang, X., Ma, S. Preparation of graphene by jet cavitation. Nanotechnology 2011; 22(36):365306.

[17] Wang, J., Shen, Z., Yi, M. Liquid-exfoliated graphene as highly efficient conductive additives for cathodes in Lithium ion batteries. Carbon 2019; 153:156–63.

[18] Lin, P. C., Wu, J. Y., Liu, W. R. Green and facile synthesis of few-layer graphene via liquid exfoliation process for Lithium-ion batteries. Sci. Rep. 2018; 8(1):1–8.

[19] Yi, M., Li, J., Shen, Z., Zhang, X., Ma, S. Morphology and structure of mono-and few-layer graphene produced by jet cavitation. Appl. Phys. Lett. 2011; 99(12):123112.

[20] Nacken, T. J., Damm, C., Walter, J., Rüger, A., Peukert, W. Delamination of graphite in a high-pressure homogenizer. Rsc Adv. 2015; 5(71):57328–38.

[21] Qi, X., Zhang, H. B., Xu, J., Wu, X., Yang, D., Qu, J., *et al.* Highly efficient high-pressure homogenization approach for scalable production of high-quality graphene sheets and sandwich-structured α-Fe_2O_3/graphene hybrids for high-performance Lithium-ion batteries. ACS Appl. Mater. Interfaces 2017; 9(12):11025–34.

[22] Hasan, T., Scardaci, V., Tan, P., Rozhin, A. G., Milne, W. I., Ferrari, A. C. Stabilization and “debundling” of single-wall carbon nanotube dispersions in N-methyl-2-pyrrolidone (NMP) by polyvinylpyrrolidone (PVP). J. Phys. Chem. C 2007; 111(34):12594–602.

[23] Hernandez, Y., Nicolosi, V., Lotya, M., Blighe, F. M., Sun, Z., De, S., *et al.* High-yield production of graphene by liquid-phase exfoliation of graphite. Nat. Nanotechnol. 2008; 3(9):563–8.

[24] Hamilton, C. E., Lomeda, J. R., Sun, Z., Tour, J. M., Barron, A. R. High-yield organic dispersions of unfunctionalized graphene. Nano Lett. 2009; 9(10):3460–2.

[25] Sahoo, S., Hatui, G., Bhattacharya, P., Dhibar, S., Das, C. K. One pot synthesis of graphene by exfoliation of graphite in ODCB. Graphene 2013; 2(1):42.

[26] Cai, M., Thorpe, D., Adamson, H., Schniepp, H. C. Methods of graphite exfoliation. J. Mater. Chem. 2012; 22(48):24992–5002.

[27] Economopoulos, S. P., Rotas, G., Miyata, Y., Shinohara, H., Tagmatarchis, N. Exfoliation and chemical modification using microwave irradiation affording highly functionalized graphene. ACS Nano 2010; 4(12):7499–507.

[28] Blake, P., Brimicombe, P. D., Nair, R. R., Booth, T. J., Jiang, D., Schedin, F., *et al.* Graphene-based liquid crystal device. Nano Lett. 2008; 8(6):1704–8.

[29] Du, W., Lu, J., Sun, P., Zhu, Y., Jiang, X. Organic salt-assisted liquid-phase exfoliation of graphite to produce high-quality graphene. Chem. Phys. Lett. 2013; 568:198–201.

[30] Bourlinos, A. B., Georgakilas, V., Zboril, R., Steriotis, T. A., Stubos, A. K. Liquid-phase exfoliation of graphite towards solubilized graphenes. Small 2009; 5(16):1841–5.

[31] Guardia, L., Fernández-Merino, M. J., Paredes, J. I., Solis-Fernandez, P., Villar-Rodil, S., Martinez-Alonso, A., *et al.* High-throughput production of pristine graphene in an aqueous dispersion assisted by non-ionic surfactants. Carbon 2011; 49(5):1653–62.

[32] Liang, Y. T., Hersam, M. C. Highly concentrated graphene solutions via polymer enhanced solvent exfoliation and iterative solvent exchange. J. Am. Chem. Soc. 2010; 132(50):17661–3.

[33] Wajid, A. S., Das, S., Irin, F., Ahmed, H. T., Shelburne, J. L., Parviz, D., *et al.* Polymer-stabilized graphene dispersions at high concentrations in organic solvents for composite production. Carbon 2012; 50(2):526–34.

[34] Patole, A. S., Patole, S. P., Kang, H., Yoo, J. B., Kim, T. H., Ahn, J. H. A facile approach to the fabrication of graphene/polystyrene nanocomposite by in situ microemulsion polymerization. J. Colloid. Interface Sci. 2010; 350(2):530–7.

[35] Li, X., Xiao, Y., Bergeret, A., Longerey, M., Che, J. Preparation of polylactide/graphene composites from liquid-phase exfoliated graphite sheets. Polym. Compos. 2014; 35(2):396403.

[36] Bissantz, C., Kuhn, B., Stahl, M. A medicinal chemist's guide to molecular interactions. J. Med. Chem. 2010; 53(14):5061–84.

[37] Li, H., Lu, Y., Liu, Y., Zhu, X., Liu, H., Zhu, W. Interplay between halogen bonds and π–π stacking interactions: CSD search and theoretical study. Phys. Chem. Chem. Phys. 2012; 14(28):9948–55.

[38] Georgakilas, V., Tiwari, J. N., Kemp, K. C., Perman, J. A., Bourlinos, A. B., Kim, K. S., *et al*. Noncovalent functionalization of graphene and graphene oxide for energy materials, biosensing, catalytic, and biomedical applications. Chem. Rev. 2016; 116(9):5464–519.

[39] Guo, Y., Peng, F., Wang, H., Huang, F., Meng, F., Hui, D., *et al.* Intercalation polymerization approach for preparing graphene/polymer composites. Polymers 2018; 10(1):61.

[40] Yaws, C. L. Thermophysical properties of chemicals and hydrocarbons, second ed. William Andrew. 2008.

[41] National Center for Biotechnology Information, National Library of Medicine. https://pubchem.ncbi.nlm.nih.gov/ (accessed 25 March 2020).

[42] DataPhysics Instruments GmbH. Surface tension values of some common test liquids for surface energy analysis. https://www.dataphysics-instruments.com/Downloads/Surface-Tensions-Energies.pdf (accessed 25 March 2020).

[43] The Dow Chemical Company. Safety data sheet. https://www.dow.com/en-us/support/sds-finder.html (accessed 25 March 2020).

[44] Look for Chemicals. https://www.lookchem.com/ (accessed 25 March 2020).

[45] Mikpokat-Helpdesk. Material safety data sheet (MSDS). http://www.microkat.gr/ (accessed 25 March 2020).

[46] Cameo Chemicals. Database of hazardous materials. https://cameochemicals.noaa.gov/ (accessed 25 March 2020).

[47] AZmax. https://www.azmax.co.jp/chemical/ (accessed 25 March 2020).

[48] Wang, P., Anderko, A., Young, R. D. Modeling surface tension of concentrated and mixed-solvent electrolyte systems. Ind. Eng. Chem. Res. 2011; 50(7):4086–98.

[49] Srivastava, S. C. Chemical reactions initiated by ultrasonic waves. Nature 1958; 182(4627):47.

[50] Moonoosawmy, K. R., Kruse, P. To dope or not to dope: The effect of sonicating single-wall carbon nanotubes in common laboratory solvents on their electronic structure. J. Am. Chem. Soc. 2008; 130(40):13417–24.

[51] Qian, R., Yu, J., Wu, C., Zhai, X., Jiang, P. Alumina-coated graphene sheet hybrids for electrically insulating polymer composites with high thermal conductivity. Rsc Adv. 2013; 3(38):17373–9.

CHAPTER 4: Chlorine-doped TiO_2/graphene nanocomposites for improving visible-light photocatalytic activity

Abstract

TiO_2/graphene nanocomposites have increasingly attracted an attention due to their high visible-light photocatalytic efficiency in the photodecomposition of organic pollutants. In Chapter 2, it was established that a novel GO-free technique to synthesize the TiO_2/graphene nanocomposites with an excellent visible-light photocatalytic activity. In this Chapter, I introduced a preparation of the chlorine-doped TiO_2/graphene nanocomposites using the chemical exfoliation of graphite in titanium tetra-*n*-butoxide and subsequently by a sol-gel reaction in the presence of chlorine organic compounds. With the aid of chlorine radicals, which accelerate the photodecomposition of target organic compound and a significant reduction of the amount of defects on the graphene framework, the chlorine-doped TiO_2/graphene nanocomposites exhibited a significant improvement photocatalytic performance compared to that of the undoped TiO_2/graphene nanocomposite.

4.1. Introduction

Recently, photocatalysts have attracted a great attention in terms of decomposition of the environmental pollutants in water, air, and soil [1–3]. During the past decades, many remarkable efforts have been made in the fabrication of new photocatalysts which work in the UV or visible-light region, and TiO_2-based photocatalysts have been considered as one of the most excellent candidates for solving environmental concerns due to its desirable properties [4–6]. However, its large band gap limits the utilization efficiency of solar energy, and the short lifetime of photo-excited electron-hole pair restrains its applicable catalytic efficiency. Enormous efforts have been devoted to alleviate these shortfalls including implanting with foreign metal ions or non-metals [7–12], tailoring heterojunction with other semiconductors [13–15], and noble metals [16–18], or grafting with organic chelating ligands [19–21]. Among them, hybridization of TiO_2 with graphene is a promising solution [22–26].

In recent years, many attempts on the synthesis of TiO_2/graphene nanocomposites using graphene oxide (GO) as a starting material have been reported. However, a nonuniform and uncontrolled growth of TiO_2 on graphene [27] as well as high density of defects in the reduced GO framework [28–30] are the challenges of the GO-based method. In Chapter 2, a novel GO-free route for the synthesis of TiO_2/graphene nanocomposites has been established, which involved the preparation of graphene dispersion in titanium alkoxide by exfoliating graphite, followed by a sol-gel reaction to achieve the TiO_2/graphene nanocomposites. The obtained TiO_2/graphene nanocomposites exhibited an excellent visible-light photocatalytic performance in the degradation of MB compared to that of a commercially available TiO_2 catalyst, TiO_2-P25, and the conventional TiO_2/rGO

nanocomposite [22]. Further enhancement of the visible-light photocatalytic activity of the TiO_2/graphene nanocomposites is the next challenge.

The essential factors affect the visible-light photocatalytic performance of the TiO_2/graphene nanocomposites need to be considered in order to further improve their photocatalytic activity. For example, the following characteristics are important as essential factors: the enhancement in adsorption capacity, the visible-light utilization efficiency by the extension of optical absorption, electron-hole separation or the generation of highly active species to accelerate the photodecomposition of the target organic compounds. Back to the modification of TiO_2, most recently, halogen have drawn great interests as promising dopants for TiO_2 for the improvement in the visible-light photocatalytic activity. It has been reported that halogen doping can enhance surface properties of TiO_2 by adjusting the chemical compositions, surface acidity, and surface area, improving the charge transfer process on the catalyst surface [31]. Another important benefit was that the optical absorption of the TiO_2 photocatalysts was extended into the visible-light region when doping with halogen [31] which includes fluorine [32–35], chlorine [36–39], and iodine doping [40–42]. In fact, fluorine was firstly utilized as a dopant for the improvement of the UV light photocatalytic activity of TiO_2 and then the investigation expanded to the development of the activity in the visible light. It was found that fluorine would affect the photocatalytic reaction by changing the surface charge distribution, surface-substrate interaction, and the interfacial electron-hole transfer, attributing to the improvement in surface acidity, hydroxyl radicals formation, and the generation of oxygen vacancies [35]. Further studies revealed that halogen doping could modify the position of the valence band (VB) and the conduction band (CB) of TiO_2 photocatalysts to extend the intrinsic absorption edge to the visible-light area [39–41]. In addition, the high electron-withdrawing capability of halogen also decreased the recombination of photo-induced electrons and holes. Thus,

the halogen doping can produce many ways to control the optical property and electronic structure, consequently reading to the improvement in the photocatalytic activity of TiO_2 [42], and hence it should give rise a positive influence on the performance of TiO_2/graphene nanocomposite catalysts.

This chapter represents my efforts to further improve the visible-light photocatalytic activity of the TiO_2/graphene nanocomposites by introducing chlorine element. The chlorine-doped TiO_2/graphene nanocomposites were synthesized based on the chemical exfoliation of graphite in titanium tetra-*n*-butoxide and subsequently the sol-gel reaction in the presence of chlorine organic compounds as catalysts or co-catalysts. A significant improvement in the visible-light photocatalytic activity in the photodecomposition of methylene blue, naphthalene and phenol in aqueous media were achieved in the chlorine-doped TiO_2/graphene nanocomposites compared to the undoped nanocomposite. This enhancement was attributed not only to the already reported basic phenomena in halogen doping to TiO_2, but also to the support of chlorine radicals to accelerate the photodecomposition process as well as a significant minimization of the defect amount on the graphene framework.

4.2. Materials and methods

4.2.1. Materials

Graphite powder (≥ 98%, 45 μm), benzylamine (> 98%), and 1,2-dichlorobenzene (ODCB, > 98%) were obtained from Wako Pure Chemical Industries, 2-chlorobenzylamine (> 97%) from ACROS Organic, aqueous ammonia solution (NH_3) (28–30%) from Kanto Chemical, and titanium tetra-*n*-butoxide ($Ti(OnBu)_4$, ≥ 97%) from Sigma Aldrich. Hydrochloric acid (HCl) (35–37%) was obtained from Wako Pure Chemical Industries. A commercial photocatalyst, TiO_2-P25 (Sigma Aldrich) with the primary crystallite size of 21

nm was utilized after calcination at 400 °C for 2 h under nitrogen as a reference sample. Acetone and hexane (Kanto Chemical) were used after being dried over molecular sieves 4A under nitrogen bubbling. Ethyl alcohol (Kanto Chemical) were also used as a solvent for washing. Methylene blue (MB) (≥ 98.5%) was obtained from Kanto Chemical, which was used as a dye for the photocatalytic test. Phenol from Wako Pure Chemical, naphthalene from Sigma Aldrich (≥ 99%) were as aromatic and polyaromatic compound for the photocatalytic test. Acetonitrile (≥ 99.8%) purchased from Wako was used as a solvent for the preparation of the stock solution of naphthalene. GO was synthesized from graphite powder using the modified Hummers method [43] and it was utilized as a graphene source in the preparation of a conventional TiO_2/reduced graphene oxide.

4.2.2. Synthesis of graphene dispersion in Ti(OnBu)$_4$

As a starting material of the catalysts, graphene dispersion in Ti(O*n*Bu)$_4$ was prepared from graphite by a chemical exfoliation method. Briefly, 44.0 mg of graphite was sonicated in 5.5 mL of Ti(O*n*Bu)$_4$ at 43 kHz and 60 °C for 4 h under a N_2 atmosphere. The resultant black mixture was centrifuged at 3000 rpm for 4 h in order to precipitate non-exfoliated graphite. Finally, the graphene dispersion in Ti(O*n*Bu)$_4$ was obtained as the supernatant and denoted as graphene/Ti(O*n*Bu)$_4$.

4.2.3. Synthesis of chlorine-doped graphene dispersion in Ti(OnBu)$_4$

The chlorine-doped graphene dispersion was prepared by the impregnation following by the chemical exfoliation. In brief, 500 mg of graphite was added into 20 mL of HCl and stirred at 70 °C for 8 h. The mixture was then washed with DI water for several times until the pH of the supernatant was neutral. The remaining black solid was fully dried under vacuum at 70 °C for 12 h to obtain the chlorine-doped graphite, which was denoted as Cl-

graphite. Similar to the preparation of the graphene dispersion in Ti(O*n*Bu)$_4$, 44.0 mg of Cl-graphite was sonicated in 5.5 mL of Ti(O*n*Bu)$_4$ for 4 h under N_2 atmosphere. The black mixture was centrifuged at 3000 rpm for 4 h to precipitate non-exfoliated graphite and denoted as Cl-graphene/Ti(O*n*Bu)$_4$. The graphene concentration of the supernatant was evaluated based on the absorbance at 550 nm (JASCO V-670 UV-Vis spectrometer). The measured absorbance was referenced to a calibration curve that was externally acquired using GNP dispersions.

4.2.4. Fabrication of chlorine-doped TiO_2/graphene nanocomposites using sol-gel method

The chlorine-doped TiO_2/graphene nanocomposites were fabricated from graphene/Ti(O*n*Bu)$_4$ based on sol-gel method in the presence of a chlorine organic compounds. 2-chlorobenzylamine and ODCB were chosen as chlorine sources. ODCB was used as a mixture with benzylamine (v/v = 1: 1) because benzylamine is important to obtain performant catalysts in terms of the extension of the absorption edge as well as an excellent photocatalytic activity of the TiO_2/graphene nanocomposites which was identified in Chapter 2. Three types of TiO_2/graphene catalysts were synthesized with varying the catalysts (H_2O or NH_3) and chlorine sources (2-chlorobenzylamine or ODCB) to explorer a better performant chlorine-doped catalyst. Firstly, aqueous (*aq.*) NH_3 or H_2O and a chlorine source (2-chlorobenzylamine or ODCB/benzylamine mixture) were mixed at a volume ratio of 1:8 (total 5.0 mL), and then the mixture was added dropwise into 5.0 mL of the graphene/Ti(O*n*Bu)$_4$ with vigorous magnetic stirring under a N_2 atmosphere. A grayish gel obtained after 2 h of the reaction at room temperature was washed subsequently with anhydrous hexane and acetone for three times before being fully dried in vacuum at 70 °C for 12 h. Thus, obtained catalysts were termed as TG-NH_3/8ClBA, TG-H_2O/8ClBA, and

TG-NH_3/8(ODCB, BA). For comparison, another chlorine-doped TiO_2/graphene nanocomposite was also prepared via a different route. The Cl-graphene/Ti(O*n*Bu)$_4$ instead of graphene/Ti(O*n*Bu)$_4$ was used in the similar procedure using the mixture of *aq.* NH_3 and benzylamine (v/v = 1:3) as a catalyst for the sol-gel reaction. The obtained nanocomposite was denoted as Cl-TG-NH_3/3BA. In addition, the undoped TiO_2/graphene nanocomposite was also prepared by the similar procedure using graphene/Ti(O*n*Bu)$_4$ as a starting material and the mixture of *aq.* NH_3 and benzylamine as a catalyst for the sol-gel reaction. All of the synthetic conditions for the preparation of the chlorine-doped TiO_2/graphene nanocomposites are summarized in Table 4.1. Due to a significantly low solubility in water of the chlorine organic compounds, the volume ratio between H_2O, *aq.* NH_3 solution and chlorine organic compounds was smaller compared to that between *aq.* NH_3 solution and benzylamine.

Table 4.1. Synthetic conditions for chlorine-doped TiO_2/graphene nanocomposites.

Sample	Catalyst for the sol-gel reaction[a]
TG-NH_3/8ClBA	*aq.* NH_3/ClBA (1/8 v/v)
TG-H_2O/8ClBA	*aq.* H_2O/ClBA (1/8 v/v)
TG-NH_3/8(ODCB, BA)[b]	*aq.* NH_3/ODCB and BA (1/8 v/v)
TG-NH_3/3BA[c]	*aq.* NH_3/BA (1/3 v/v)
Cl-TG-NH_3/3BA[d]	*aq.* NH_3/BA (1/3 v/v)

[a] Benzylamine and 2-chlorobenzylamine are abbreviated as BA and ClBA, respectively.
[b] Catalyst is the mixture of ODCB and benzylamine with volume ratio of 1:1.
[c]The TiO_2/graphene nanocomposite was prepared by the sol-gel reaction of the graphene/Ti(O*n*Bu)$_4$ and the mixture of *aq.* NH_3 and benzylamine (v/v = 1:3).
[d] The chlorine-doped TiO_2/graphene nanocomposite was prepared from Cl-graphene/Ti(O*n*Bu)$_4$.

4.2.5. Preparation of TiO_2/rGO

For comparison purpose, a TiO_2/rGO nanocomposite was also prepared by the procedure reported by Jiang et al. [44]: 1.0 mg of GO was dispersed in 36.7 mL of methanol under ultrasonication at room temperature for 30 minutes. 5.7 mL of Ti(O*n*Bu)$_4$ was then

dropwise added into the dispersion under a N_2 atmosphere and vigorously stirred for 1 h. The mixture was transferred into a Teflon-lined autoclave (100 mL) prior to a solvothermal process at 180 °C for 24 h, followed by natural cooling to room temperature. After thorough washing by ethanol and DI water for three times alternately and subsequently drying in vacuum at for 12 h 80 °C, the product was calcined at 400 °C for 2 h under nitrogen. The produced nanocomposite is denoted as TiO_2/rGO.

4.2.6. Characterizations

The morphology of the nanocomposites was examined using a transmission electron microscope (TEM) (H-7100, HITACHI) operated at a voltage of 100 kV. A sample was dispersed in methanol, then casted onto a carbon-coated copper grid and dried overnight at room temperature prior to the measurements. The Raman spectra of the nanocomposites were measured on a Laser Raman spectrometer (NRS-4100, JASCO) with a 532 nm laser. The dried powder samples were placed on a glass slide. The Raman measurement was conducted with the slit of 10 x 8000 μm and the exposure time of 80 s and 50 accumulations. In the Raman active modes of TiO_2, the E_g bands are characterized to the symmetric vibration of O–Ti–O bonds, while the B_{1g} and A_{1g} bands are related to the symmetric and asymmetric bending vibration of O–Ti–O [45–47]. For graphene modes, the G band is originated from the in-plane vibration of sp^2 carbon atoms [48], whereas the D band indicates the existence of defects on the graphene [48,49]. In order to estimate the relative concentration of defects compared to the sp^2 hybridized graphene domain, the intensity ratio of the D and G bands (I_D/I_G) is evaluated. X-ray diffraction (XRD) patterns were acquired in a reflection geometry on a Rigaku Smartlab X-ray diffractometer using a Cu Kα radiation (1.542 Å) at a voltage of 40 kV and a current of 30 mA. The measurements

were performed at room temperature in the range of 2θ of 10–80º with a scan speed of 0.3º min^{-1}.

UV-visible (UV-Vis) spectra were recorded in the transmittance mode to evaluate the MB concentration in photocatalysis and in the diffuse reflectance (DRS) mode for the powder samples using a UV-Vis spectrometer (V770, JASCO). The fine powder samples were loaded into a quartz cell with a 2 mm path length. The measurements were conducted in the range of 300–800 nm at a scanning rate of 100 nm min^{-1} and at the resolution of 2 nm, in which a $BaSO_4$ plate was utilized as the background.

The chlorine contained was evaluated by X-ray Photoelectron Spectroscopy (XPS) analysis which was carried out on a Shimadzu Kratos AXIS-ULTRA DLD high performance XPS system operating at 150 W and vacuum level of 1 x 10^{-8} Torr. Photoelectrons were excited by monochromated Al Kα radiation and detected with a delay-line detector (DLD) and a concentric hemispherical analyzer (CHA). The pass energy of the CHA was 160 eV for the survey scan and 20 eV for narrow-scan spectra. For each element, a narrow scan was swept in 240 s and repeated 3 times. An analyzed area was 300 x 700 μm^2 on the specimen surface and located in the center of the irradiation. A fine powder sample was stacked on a copper substrate. The stage position was adjusted to achieve the best intensity for C 1s for each sample and to avoid a signal from the substrate (e.g. Cu 2p)

4.2.7. Photocatalytic test

4.2.7.1 Photodegradation of methylene blue

The photocatalytic activity of the nanocomposites was investigated preliminarily by the photodegradation of methylene blue. A specified amount of the catalyst powder was suspended in 25 mL of aqueous solution of MB at 50 mg L^{-1} and kept in dark under a constant stirring for 12 h to ensure the adsorption/desorption equilibrium. 2.0 mL of the

suspension was then extracted in order to determine the initial concentration of MB in the reaction medium. The rest of the suspension was irradiated for 6 h under the visible light at room temperature. The light source was supplied by a light irradiator (MAX-303, Asahi spectra) using a 300 W xenon short arc lamp and a 422-nm longpass filter. A guide light rod unit (LG series, Asahi spectra) was inserted into the suspension at the location of 4 cm away from the reactor bottom. The photocatalytic activity of a catalyst was evaluated through the amount of MB degraded per one gram of the catalyst per hour. The activity was recorded as an average of at least three photocatalytic tests per sample.

4.2.7.2 Photodecomposition of naphthalene

The photocatalytic activity of the catalysts was further examined by the photodecomposition of naphthalene in aqueous media. Briefly, a specific amount of the catalyst was added in 20 mL of the solution of 25 ppm of naphthalene prepared in the mixture of DI water and acetonitrile (v/v = 1:1) and kept stirring in dark for 6 h to achive the adsorption and desorption equilibrium. The suspension was irradiated for 4 h under the visible light at room temperature under an O_2 atmosphere at 0.1 MPa using light irradiator (MAX-303, Asahi spectra) with a 300 W xenon short arc lamp and a 422-nm longpass filter. The concentration of the naphthalene was determined by gas chromatography (GC) using benzyl alcohol as an internal standard. The conditions for GC are presented in Table 4.2. The photocatalytic activity was calculated by the amount of naphthalene decomposed per one gram of the catalyst per hour with the average of three tests per sample.

4.2.7.3 Photodecomposition of phenol

The photodecomposition of phenol in aqueous media was conducted also to evaluate the catalytic ability of the samples. In brief, a specific amount of the catalyst was added into

20 mL of aqueous solution of phenol 100 ppm under stirring and kept in dark for 6 h to achieve the adsorption/desorption equilibrium. The suspension was then purged with pure O_2 for 10 minutes and irradiated for 4 h under visible light at 0.1 MPa. Similarly, the photocatalytic activity was recorded as the amount of phenol being decomposed per gram catalyst per hour.

Table 4.2. Measurement conditions for GC

Parameters	Details
Column	DB-FATWAX
Inject volume	1 μL
Injection mode	Spitless for NAP and split ratio of 5:1 for others
Carrier gas	N_2 with flow rate of 25 mL/min
Detector	FID, temp = 300 ℃

4.3. Results and discussion

4.3.1. Preparation of chlorine-doped TiO_2/graphene nanocomposites

Figure 4.1 compares the TEM images of the TiO_2/graphene nanocomposites with and without chlorine doping. Uniform sheet-like structures are presented in all of the chlorine-doped and undoped TiO_2/graphene nanocomposites. It can be considered that the isolated graphene sheets are uniformly and thinly covered by TiO_2 nanolayers, which is promising for an effective charge carrier separation. Figure 4.2 presents Raman spectra of the chlorine-doped and undoped TiO_2/graphene nanocomposites. Compared to the undoped TiO_2/graphene (TG-NH_3/3BA), the chlorine-doped samples showed different TiO_2 modes. Beside the peaks of TiO_2 anatase at 397 [B_{1g}], 516 [A_{1g} + B_{1g}], and 638 cm^{-1} [E_g], there was a peak appeared at 241 cm^{-1} in all chlorine-doped TiO_2/graphene samples, which was attributed to the second-order scattering (E_g) peak of rutile. In addition, the E_g peaks of anatase at 144 and 197 cm^{-1} were also disappeared in the case of chlorine-doped

TiO_2/graphene samples. Thus, different from the undoped TiO_2/graphene nanocomposite, the chlorine-doped TiO_2/graphene nanocomposites contained TiO_2 with the combination of anatase and rutile forms. For graphene modes, it can be observed that in the presence of chlorine significantly decreased the I_D/I_G, except in the case of using ODCB, which suggested the decrease of defects on the graphene framework. The most significant difference between TG-NH_3/3BA and Cl-TG-NH_3/3BA was the starting materials. TG-NH_3/3BA was synthesized using graphene/Ti(O*n*Bu)$_4$ while Cl-TG-NH_3/3BA was prepared from Cl-graphene/Ti(O*n*Bu)$_4$. It has been found that Brønsted acids can be intercalants and thus, expand the interlayer distance of graphite [50]. The intercalated graphite can be obtained during the impregnation process with HCl at 70 ℃, which was able to accelerate the exfoliation process. As a result, an improvement in graphene yield was achieved. As a matter of fact, the graphene concentration in Cl-graphene/Ti(O*n*Bu)$_4$ was 0.4 mg mL^{-1}, which was higher than that in graphene/Ti(O*n*Bu)$_4$, 0.3 mg mL^{-1}. This high efficiency of graphene exfoliation probably led to a smaller number of defects in graphene framework. On the other hand, this reduction was also observed in TG-NH_3/8ClBA and TG-H_2O/8ClBA nanocomposites, which can be attributed to the effectiveness of 2-chlorobenzylamine in stabilizing graphene sheets during the sol-gel process. The difference between TG-NH_3/3BA and TG-NH_3/8ClBA or TG-H_2O/8ClBA was the catalyst utilized in the sol-gel reaction. It is known that ideal solvents to stabilize graphene are those which can minimize the interfacial tension between solvent and graphene flakes [51–53]. In another ways, solvents with surface tension $\sigma \approx 40$ mJ m^{-2}, comparable to that of graphene, are the most suitable to stably disperse graphene [54]. Both benzylamine (σ = 38.82 mJ m^{-2}) [55] and 2-chlorobenzylamine (σ = 42.0 mJ m^{-2}) [56] with surface tension matching exhibited ability to stabilize graphene, which was found in Chapter 3. However, 2-chlorobenzylamine might present a better performance in stabilization due to the synergistic effect among

aromatic, amine, and halogen functional groups. However, a similar result was not obtained in TG-NH_3/8(ODCB, BA). It can be considered that the usage of combination of benzylamine and ODCB did not show any change compared to that of benzylamine itself.

Figure 4.3 plots XRD patterns of the chlorine-doped and undoped TiO_2/graphene nanocomposites. Only three broad diffraction peaks of TiO_2 anatase at 27.8º, 47.1º, and 62.5º was observed, which indicate the formation of nano-sized TiO_2 crystals. The absence of graphite diffraction peaks also evidenced the sufficient exfoliation or formation of graphene.

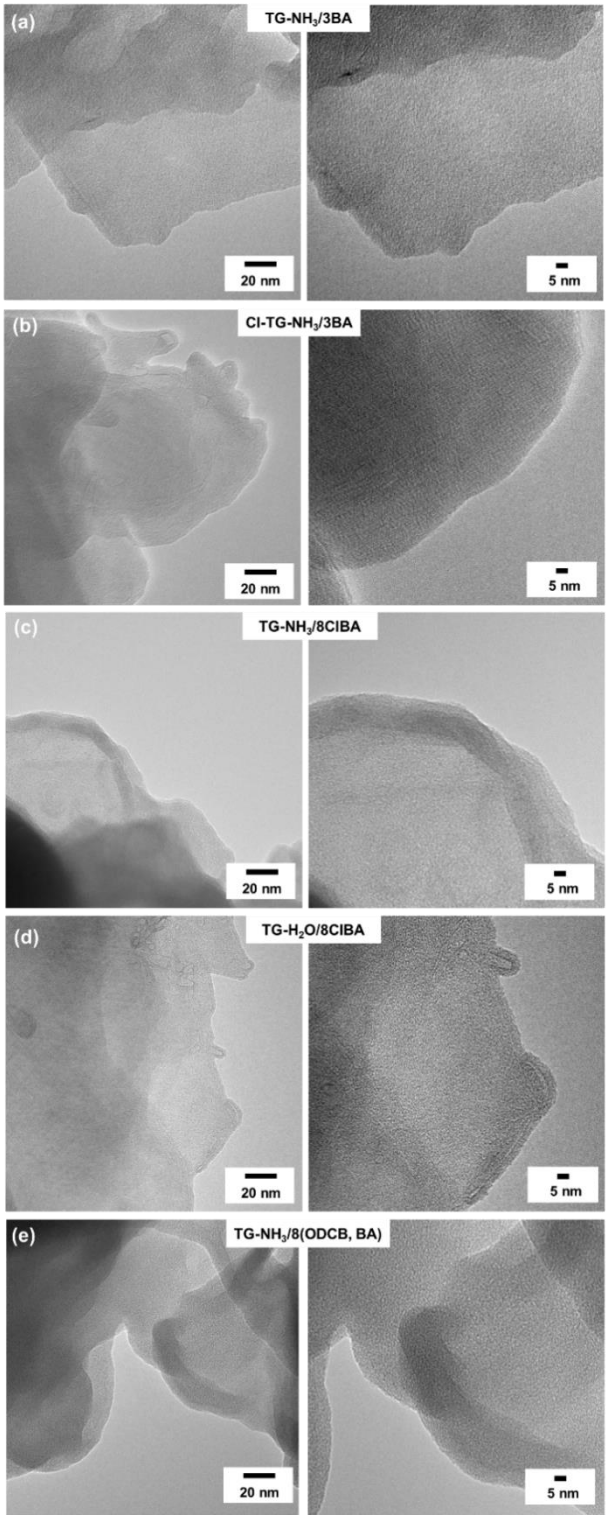

Figure 4.1. TEM images of a) TG-NH_3/3BA b) Cl-TG-NH_3/3BA, c) TG-NH_3/8ClBA, d) TG-H_2O/8ClBA, e) TG-NH_3/8(ODCB, BA) nanocomposites.

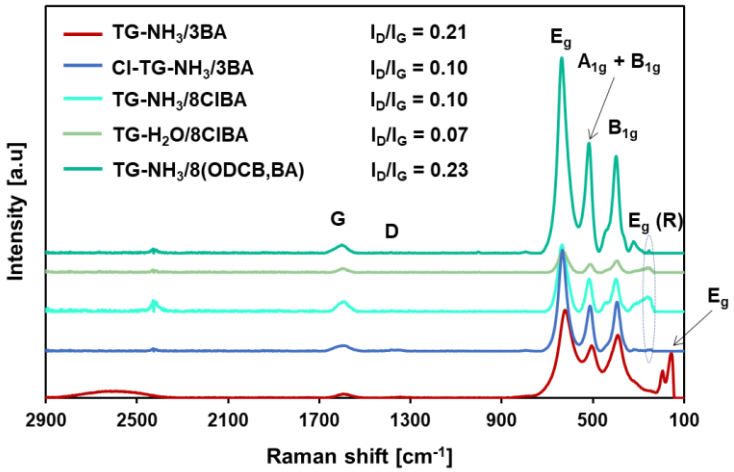

Figure 4.2. Raman spectra of the chlorine-doped and undoped TiO_2/graphene nanocomposites.

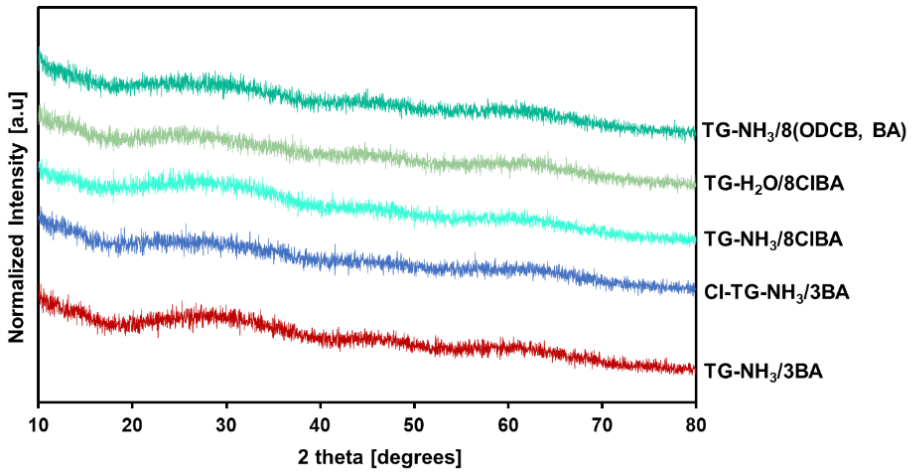

Figure 4.3. XRD patterns of the chlorine-doped and undoped TiO_2/graphene nanocomposites

In order to investigate the optical absorption feature of the chlorine-doped TiO_2/graphene nanocomposites, the UV-Vis DRS spectra were acquired (Figure 4.4). TG-NH_3/3BA showed a larger background absorption in the visible-light area compared to the other samples, which was attributed to the incorporation of graphene into the TiO_2 matrix [57]. The absorption edge is recorded as the intercept of a linear part of absorption spectra

and a linear part of the background absorption. The absorption edges of TG-NH_3/3BA, Cl-TG-NH_3/3BA, TG-H_2O/8ClBA, TG-NH_3/8ClBA, and TG-NH_3/8(ODCB, BA) were 578, 440, 540, 574, and 461 nm, respectively. Each sample showed a remarkable extension compared to the nano-sized TiO_2 anatase (360 nm) [58]. Among the chlorine-doped TiO_2/graphene nanocomposites, Cl-TG-NH_3/3BA and TG-NH_3/8(ODCB, BA) showed a smaller extension of the absorption edge, which may reduce the light utilization efficiency compared to others.

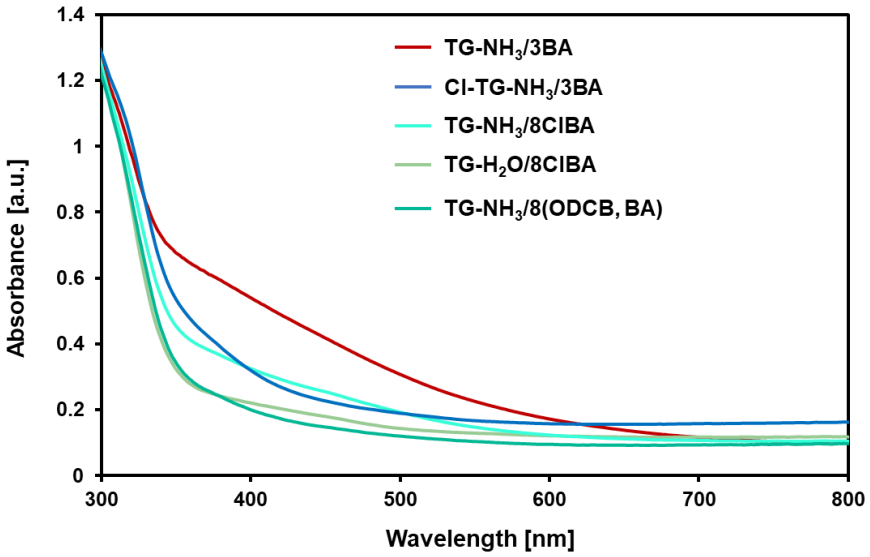

Figure 4.4 UV-Vis DRS spectra of chlorine-doped and undoped TiO_2/graphene nanocomposites prepared in different conditions.

4.3.2. Photocatalytic test

The photocatalytic activities of the catalysts were examined by the decomposition of MB under the visible-light irradiation. At first, the adsorption abilities of the catalysts were evaluated by the adsorption of MB in dark for 12 h. Figure 4.5a compares the adsorption ability of the catalysts. Compared to TiO_2-P25 and TiO_2/rGO nanocomposite, the TiO_2/graphene nanocomposites exhibited by far the better adsorption abilities. In addition,

the chlorine-doped TiO_2/graphene showed 1.2–1.5 times higher in adsorption ability compared to that of the undoped TiO_2/graphene nanocomposite. In order to normalize the difference in the MB adsorption capacity, the amount of the catalysts was adjusted to unify the initial concentration of MB before irradiation which is shown in Table 4.3. After achieving the equilibration in dark, the visible light was irradiated under constant stirring at room temperature. Firstly, the activities of the catalysts were quantified by the MB degradation per gram catalyst per hour (Figure 4.5b). Compared to TG-NH_3/3BA, the chlorine-doped TiO_2/graphene nanocomposites exhibited higher activity. Especially, the TG-NH_3/8ClBA and TG-H_2O/8ClBA presented the highest photocatalytic activity (2.4 times higher than that of the TiO_2/graphene nanocomposite). Next, the photocatalytic was then compared based on the adsorption amount (Figure 4.5c). It can be observed that the TG-NH_3/8ClBA exhibited the highest activity, which was 2.4 times higher in compared to that of TiO_2/rGO nanocomposite and 1.8 times greater in compared to TG-NH_3/3BA.

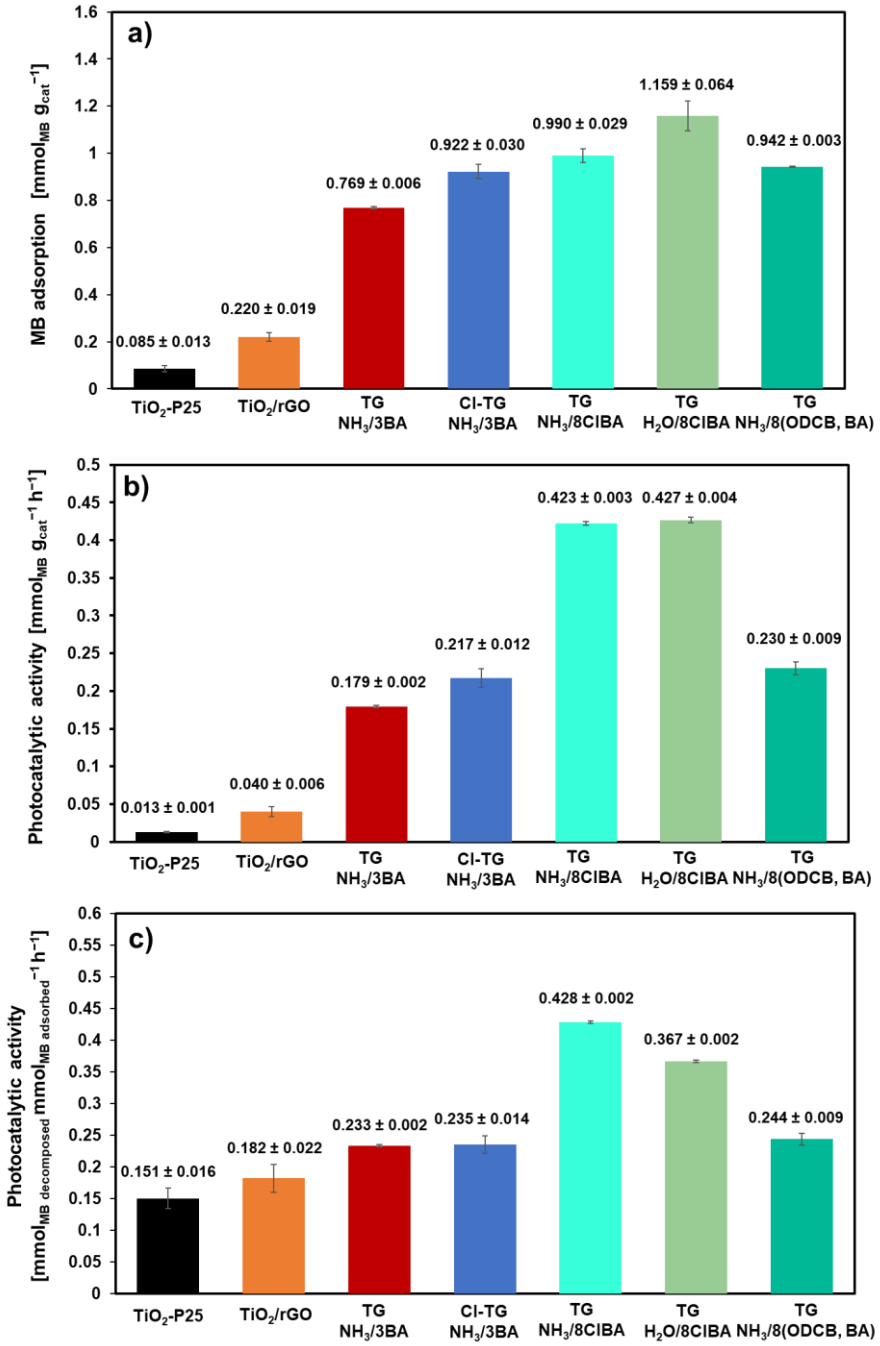

Figure 4.5. a) Equilibrium adsorption of MB on the photocatalysts. 3.0 mg of a sample was placed in a 50 mg/mL aqueous solution of MB in dark for 12 h under constant stirring. The amount of the adsorption was derived by measuring the MB concentration in the supernatant after 12 h. b) Photocatalytic activity per gram catalyst. The activities were evaluated from the loss of the MB concentration after 6 h irradiation. c) Photocatalytic

activity per MB adsorption. The activity per gram catalyst in b) was divided by the MB adsorption capacity per gram catalyst in a).

Table 4.3 Adjusted catalyst amount for the photodegradation of methylene blue

Catalyst	Catalyst amount (mg)
TiO_2-P25	7.74
TiO_2/rGO	3.00
TG-NH_3/3BA	0.86
Cl-TG-NH_3/3BA	0.72
TG-NH_3/8ClBA	0.67
TG-H_2O/8ClBA	0.57
TG-NH_3/8(ODCB, BA)	0.70

The study about the active species in the TiO_2/graphene nanocomposites in Chapter 2 investigated the significant role of superoxide radicals on the excellent photocatalytic activity of the TiO_2/graphene nanocomposites, in other words, it implied the ability of the nanocomposites to activate molecular oxygen. Based on that fact, the photocatalytic activity of the chlorine-doped TiO_2/graphene nanocomposites were examined by the photodecomposition of obstinate polyaromatic and aromatic compounds (naphthalene and phenol) under an O_2 atmosphere. Figure 4.6a presents the naphthalene adsorption ability of the catalysts. Obviously, the TiO_2/graphene nanocomposites showed higher adsorption capacity compared to that of TiO_2-P25 and TiO_2/rGO nanocomposite. Among TiO_2/graphene nanocomposites, further improvement in adsorption capacity was achieved for the chlorine-doped nanocomposites, especially in the TG-NH_3/8ClBA and TG-H_2O/8ClBA nanocomposite. Table 4.4 shows the amount of the catalysts, which was adjusted to unify the initial concentration of naphthalene before irradiation (after 6 h in dark). After obtaining the equilibration in dark, the visible light was irradiated under a constant stirring at room temperature. The activities of the catalysts were quantified by the naphthalene decomposition per gram catalyst per hour (Figure 4.6b). Obviously, under an

O_2 atmosphere, the TiO_2/graphene nanocomposites presented excellent catalytic activity compared to TiO_2-P25 and TiO_2/rGO, which can be observed in the order of TiO_2-P25 < TiO_2/rGO << [TG-NH_3/3BA < TG-NH_3/8(ODCB, BA) ≈ Cl-TG-NH_3/3BA << TG-H_2O/8ClBA < TG-NH_3/8ClBA]. Compared to TiO_2-P25 and TiO_2/rGO nanocomposite, TG-NH_3/3BA nanocomposite exhibited 16 and 4 times higher in the photocatalytic activity. Further improvement in the photocatalytic activity was obtained in the presence of chlorine, especially TG-NH_3/8ClBA and TG-H_2O/8ClBA exhibited the highest activity (0.0732 and 0.0728 mmol g_{cat}^{-1} h^{-1}), which were 2 times higher than that of TG-NH_3/3BA nanocomposite. While in the comparison per mmol of naphthalene adsorbed, TG-NH_3/8ClBA and TG-H_2O/8ClBA showed 1.2 and 1.4 times higher in the activity compared to that of TG-NH_3/3BA nanocomposite, respectively (Figure 4.6c).

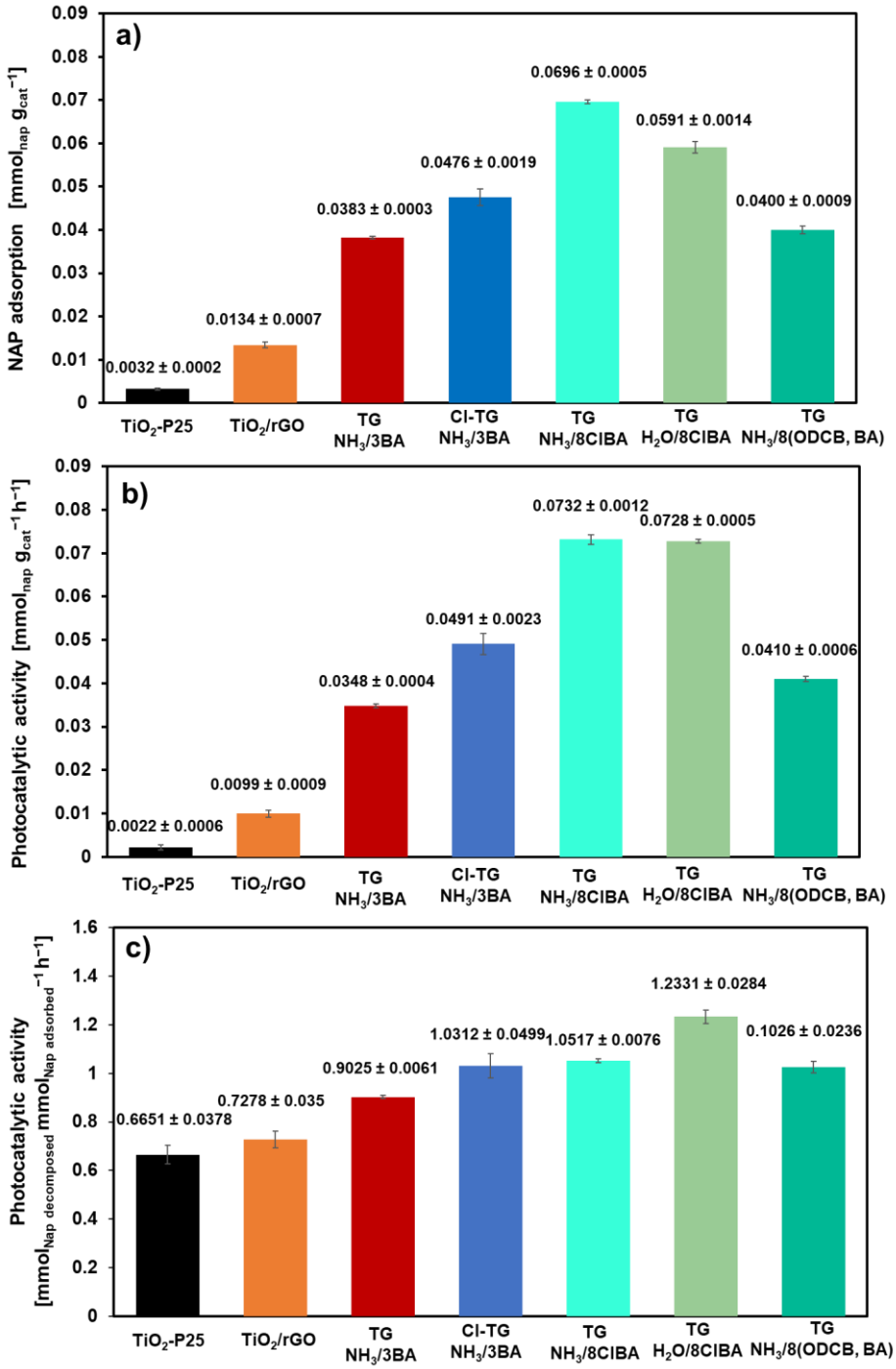

Figure 4.6. a) Equilibrium adsorption of naphthalene on the photocatalysts. 20.0 mg of a sample was placed in 20 mL of naphthalene solution (25 mg/mL) in dark for 6 h under constant stirring. The amount of the adsorption was derived by measuring the naphthalene concentration in the supernatant after 6 h. b) Photocatalytic activity per gram catalyst. The adjusted amount of the catalysts is presented in Table 4.4. The activities were evaluated

from the loss of the naphthalene concentration after 4 h irradiation. c) Photocatalytic activity per naphthalene adsorption. The activity per gram catalyst in b) was divided by the naphthalene adsorption capacity per gram catalyst in a).

Table 4.4 Adjusted catalyst amount for the photodegradation of naphthalene

Catalyst	Catalyst amount (mg)
TiO_2-P25	82.62
TiO_2/rGO	20.00
TG-NH_3/3BA	7.00
Cl-TG-NH_3/3BA	5.62
TG-NH_3/8ClBA	3.84
TG-H_2O/8ClBA	4.53
TG-NH_3/8(ODCB, BA)	6.69

The visible-light photocatalytic activity of the TiO_2/graphene nanocomposites was also evaluated by the decomposition of phenol in an O_2 atmosphere. Figure 4.7a displays the adsorption capacity of the photocatalysts, which was recorded after 6 h stirring in dark. It is clear that the TiO_2/graphene nanocomposites presented an excellent adsorption capacity compared to that of TiO_2-P25 and TiO_2/rGO nanocomposite and the chlorine-doped TiO_2/graphene nanocomposites therein exhibited further enhancement compared to the undoped nanocomposite. The photocatalytic activity is shown in Figure 4.7b. Similar to the results for MG and naphthalene decomposition, the TiO_2/graphene nanocomposites demonstrated the excellent photocatalytic performance. Among the results of the TiO_2/graphene nanocomposites, it can be seen that further improvement was observed in the presence of chlorine and especially the TG-NH_3/8ClBA and TG-H_2O/8ClBA nanocomposites showed the highest enhancement in photocatalytic activity. TG-NH_3/8ClBA nanocomposite presented 2.6 times higher in the activity compared to that of TG-NH_3/3BA nanocomposite, while 2.2 times greater improvement was found in the case

of TG-H_2O/8ClBA nanocomposite. In comparison per mmol of phenol adsorption, TG-NH_3/8ClBA and TG-H_2O/8ClBA nanocomposites presented 1.6 and 1.5 times higher in activity compared to TG-NH_3/3BA nanocomposite (Figure 4.7c).

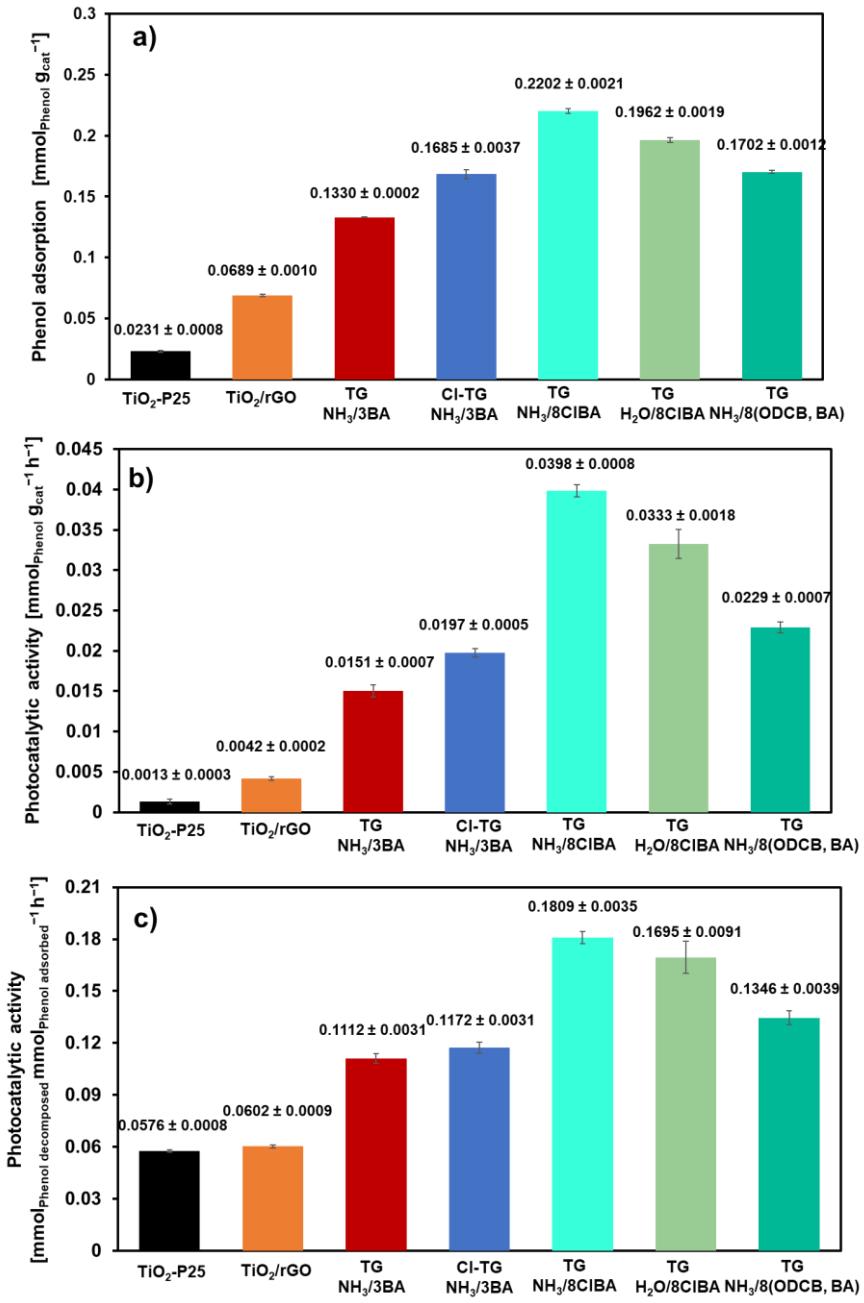

Figure 4.7. a) Equilibrium adsorption of phenol on the photocatalysts. 100.0 mg of a sample was placed in 20 mL of phenol solution (100 mg/mL) in dark for 6 h under constant stirring.

The amount of the adsorption was derived by measuring the phenol concentration in the supernatant after 6 h. b) Photocatalytic activity per gram catalyst. The activities were evaluated from the loss of the phenol concentration after 4 h irradiation. The amount of the catalysts was adjusted to unify the initial concentration of phenol before irradiation, summarized in Table 4.5. c) Photocatalytic activity per phenol adsorption. The activity per gram catalyst in b) was divided by the phenol adsorption capacity per gram catalyst in a).

Table 4.5. Adjusted catalyst amount for the photodegradation of phenol

Catalyst	Catalyst amount (mg)
TiO_2-P25	298.84
TiO_2/rGO	100.00
TG-NH_3/3BA	51.78
Cl-TG-NH_3/3BA	31.29
TG-NH_3/8ClBA	35.11
TG-H_2O/8ClBA	40.48
TG-NH_3/8(ODCB, BA)	40.89

The three decomposition tests showed that the TiO_2/graphene nanocomposites, especially the chlorine-doped ones, exhibited an excellent visible-light photocatalytic activity compared to TiO_2-P25 and TiO_2/rGO nanocomposite (30 times and 6 times higher in activity, respectively); while in literatures, only 4–7 times improvement in the visible-light photocatalytic performance was found in chlorine-doped TiO_2 compared to that of TiO_2-P25 [36,37,39]. As concluded in Chapter 2, a large portion of the activity improvement (*ca.* 70 %) was attributed to the superb adsorption capacity benefited from the special morphologies of the TiO_2/graphene nanocomposites. On the contrary, in the case of the chlorine-doped TiO_2/graphene nanocomposites, the activity of TG-NH_3/8ClBA was 2–2.6 times higher than that of TG-NH_3/3BA on the comparison per gram of the catalyst, while the improvement in the organic compounds adsorption was 1.2–1.6 times, and hence only around 40 % of the catalytic enhancement was attributed to the improvement in the

adsorption capacity. Thus, there would be another factor contributing to the improvement in the visible-light photocatalytic performance of the chlorine-doped TiO_2/graphene nanocomposites. The order of the photocatalytic activity was TG-NH_3/8ClBA ≈ TG-H_2O/8ClBA >> Cl-TG-NH_3/3BA ≈ TG-NH_3/8(ODCB, BA) > TG-NH_3/3BA nanocomposites. Several factors for the photocatalytic improvement were examined. At first, the effect of their optical property was considered. In comparison between chlorine-doped and undoped nanocomposites, even Cl-TG-NH_3/3BA and TG-NH_3/8(ODCB, BA) nanocomposites presented the lower absorption edge extension than TG-NH_3/3BA nanocomposite, whereas they both exhibited better catalytic activity compared to that of TG-NH_3/3BA nanocomposite. On the other hand, among the chlorine-doped TiO_2/graphene nanocomposites, the catalysts which showed a lower absorption edge extension (Cl-TG-NH_3/3BA and TG-NH_3/8(ODCB, BA)) exhibited more or less lower photocatalytic activity. It is because the visible-light utilization efficiency of Cl-TG-NH_3/3BA and TG-NH_3/8(ODCB, BA) might be reduced compared to the other chlorine-doped catalysts. It can be concluded from the fact that the absorption edge extension must be important to improve the photocatalytic activity, but it is not exclusive factor. The role of the chlorine dopant was the next consideration. By XPS measurement, the amount of chlorine content in the TG-NH_3/8ClBA, TG-H_2O/8ClBA, Cl-TG-NH_3/3BA, and TG-NH_3/8(ODCB, BA) were determined as 0.96, 1.50, 0.10, and 2.03 wt%, respectively. It is possible that under visible-light irradiation, the chlorine radicals which are less energetic than hydroxyl radicals can be formed [59]. Chlorine radicals can attack organic substrates having weakly bound branch hydrogen and destruct them to smaller molecules by chain transfer oxidation. For aromatic and polyaromatic compounds, it is difficult to decompose them by chlorine radicals directly under the visible light, while the holes, hydroxyl radicals and especially superoxide radicals are more reactive for the cleavage of aromatic rings [60,61]. Thus, the existence of chlorine

radicals can further accelerate the overall photodecomposition reaction of the organic compounds. However, TG-NH_3/8(ODCB, BA) showed less activity improvement compared to others even though it had the highest chlorine content. Therefore, even though the existence of chlorine radicals was important to accelerate the photodecomposition of organic compounds, chlorine content was not the most important factor in the development of the photocatalytic activity of the chlorine-doped TiO_2/graphene nanocomposites. The final factor is the number of defects on the graphene framework. It is known that the photocatalytic decomposition of organic compounds was likely driven by the highly reactive radicals e.g. hydroxyl radicals, superoxide radicals, and etc., which were generated by photo-excited electrons injected into graphene. Thus, graphene quality, especially a less number of defects, was most likely correlated to the photocatalytic activity of the nanocomposites. In fact, it was reported that the electrical mobility of the nanocomposite can be increased by minimizing the number of defects [62]. This improvement can in turn enhance the transportation and separation of photogenerated charge carriers within graphene, resulting in the enhancement of the photocatalytic activity of the TiO_2/graphene nanocomposites. As shown in Figure 4.2, except TG-NH_3/8(ODCB, BA), the defect minimization was found in the chlorine-doped TiO_2/graphene nanocomposites compared to that of the undoped one. This fact was consistent with the photocatalytic performance of the chlorine-doped TiO_2/graphene nanocomposites.

4.4. Conclusion

The visible-light photocatalytic activity of the TiO_2/graphene nanocomposites was successfully improved by chlorine-doping. The chlorine-doped nanocomposites were prepared based on the chemical exfoliation of graphite with the aid of titanium tetra-*n*-butoxide followed by sol-gel reaction in the presence of chlorine organic compounds. Four

types of chlorine-doped nanocomposites were prepared with different chlorine sources and protocols, on which the enhancement in photocatalytic activity depended. From the difference in the performance and characteristics of the nanocomposites, it was found that the enhancement in the catalytic activity would be achieved by the mix contribution of extending in adsorption edge, formation of chlorine radicals, and reducing the number of defects in the graphene framework.

4.5. References

[1] Alfano, O. M., Bahnemann, D., Cassano, A. E., Dillert, R, Goslich, R. Photocatalysis in water environments using artificial and solar light. Catal. Today 2000; 58(2–3):199–230.

[2] Hoffmann, M. R., Martin, S. T., Choi, W., Bahnemann, D. W. Environmental applications of semiconductor photocatalysis. Chem. Rev. 1995; 95(1):69–96.

[3] Linsebigler, A. L., Lu, G., Yates, J. T. Photocatalysis on TiO_2 surfaces: Principles, mechanisms, and selected results. Chem. Rev. 1995; 95(3):735–58.

[4] Hamad, S., Catlow, C. R. A., Woodley, S. M., Lago, S. Structure and stability of small TiO_2 nanoparticles. J. Phys. Chem. B 2005; 109(33):15741–8.

[5] Varghese, O. K., Paulose, M., LaTempa, T. J., Grimes, C. A. High-rate solar photocatalytic conversion of CO_2 and water vapor to hydrocarbon fuels. Nano Lett. 2009; 9(2):731–7.

[6] Lee, S., Park, S. TiO_2 photocatalyst for water treatment applications. J. Ind. Eng. Chem. 2013; 19(6):1761–9.

[7] Anpo, M. Use of Visible Light. Second-generation titanium oxide photocatalysts prepared by the application of an advanced metal ion-implantation method. Pure Appl. Chem. 2000; 72(9):1787–92.

[8] Hu, C., Lan, Y., Qu, J., Hu, X., Wang, A. Ag/AgBr/TiO_2 visible light photocatalyst for destruction of Azodyes and bacteria. J. Phys. Chem. B 2006; 110(9):4066–72.

[9] Khairy, M., Zakaria, W. Effect of metal-doping of TiO_2 nanoparticles on their photocatalytic activities toward removal of organic dyes. Egypt. J. Pet. 2014; 23(4):419–26.

[10] Zhu, J., Zheng, W., He, B., Zhang, J., Anpo, M. Characterization of Fe-TiO_2 photocatalysts synthesized by hydrothermal method and their photocatalytic reactivity for photodegradation of XRG dye diluted in water. J. Mol. Catal. A: Chem. 2004; 216(1):35–43.

[11] Chen, D., Jiang, Z., Geng, J., Wang, Q., Yang, D. Carbon and nitrogen co-doped TiO_2 with enhanced visible-light photocatalytic activity. Ind. Eng. Chem. Res. 2007; 46(9):2741–6.

[12] Dong, F., Guo, S., Wang, H., Li, X., Wu, Z. Enhancement of the visible light photocatalytic activity of C-doped TiO_2 nanomaterials prepared by a green synthetic approach. J. Phys. Chem. C 2011; 115(27):13285–92.

[13] Huang, H., Li, D., Lin, Q., Zhang, W., Shao, Y., Chen, Y., *et al.* Efficient degradation of benzene over $LaVO_4/TiO_2$ nanocrystalline heterojunction photocatalyst under visible light irradiation. Environ. Sci. Technol. 2009; 43(11):4164–8.

[14] Gao, C., Li, J., Shan, Z., Huang, F., Shen, H. Preparation and visible-light photocatalytic activity of In_2S_3/TiO_2 composite. Mater. Chem. Phys. 2010; 122(1):183–7.

[15] Bessekhouad, Y., Robert, D., Weber, J. V. Bi_2S_3/TiO_2 and CdS/TiO_2 heterojunctions as an available configuration for photocatalytic degradation of organic pollutant. J. Photochem. Photobiol. A 2004; 163(3):569–80.

[16] Kim, S., Hwang, S. J., Choi, W. Visible light active Platinum-ion-doped TiO_2 photocatalyst. J. Phys. Chem. B 2005; 109(51):24260–7.

[17] Sobana, N., Muruganadham, M., Swaminathan, M. Nano-Ag particles doped TiO_2 for efficient photodegradation of direct Azo dyes. J. Mol. Catal. A: Chem 2006; 258(1–2):124–

32.

[18] Chen, B. Meng, Y., Sha, J., Zhong, C., Hu, W., Zhao, N. Preparation of MoS_2/TiO_2 based nanocomposites for photocatalysis and rechargeable batteries: Progress, challenges, and perspective. Nanoscale 2018; 10(1):34–68.

[19] Cozzoli, P. D., Kornowski, A., Weller, H. Low-temperature synthesis of soluble and processable organic-capped anatase TiO_2 nanorods. J. Am. Chem. Soc. 2003; 125(47):14539–48.

[20] Niederberger, M., Garnweitner, G., Krumeich, F., Nesper, R., Co, H. Tailoring the surface and solubility properties of nanocrystalline titania by a nonaqueous in situ functionalization process. Chem. Mater. 2004; 16(7):1202–8.

[21] Li, X., Wang, D., Cheng, G., Luo, Q. Preparation of polyaniline-modified TiO_2 nanoparticles and their photocatalytic activity under visible light illumination. Appl. Catal. B: Environ. 2008; 81(3–4):267–73.

[22] Ton, N. N. T., Dao, A. T. N., Kato, K., Ikenaga, T., Trinh, D. X., Taniike, T. One-pot synthesis of TiO_2/graphene nanocomposites for excellent visible light photocatalysis based on chemical exfoliation method. Carbon 2018; 133:109–17.

[23] Akhavan, O., Ghaderi, E. Photocatalytic reduction of graphene oxide nanosheets on TiO_2 thin film for photoinactivation of bacteria in solar light irradiation. J. Phys. Chem. C 2009; 113(47):20214–20.

[24] Li, N., Liu, G., Zhen, C., Li, F., Zhang, L., Cheng, H. M. Battery performance and photocatalytic activity of mesoporous anatase TiO_2 nanospheres/graphene composites by template-free self-assembly. Adv. Funct. Mater. 2011; 21(9):1717–22.

[25] Xiong, Z., Luo, Y., Zhao, Y., Zhang, J., Zheng, C., Wu, J. C. Synthesis, characterization and enhanced photocatalytic CO_2 reduction activity of graphene supported TiO_2 nanocrystals with coexposed {001} and {101} Facets. Phys. Chem. Chem. Phys.

2016; 18(19):13186–95.

[26] Ding, H., Zhang, S., Juan, P., Liu, T., Du, Z. Enhancing the photovoltaic performance of dye- sensitized solar cells by modifying TiO_2 photoanodes with exfoliated graphene sheets. RSC Adv. 2016; 6(47):41092–102.

[27] Jiang, G., Lin, Z., Chen, C., Zhu, L., Chang, Q., Wang, N., *et al.* TiO_2 nanoparticles assembled on graphene oxide nanosheets with high photocatalytic activity for removal of pollutants. Carbon 2011; 49(8):2693–701.

[28] Liu, X., Pan, L., Lv, T., Zhu, G., Lu, T., Sun, Z., *et al.* Microwave-assisted synthesis of TiO_2-reduced graphene oxide composites for the photocatalytic reduction of Cr(VI). RSC Adv. 2011; 1(7):1245–9.

[29] Xu, T., Zhang, L., Cheng, H., Zhu, Y. Significantly enhanced photocatalytic performance of ZnO via graphene hybridization and the mechanism study. Appl. Catal. B: Environ. 2011; 101(3–4):382–7.

[30] Larciprete, R., Fabris, S., Sun, T., Lacovig, P., Baraldi, A., Lizzit, S. Dual path mechanism in the thermal reduction of graphene oxide. J. Am. Chem. Soc. 2011; 133(43):17315–21.

[31] Sun, H., Wang, S., Ang, H. M., Tadé, M. O., Li, Q. Halogen element modified titanium dioxide for visible light photocatalysis. Chem. Eng. 2010; 162(2):437–47.

[32] Hattori, A., Shimoda, K., Tada, H., Ito, S. Photoreactivity of sol-gel TiO_2 films formed on soda-lime glass substrates: Effect of SiO_2 underlayer containing fluorine. Langmuir 1999; 15(16):5422–5.

[33] Minero, C., Mariella, G., Maurino, V., Pelizzetti, E. Photocatalytic transformation of organic compounds in the presence of inorganic anions. 1. Hydroxyl-mediated and direct electron-transfer reactions of phenol on a titanium dioxide-fluoride system. Langmuir 2000; 16(6):2632–41.

[34] Hattori, A., Tada, H. High photocatalytic activity of F-doped TiO_2 film on glass. J. Sol-gel Sci. Technol. 2001; 22(1–2):47–52.

[35] Vohra, M. S., Kim, S., Choi, W. Effects of surface fluorination of TiO_2 on the photocatalytic degradation of tetramethylammonium. J. Photochem. Photobiol. A: Chem. 2003; 160(1–2):55–60.

[36] Wang, X. K., Wang, C., Jiang, W. Q., Guo, W. L., Wang, J. G. Sonochemical synthesis and characterization of Cl-doped TiO_2 and its application in the photodegradation of phthalate ester under visible light irradiation. Chem. Eng. 2012; 189:288–94.

[37] Yuan, R., Chen, T., Fei, E., Lin, J., Ding, Z., Long, J., *et al.* Surface chlorination of TiO_2-based photocatalysts: A way to remarkably improve photocatalytic activity in both UV and visible region. ACS Catal. 2011; 1(3):200–6.

[38] Xu, H., Zheng, Z., Zhang, L., Zhang, H., Deng, F. Hierarchical chlorine-doped rutile TiO_2 spherical clusters of nanorods: Large-scale synthesis and high photocatalytic activity. J. Solid State Chem. 2008; 181(9):2516–22.

[39] Long, M., Cai, W., Chen, H., Xu, J. Preparation, characterization and photocatalytic activity of visible light driven chlorine-doped TiO_2. Front. Chem. China 2007; 2(3):278–82.

[40] Lin, H., Deng, W., Zhou, T., Ning, S., Long, J., Wang, X. Iodine-modified nanocrystalline titania for photo-catalytic antibacterial application under visible light illumination. Appl. Catal. B: Environ. 2015; 176:36–43.

[41] Zhang, L., Zhou, J., Li, J., Liu, G., Lin, X., Mao, B., *et al.* Surface structural reconstruction for optical response in iodine-modified TiO_2 photocatalyst system. J. Phys. Chem. C 2014; 118(25):13726–32.

[42] Zhang, Q., Li, Y., Ackerman, E. A., Gajdardziska-Josifovska, M., Li, H. Visible light responsive iodine-doped TiO_2 for photocatalytic reduction of CO_2 to fuels. Appl. Catal. A: Gen. 2011; 400(1–2):195–202.

[43] Hummers Jr, W. S., Offeman, R. E. Preparation of graphitic oxide. J. Am. Chem. Soc., 1958; 80(6):1339.

[44] Jiang, B., Tian, C., Pan, Q., Jiang, Z., Wang, J. Q., Yan, W., *et al*. Enhanced photocatalytic activity and electron transfer mechanisms of graphene/TiO_2 with exposed {001} facets. J. Phys. Chem. C 2011; 115(48):23718–25

[45] Xiang, Q., Yu, J., Jaroniec, M. Enhanced photocatalytic H_2-production activity of graphene-modified titania nanosheets. Nanoscale 2011; 3(9):3670–8.

[46] Yang, D., Velamakanni, A., Bozoklu, G., Park, S., Stoller, M., Piner, R. D, *et al.* Chemical analysis of graphene oxide films after heat and chemical treatments by X-ray photoelectron and Micro-Raman spectroscopy. Carbon 2009; 47(1):145–52.

[47] Ohsaka, T., Izumi, F., Fujiki Y. Raman spectrum of anatase. J. Raman Spectrosc. 1978; 7(6):321−4.

[48] Pimenta, M. A., Dresselhaus, G., Dresselhaus, M. S., Cancado, L. G., Jorio, A., Saito, R. Studying disorder in graphite-based systems by Raman spectroscopy. Phys. Chem. Chem. Phys. 2007; 9(11):1276–90.

[49] Zhang, W., Cui, J., Tao, C. A., Wu, Y., Li, Z., Ma, L., *et al*. A strategy for producing pure single-layer graphene sheets based on a confined self-assembly approach. Angew. Chem. Int. Ed. 2009; 121(32):5978−82.

[50] Kovtyukhova, N. I., Wang, Y., Berkdemir, A., Cruz-Silva, R., Terrones, M., Crespi, V. H., *et al*. Non-oxidative intercalation and exfoliation of graphite by Brønsted acids. Nat. Chem. 2014; 6(11):957.

[51] Lyklema, J. The surface tension of pure liquids: Thermodynamic components and corresponding states. Colloids Surf. A 1999; 156(1–3):413–21.

[52] Israelachvili, J. N. Intermolecular and surface forces, third ed. Academic press. 2011.

[53] Coleman, J. N. Liquid exfoliation of defect-free graphene. Acc. Chem. Res. 2013; 46(1):14–22.

[54] Hernandez, Y., Nicolosi, V., Lotya, M., Blighe, F. M., Sun, Z., De, S., *et al.* High-yield production of graphene by liquid-phase exfoliation of graphite. Nat. Nanotechnol. 2008; 3(9):563–8.

[55] National Center for Biotechnology Information, National Library of Medicine. https://pubchem.ncbi.nlm.nih.gov/ (accessed 25 March 2020).

[56] Look for Chemicals. https://www.lookchem.com/ (accessed 25 March 2020).

[57] Beams, R., Cançado, L. G., Novotny, L. Raman characterization of defects and dopants in graphene. J. Phys.: Condens. Matter. 2015; 27(8):083002.

[58] Reddy, K. M., Reddy, C. G., Manorama, S. V. Preparation, characterization, and spectral studies on nanocrystalline anatase TiO_2. J. Solid State Chem. 2001; 158(2):180–6.

[59] Lewandowski, M., Ollis, D. F. Halide acid pretreatments of photocatalysts for oxidation of aromatic air contaminants: rate enhancement, rate inhibition, and a thermodynamic rationale. J. Catal. 2003; 217(1):38–46.

[60] Bhatkhande, D. S., Pangarkar, V. G., Beenackers, A. A. C. M. Photocatalytic degradation for environmental applications-a review. J. Chem. Technol. Biotechnol. 2002; 77(1):102–16.

[61] Fu, X., Zeltner, W. A., Anderson, M. A. The gas-phase photocatalytic mineralization of benzene on porous titania-based catalysts. Appl. Catal. B: Environ. 1995; 6(3):209–24.

[62] Liang, Y. T., Vijayan, B. K., Gray, K. A., Hersam, M. C. Minimizing graphene defects enhances titania nanocomposite-based photocatalytic reduction of CO_2 for improved solar fuel production. Nano Lett. 2011; 11(7):2865–70.

CHAPTER 5. General Conclusion and Future Plan

5.1. General conclusion

According to the high ability to adsorb organic pollutants, the improvement of the photo-induced charge career separation, as well as the absorption of visible light, TiO_2/graphene has been widely studied for the utilization in various applications, especially in the detoxification and disinfection of wastewater. However, the photocatalytic performance of the TiO_2/graphene was insufficient for practical applications. Conventionally, the TiO_2/graphene was synthesized from graphene oxide (GO) coupled with TiO_2 or a titanium alkoxide, which was subsequently reduced to rGO. However, this reduction process always led to the formation of defect-rich rGO. Furthermore, the aggregation of TiO_2 was usually observed which was caused by the hydrophilic nature of GO. In this thesis, a novel method for the fabrication of TiO_2/graphene nanocomposites has been established, which alleviated the problems in the conventional TiO_2/rGO photocatalysts.

A novel GO-free route to synthesize TiO_2/graphene nanocomposites has been examined in Chapter 2. The synthetic approach involved the chemical exfoliation of graphite in a titanium tetra-*n*-butoxide and subsequent sol-gel reaction catalyzed with benzylamine. This afforded the TiO_2/graphene nanocomposites featured with i) a morphology in which TiO_2 nanolayers uniformly and thinly covered graphene sheets, ii) a trace amount of defects on the graphene frameworks, iii) a dramatic inhibition of charge carriers recombination, and iv) a significant extension of absorption edge into visible-light area. Owing to these advantages, the TiO_2/graphene nanocomposites exhibited an

outstanding photocatalytic performance in the degradation of methylene blue in water. The obtained TiO_2/graphene nanocomposites presented 5 and 15 times greater in photocatalytic activity compared to that of the conventional TiO_2/rGO nanocomposite and the commercial TiO_2-P25.

Motivated by the finding that a titanium alkoxide can exfoliate graphite into high-quality graphene, I focused on the exploration of solvents for the liquid-phase exfoliation of graphite under ultrasonication in Chapter 3. Through the screening of different solvents and their mixtures, a number of new exfoliating solvents have been identified. Particularly, chlorobenzylamine, which is a combination of the molecular structure of chlorobenzene and benzylamine, known as famous exfoliating solvents, presented the highest graphene yield. In addition, titanium alkoxides showed a high yield although its surface tension was far from that of graphene. More importantly, a synergistic effect among different functional groups e.g. aromatic, amine, and halogen groups was identified, and this was more effectively exploited in a form of solvent mixtures.

In Chapter 4, further enhancement in the photocatalytic activity of the TiO_2/graphene nanocomposites was achieved by pursuing the fabrication of chlorine-doped TiO_2/graphene nanocomposites. The chlorine-doped TiO_2/graphene nanocomposites were fabricated based on the synthetic method established in Chapter 2. With the aid of chlorine radicals in accelerating the photodecomposition of organic compounds, the nanocomposites exhibited a significant enhancement in the visible-light photocatalytic activity compared to that of the undoped TiO_2/graphene nanocomposites in the photodecomposition of methylene blue, phenol, and naphthalene.

This thesis has established a novel and effective route for the synthesis of the TiO_2/graphene nanocomposites and demonstrated its usefulness in the field of water treatment based on excellent visible-light photocatalysis. It was also suggested that a similar

method is applicable for the synthesis of different oxide@graphene nanocomposites with advantageous features.

5.2. Future plan

Nowadays, organic pollution of rivers and lakes by sewage released from human activities like farming, industry, or even daily life increasingly affects ecosystems and human worldwide. The containing of pathogens in untreated urban wastewater can cause a variety of serious diseases, which can kill human life. Organic pollutants accumulating in rivers and lakes accelerate the growth of microbial, resulting in oxygen exhaustion and consequently destroy the river and lake ecosystems. With the concern to reduce the amount of organic pollutants in water, the target of future research is to develop a unique and simple photocatalytic water treatment system, which can operate in polluted rivers and lakes using solar light. The TiO_2/graphene nanocomposites developed in this thesis are expected to fit to this purpose. There are several requirements, which need further consideration. For example, one of the most important requirements is the long-term stability of the immobilized catalyst in different water flow rates. Thus, it is necessary to develop an effective immobilization method to significantly improve the adhesion stability of the immobilized photocatalysts. Further enhancement of the photocatalytic performance of TiO_2/graphene nanocomposites is also required since the amount as well as the diversity of the pollutants in the applied environment is significantly different compared to the laboratory conditions. The improvement of light utilization efficiency of the catalyst under the water is the next concern. In order to achieve an expected performance efficiency of the photocatalytic water treatment, an effective solar light accumulation should be considered for this system. The

successful establishment of the photocatalytic water treatment system can contribute partly to the global efforts in combating global warming.

Achievements

A) Publications

1. Solvent Screening for Efficient Chemical Exfoliation of Graphite. **Nhan Nu Thanh Ton**, Minh-Quyet Ha, Takuma Ikenaga, Ashutosh Thakur, Hieu-Chi Dam, Toshiaki Taniike. (Submitted).

2. One-pot synthesis of TiO_2/graphene nanocomposites for excellent visible-light photocatalysis based on chemical exfoliation method. **Nhan Nu Thanh Ton**, Anh Thi Ngoc Dao, Koichiro Kato, Takuma Ikenaga, Dai Xuan Trinh, Toshiaki Taniike. Carbon, 2018, 133, 109–117.

B) Conferences

International conferences:

1. One-pot Synthesis of TiO_2/graphene Nanocomposite for Visible-light Photocatalysis. **Nhan Nu Thanh Ton**, Anh Thi Ngoc Dao, Ashutosh Thakur, Kouichiro Kato, Toshiaki Taniike, The 8th Asia Pacific Congress on Catalysis (APCAT-8), Bangkok, Thailand, Aug. 4-7, 2019, oral.

2. Synthesis of TiO_2/Graphene Nanocomposites with Excellent Visible-light Photocatalytic Activity Based on Chemical Exfoliation Method. **Nhan Nu Thanh Ton**, Anh Thi Ngoc Dao, Kouichirou Katou, Toshiaki Taniike, 20th International Conference on Heterogeneous Catalysis, Osaka, Japan, Oct. 11-12, 2018, oral.

C) Award

1. Best Presentation Award, "Synthesis of TiO_2/graphene Nanocomposites with Excellent Visible-Light Photocatalytic Activity Based on Chemical Exfoliation Method", **Nhan Nu Thanh Ton**, 20^{th} International Conference on Heterogeneous Catalysis 2018, Osaka, Japan, 10/2018.